OCS Study
MMS 98-0052

Coastal Marine Institute

Coastal Marine Environmental Modeling

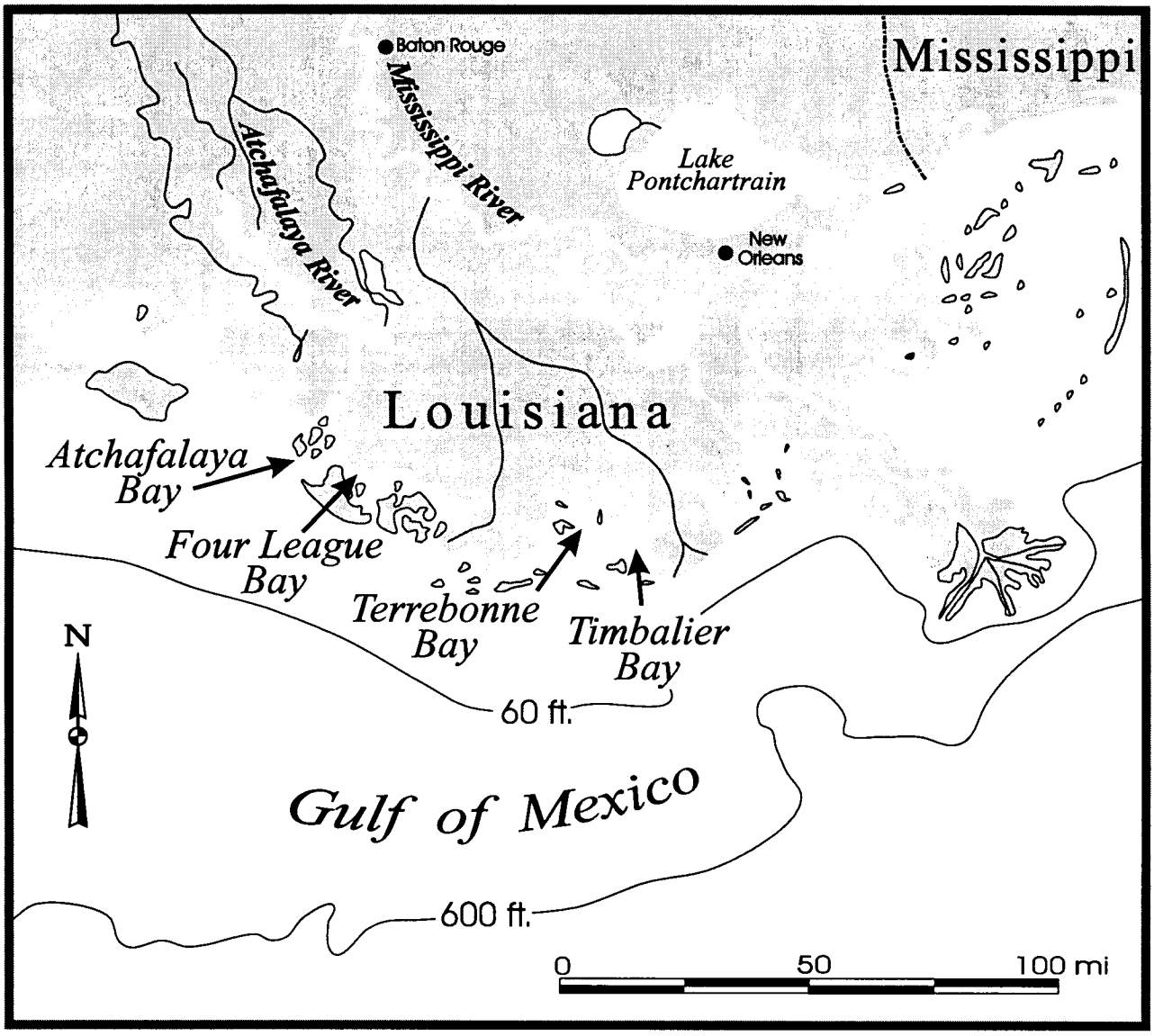

MMS U.S. Department of the Interior
Minerals Management Service
Gulf of Mexico OCS Region

Cooperative Agreement
Coastal Marine Institute
Louisiana State University

OCS Study
MMS 98-0052

Coastal Marine Institute

Coastal Marine Environmental Modeling

Authors

Masamichi Inoue
William J. Wiseman, Jr.
Dongho Park

December 1998

Prepared under MMS Contract
14-35-0001-30660-19917
by
Coastal Marine Institute
Louisiana State University
Baton Rouge, Louisiana 70803

Published by

U.S. Department of the Interior
Minerals Management Service
Gulf of Mexico OCS Region

Cooperative Agreement
Coastal Marine Institute
Louisiana State University

DISCLAIMER

This report was prepared under contract between the Minerals Management Service (MMS) and Louisiana State University. This report has been technically reviewed by the MMS and approved for publication. Approval does not signify that the contents necessarily reflect the view and policies of the Service nor does mention of trade names or commercial products constitute endorsement or recommendation for use. It is, however, exempt from review and compliance with MMS editorial standards.

REPORT AVAILABILITY

Extra copies of the report may be obtained from the Public Information Office (MS 5034) at the following address:

U.S. Department of the Interior
Minerals Management Service
Public Information Office (MS 5034)
Gulf of Mexico OCS Region
1201 Elmwood Park Boulevard
New Orleans, Louisiana 70123-2394

Telephone Number: (504) 736-2519
1-800-200-GULF

CITATION

Suggested citation:

Inoue, M., W. J. Wiseman, Jr. and D. Park. 1998. Coastal Marine Environmental Modeling. OCS Study MMS 98-0052. U.S. Dept. of the Interior, Minerals Management Service, Gulf of Mexico OCS Region, New Orleans, La. 133 pp.

ABSTRACT

A two-dimensional, depth-integrated, barotropic, numerical hydrodynamic model is developed to study the circulation and mixing processes in the shallow bays characteristic of coastal Louisiana. It is applied with varying degrees of success to three different estuarine systems. The model is coupled to an ecological code to investigate the processes responsible for plankton biomass variability within one of these systems.

In the sediment starved, low-runoff environment of lower Terrebonne/Timbalier Basin, comparison of historical current meter records and model output, forced by observed winds and tides, yielded correlation coefficients of about 0.9. A large bottom friction (Manning's coefficient ~ 0.07) is required by the model, apparently reflecting wave-current interactions - a process not resolved explicitly by the model. Despite the microtidal environment of the northern Gulf of Mexico, tidal currents were an important component of the current spectrum within the bay system, even during equatorial tides. Local wind forcing was also important in controlling the general flow direction in the broad open reaches of the bay system, particularly during equatorial tidal conditions. Flushing time, estimated by a particle tracking technique, was 27 days, in good agreement with previous estimates derived from tidal prism modeling. Horizontal diffusivities estimated using the tracer particles ranged from 3.8 to 19.5 $m^2 s^{-1}$, values comparable to those compiled by Okubo (1974) at similar length scales. The larger values appear to be due to coastal topographic trapping. Mixing of water masses, based on particle tracking, is found to consist of continuous stretching, folding and break-up of material lines due to the interaction of wind-driven and tidal currents with bottom and coastal topography. In particular, coastal topographic trapping appears to be an important process by which stirring and mixing processes are enhanced, thus making them more efficient and chaotic . These observations point to the need to resolve small-scale shear flow patterns, in both space and time, and detailed bottom and coastal topography in order to understand transport, stirring and mixing processes in such broad shallow estuaries.

In an application to the Barataria Basin, the model domain was extended beyond the open bay into the interconnected tidal channels, lakes, and creeks of the upper basin. Barataria Basin receives greater freshwater runoff than the Terrebonne/Timbalier system, but is still isolated from any large drainage basin. Model calibration to observed water levels was good, but the comparison of model and observed currents was less satisfying than in the Terrebonne/Timbalier application. This appears to be due to the narrow channels in the upper basin which are inadequately resolved by the 0.5 km model grid size and by inadequately resolved depths within the upper basin. Spin-up time for this more complex model domain was significantly longer than for the earlier application, but the required friction appeared to be somewhat less (Manning's coefficient ~0.04). The modeled current field in the open water reaches of the lower basin responded to wind and tidal forcing in a manner similar to that observed in the Terrebonne/Timbalier Bay model. Particle tracer experiments, again, indicated the importance of topographic trapping in defining the dispersion characteristics of the system, particularly in the lower reaches of the system. Flushing times increased dramatically as one moved into the

slowly-moving, crenulated and highly interconnected waters of the upper basin. This is consistent with previous tidal prism model results. Estimated dispersion coefficients are, again, consistent with Okubo's estimates (Okubo, 1974).

The hydrodynamic code has been successfully calibrated to Fourleague Bay, a small estuary immediately east of the Atchafalaya River mouth and which is forced directly by Atchafalaya River discharge under high flow or westerly wind conditions. While the neglect of baroclinic pressure gradients is least justified in this case, the excellent calibration results appear to justify a barotropic model, at least to first order. In order to begin to investigate estuarine ecosystem dynamics, the calibrated model was coupled to a simple ecological model. Climatological nitrogen and suspended sediment concentrations characteristic of the seasonal variability associated with the Atchafalaya River were imposed at the upstream open boundary. Sediment was allowed to settle from suspension, but not to resuspend. Light was attenuated by the suspended sediment and phytoplankton grew in response to the available light and nitrogen. A constant rate of zooplankton grazing was assumed. Phytoplankton blooms in the lower bay occur on time scales of one to two weeks. This is a response to improved light conditions in the lower bay. Tidal pumping effectively flushes the phytoplankton from the system, potentially allowing Fourleague Bay to act as a source of phytoplankton for the nearshore Gulf waters.

TABLE OF CONTENTS

PAGE

LIST OF FIGURES ix

LIST OF TABLES xix

ACKNOWLEDGEMENTS xxi

CHAPTER

1 INTRODUCTION 1

2 TERREBONNE/TIMBALIER BASIN STUDY 5
- 2.1 Background 5
- 2.2 Numerical Model Formulation 9
- 2.3 Computation of Particle Trajectories 11
- 2.4 Model Calibration 14
- 2.5 Model Simulation 17
- 2.6 Flushing Characteristics 17
- 2.7 Particle Dispersion 26
- 2.8 Mixing and Stirring of "Bay Water" with "Open Gulf Water" 36
- 2.9 Summary and Conclusions 44

3 BARATARIA BASIN STUDY 51
- 3.1 Background 51
- 3.2 Model Calibration 54
- 3.3 Model Simulation 57
- 3.4 Flushing Characteristics 68
- 3.5 Particle Dispersion 87
- 3.6 Summary and Conclusions 87

4 COUPLED HYDRODYNAMIC-ECOLOGICAL MODEL 101
- 4.1 Background 101
- 4.2 Model Formulation 104
- 4.3 Model Equations 106
- 4.4 Model Simulation 107
- 4.5 Summary and Conclusions 123

5 CONCLUSIONS 125

REFERENCES 127

LIST OF FIGURES

FIGURE		PAGE
1	(a) Location map of study area. (b) Chart of Terrebonne/ Timbalier Bay. Numbered dots indicate mooring locations. Dashed line is a dredged ship channel.	6
2	Clockwise (CW) and counter-clockwise (CCW) variance-preserving velocity spectra from a 203-day record at site 3. Spectra were estimated by smoothing the periodogram with an 11-point triangular running filter. Spectra units are ($cm^2 s^{-2}$).	7
3	Variance-preserving salinity spectrum for a 77-day record from site 3 (After McKee et al., 1992). Spectrum was estimated by smoothing the periodogram with an 11-point triangular running filter.	8
4	(a) Salinity time series from site 3. (b) Time series of Mississippi River discharge at Tarbert Landing, LA. The time origin (day 0) for these plots is 1 January 1990	10
5a	Model geometry of the Terrebonne/Timbalier Bay Model. The southern boundary is open.	12
5b	Model bathymetry of the Terrebonne/Timbalier Bay Model. Bottom bathymetric countours are shown at every 0.5 m.	13
6	Observed (solid line) and simulated (dashed line) currents at Station 3 located in the middle of Terrebonne Bay for the period 03/21/90-03/27/90. East-west component (top), and north-south component (bottom). r is the correlation coefficient between the observed and simulated currents	16
7	Observed sea-level height at site 1 during May, 1990	18
8	Observed wind at Isles Dernier during May, 1990. (a) Wind speed ($m s^{-1}$). (b) Wind direction (degrees measured clockwise from North)	19
9a	Simulated currents in Terrebonne/Timbalier Bay. Maximum velocity vector (in units of cm s^{-1}) is shown at the bottom right. Vectors are plotted at every other grid points. Ebb tidal current at equatorial tide at 446 hr from 05/01/90. Maximum current speed of 69 cm s^{-1} in Little Pass Timbalier is not shown.	20

FIGURE PAGE

9b Flood tidal current at equatorial tide at 457 hr from 05/01/90. Maximum current speed of 59 cm s^{-1} in Whisky Pass is not shown. 21

9c Flood tidal current at tropic tide at 504 hr from 05/01/90. Maximum current speed of 110 cm s^{-1} in Whisky Pass is not shown 22

9d Ebb tidal current at tropic tide at 518 hr from 05/01/90. Maximum current speed of 192 cm s^{-1} in Whisky Pass is not shown 23

10 Maximum current speed (in cm s^{-1}) simulated for the period 05/01/90-05/25/90. Very large currents are always located either in Little Pass Timbalier or in Whisky Pass. 24

11 Mean simulated current speed (in cm s^{-1}) for the period 05/07/90-05/25/90. Hatched areas have current speed less than 10 cm s^{-1} 25

12 Distribution of tracer particles simulated for the period 05/02/90-05/25/90. a) At time of release (0 hr 05/02/90) b) After 24 hours 27

12 Distribution of tracer particles simulated for the period 05/02/90-05/25/90. c) After 240 hours. d) After 480 hours 28

12 Distribution of tracer particles simulated for the period 05/02/90-05/25/90. e) After 600 hours 29

13 A subset of tracer particles used in Figure 12. a) At time of release (0 hr 05/02/90). b) After 24 hours. 30

13 A subset of tracer particles used in Figure 12. c) After 48 hours. d) After 168 hours. 31

13 A subset of tracer particles used in Figure 12. e) After 216 hours 32

14 Variance (open circle), $\sigma_X\sigma_Y$, versus time for the particle cluster shown in Figure 13. Solid line is a least square fit 34

FIGURE PAGE

15 Horizontal diffusivities ($cm^2\ s^{-1}$) of 100 particles released at various locations (b: Lake Barre; e: Terrebonne; f: Lake Felicity; p: Lake Pelto; r: Lake Raccourci; t: Timbalier) versus scale of diffusion, $l = 3\sqrt{2\sigma_X\sigma_Y}$ (Okubo, 1971). Range of Okubo's data (1974) is bounded by the two solid lines, $K_{XY} = 0.01(\frac{l^2}{9})^{2/3}$ and $K_{XY} = 0.002(\frac{l^2}{9})^{2/3}$ (Fischer et al., 1979) 35

16 Distribution of tracer particles simulated for the period 05/02/90-05/25/90. A total of 9800 particles were released along a straight line across Wine Island and Cat Island Passes. a) At time of release. b) After 24 hours 38

16 Distribution of tracer particles simulated for the period 05/02/90-05/25/90. A total of 9800 particles were released along a straight line across Wine Island and Cat Island Passes. c) After 48 hours. d) 72 hours. 39

16 Distribution of tracer particles simulated for the period 05/02/90-05/25/90. A total of 9800 particles were released along a straight line across Wine Island and Cat Island Passes. e) After 96 hours. f) After 120 hours. 40

16 Distribution of tracer particles simulated for the period 05/02/90-05/25/90. A total of 9800 particles were released along a straight line across Wine Island and Cat Island Passes. g) After 144 hours 41

17a Mean separation distance between neighboring particles along the line formed by 9800 particles as a function of time 42

17b Fraction of the particles remaining within the model domain as a function of time 43

18a Mean separation distance between neighboring particles along the line formed by 9800 particles as a function of time for the first 100 hours. Points indicate the case shown in Figure 17. +, open circle, and * indicate three cases with the initial release time lagged by 6, 12, and 18 hours, respectively relative to the first case shown in Figure 17. 45

FIGURE PAGE

18b Same as (a) except shown for the entire period of the experiments. 46

18c Fraction of the particles remaining within the model domain as a function of time. Symbols are same as for (a) and (b). 47

19 Location map of Barataria Basin and model geometry. The southern boundary is open. 52

20 Locations of stations where data on sea level height (denoted by S), currents (denoted by C) and winds are available for model calibration. Bottom bathymetric contours are shown at every 2.5 m. 53

21 Simulated and observed sea level height at Sts. 01 and 12. Spin-up period is indicated during which the model initialization from rest appears to have died down. Analysis of model output is performed excluding the spin-up period 55

22 Comparison of the observed (solid line) and the simulated (dotted line) sea level height. (a) At St. 01. (b) At St. 02 58

22 Comparison of the observed (solid line) and the simulated (dotted line) sea level height. (c) At St. 03. (d) At St. 11 59

22 Comparison of the observed (solid line) and the simulated (dotted line) sea level height. (e) At St. 12. (f) At St. 16 60

22 Comparison of the observed (solid line) and the simulated (dotted line) sea level height. (g) At St. 18. (h) At St. 20 61

23a Comparison of the observed (solid line) and the simulated (dotted line) current components. East-west component (top figure) and north-south component (bottom figure) at St. 04 62

23b Comparison of the observed (solid line) and the simulated (dotted line) current components. East-west component (top figure) and north-south component (bottom figure) at St. 07. 63

FIGURE PAGE

23c Comparison of the observed (solid line) and the simulated (dotted line) current components. East-west component (top figure) and north-south component (bottom figure) at St. 08. 64

24 Wind vectors observed at Grand Isle for the period 07/17/88-07/27/88. 65

25 Sea level height simulated at St. 16 (at the mouth of Barataria Bay) and eight instantaneous moments (74th, 80th, 86th and 92nd hour represent low, maximum flood, high and maximum ebb tides, respectively, during a tidal cycle of equatorial tide; 222nd, 228th, 234th and 240th hour represent low, maximum flood, high and maximum ebb tides, respectively, during a tidal cycle of tropic tides). 66

26 Tidal propagation simulated in the model. Time lags relative to station 16 are shown. 67

27a Simulated currents in Barataria Basin at Hour 74. Different scalings for velocity vector are used for the upper and lower domains. Reference velocity vectors are indicated. 69

27b Simulated currents in Barataria Basin at Hour 80. Different scalings for velocity vector are used for the upper and lower domains. Reference velocity vectors are indicated. 70

27c Simulated currents in Barataria Basin at Hour 86. Different scalings for velocity vector are used for the upper and lower domains. Reference velocity vectors are indicated. 71

27d Simulated currents in Barataria Basin at Hour 92. Different scalings for velocity vector are used for the upper and lower domains. Reference velocity vectors are indicated. 72

27e Simulated currents in Barataria Basin at Hour 222. Different scalings for velocity vector are used for the upper and lower domains. Reference velocity vectors are indicated. 73

FIGURE PAGE

27f Simulated currents in Barataria Basin at Hour 228. Different scalings for velocity vector are used for the upper and lower domains. Reference velocity vectors are indicated. 74

27g Simulated currents in Barataria Basin at Hour 234. Different scalings for velocity vector are used for the upper and lower domains. Reference velocity vectors are indicated. 75

27h Simulated currents in Barataria Basin at Hour 240. Different scalings for velocity vector are used for the upper and lower domains. Reference velocity vectors are indicated. 76

28a Distribution of tracer particles simulated for the period 07/17/88-07/27/88 in Barataria Basin. At time of release (0 hr 07/17/88) 77

28b Distribution of tracer particles simulated for the period 07/17/88-07/27/88 in Barataria Basin. After 48 hours 78

28c Distribution of tracer particles simulated for the period 07/17/88-07/27/88 in Barataria Basin. After 96 hours 79

28d Distribution of tracer particles simulated for the period 07/17/88-07/27/88 in Barataria Basin. After 144 hours 80

28e Distribution of tracer particles simulated for the period 07/17/88-07/27/88 in Barataria Basin. After 192 hours 81

28f Distribution of tracer particles simulated for the period 07/17/88-07/27/88 in Barataria Basin. After 240 hours 82

29 Eight sub-basins in Barataria Basin used for estimating flushing time 83

30a Distribution of tracer particles in Sub-basins A, B and C in Barataria Basin for the period 07/17/88-07/27/88. At time of release (0 hr 07/17/88) (Left figure). After 240 hours (Right figure). 84

FIGURE PAGE

30b Distribution of tracer particles in Sub-basins D, E and F in Barataria Basin for the period 07/17/88-07/27/88. At time of release (0 hr 07/17/88) (Left figure). After 240 hours (Right figure). 85

30c Distribution of tracer particles in Sub-basins G and H in Barataria Basin for the period 07/17/88-07/27/88. At time of release (0 hr 07/17/88) (Left figure). After 240 hours (Right figure). 86

31 A cluster of 49 tracer particles released at Lake Salvador. (a) At time of release (0 hr 07/17/88). (b) After 24 hours. (c) After 48 hours. (d) After 72 hours. (e) After 96 hours. (f) After 120 hours 89

31 A cluster of 49 tracer particles released at Lake Salvador. (g) After 144 hours. (h) After 168 hours. (i) After 192 hours. (j) After 216 hours. (k) After 240 hours 90

32 A cluster of 49 tracer particles released at Little Lake. (a) At time of release (0 hr 07/17/88). (b) After 24 hours. (c) After 48 hours. (d) After 72 hours. (e) After 96 hours. (f) After 120 hours 91

32 A cluster of 49 tracer particles released at Little Lake. (g) After 144 hours. (h) After 168 hours. (i) After 192 hours. (j) After 216 hours. (k) After 240 hours 92

33 A cluster of 49 tracer particles released at Barataria Bay. (a) At time of release (0 hr 07/17/88). (b) After 24 hours. (c) After 48 hours. (d) After 72 hours. (e) After 96 hours. (f) After 120 hours 93

33 A cluster of 49 tracer particles released at Barataria Bay. (g) After 144 hours. (h) After 168 hours. (i) After 192 hours. (j) After 216 hours. (k) After 240 hours 94

34 A cluster of 49 tracer particles released at Caminada Bay. (a) At time of release (0 hr 07/17/88). (b) After 24 hours. (c) After 48 hours. (d) After 72 hours. (e) After 96 hours. (f) After 120 hours 95

FIGURE PAGE

34 A cluster of 49 tracer particles released at Caminada Bay. (g) After 144 hours. (h) After 168 hours. (i) After 192 hours. (j) After 216 hours. (k) After 240 hours 96

35 Variance, $\sigma_X\sigma_Y$, versus time for the particle clusters released in four areas shown in Figures 31 through 34 97

36 Horizontal diffusitivities (cm^2/sec) of clusters of 49 particles released at various locations (Lake Salvador, Little Lake, Barataria Bay and Caminada Bay) versus scale of diffusion, $l = 3\sqrt{2\sigma_X\sigma_Y}$ (Okubo, 1971). Range of Okubo's data (1974) is bounded by the two solid lines, $K_{XY} = 0.01(\frac{l^2}{9})^{2/3}$ and $K_{XY} = 0.002(\frac{l^2}{9})^{2/3}$ (Fischer et al., 1979) 98

37 Model geometry of the Fourleague Bay Model. The southern and the western boundaries are open 102

38 Model bathymetry of the Fourleague Bay Model. Bottom bathymetric contours are shown at every 0.5 m. 103

39a Simulated concentrations of suspended sediment ($mg\ l^{-1}$) (solid line), nitrogen (μg at l^{-1}) (+) and phytoplankton ($\mu g\ l^{-1}$) (circles) for the first 30 days. At Upper Fourleague Bay 110

39b Simulated concentrations of suspended sediment ($mg\ l^{-1}$) (solid line), nitrogen (μg at l^{-1}) (+) and phytoplankton ($\mu g\ l^{-1}$) (circles) for the first 30 days. At Mid Fourleague Bay 111

39c Simulated concentrations of suspended sediment ($mg\ l^{-1}$) (solid line), nitrogen (μg at l^{-1}) (+) and phytoplankton ($\mu g\ l^{-1}$) (circles) for the first 30 days. At Lower Fourleague Bay 112

40a Simulated concentrations of suspended sediments ($mg\ l^{-1}$) in Fourleague Bay on Day 18. 113

40b Simulated concentrations of nitrogen (μg at l^{-1}) in Fourleague Bay on Day 18 114

40c Simulated concentrations of phytoplankton ($\mu g\ l^{-1}$) in Fourleague Bay on Day 18 115

FIGURE PAGE

41 Simulated currents in Oyster Bayou. Positive northward, negative southward currents. Notice the mean currents are southward, indicating a net flow through Fourleague Bay due to influx of discharge from Atchafalaya River. 116

42a Simulated suspended sediment (mg l^{-1}) in Oyster Bayou 117

42b Simulated nitrogen (μg at l^{-1}) in Oyster Bayou 118

42c Simulated phytoplankton (μg l^{-1}) in Oyster Bayou 119

43a Simulated suspended sediment flux (mg $cm^{-2}s^{-1}$) through Oyster Bayou. Negative values indicate southward flux toward the open Gulf 120

43b Simulated nitrogen flux (μg at $cm^{-2}s^{-1}$) through Oyster Bayou. Negative values indicate southward flux toward the open Gulf 121

43c Simulated phytoplankton flux (μg $cm^{-2}s^{-1}$) through Oyster Bayou. Negative values indicate southward flux toward the open Gulf 122

LIST OF TABLES

TABLE PAGE

1 Observed and simulated phase lag (minutes) in sea level height relative to St. 16 for three different Manning's coefficients. 56

2 Ratio of amplitude between simulated and observed sea level heights for three different Manning's coefficients. 56

3 Estimated flushing time in eight sub-basins 88

ACKNOWLEDGMENTS

We would like to thank the Coastal Marine Institute at LSU that is funded by the Minerals Management Service for providing the necessary support of this project. We would also like to thank the System Network Computing Center for the free usage of the IBM 9672-R53 mainframe.

We would like to acknowledge the essential role of Dr. Dubravko Justic in originally formulating all the model equations used in the ecological modeling and in coupling the hydrodynamic model to the ecological model. Dr. S. A. Hsu provided the wind data as well as the wind stress formulation suitable for the region under study. In this study we made an extensive use of a computer animation software produced by Mr. Lingsong Bi. Additional assistance in computer graphics was provided by Dr. S. E. Welsh. Our acknowledgments are extended to Mr. David Wilensky and Mr. Aleric Haaq for maintaining the computing facilities at CSI.

CHAPTER 1

INTRODUCTION

Estuaries are important coastal features, world-wide. They represent sheltered harbors for maritime transportation. They are the coastal terminus of inland waterways connecting sea routes with the continental interior. They are sites of major fisheries, both recreational and commercial. They are sites of significant industrial development and major population centers. They are important recreational sites.

The potential uses of these coastal systems represent multiple and, potentially, conflicting demands. As a common, but finite, resource, estuaries must be carefully managed. This management task falls under many different jurisdictional authorities - local, state, and federal. While certain processes are common to estuaries, in general, each system presents unique problems and opportunities which must be assessed and considered during the design of an enlightened management program focused on the sustainable development of a region. Cost-effectiveness criteria preclude the exhaustive monitoring which would be most desirable in each basin. One possible alternative to extensive monitoring is modeling of these systems. While such modeling requires some monitoring to calibrate the models, define the forcing functions and boundary conditions required to drive them and skill assess the models' usefulness, the necessary savings, in both time and dollars, over the cost of a complete monitoring program should be significant.

Louisiana's coast is replete with estuarine systems of different characteristics. Within the continental United States, Louisiana accounts for 25% of the identifiable vegetated wetlands and 40% of the tidally-influenced wetlands. The most common of these is the bar-built estuary. These estuaries often result from the abandonment of a delta of the Mississippi River system with consequent subsidence and reworking of the deltaic sediments. As these unconsolidated sediments are reworked by waves and tides, marsh is lost and open water, estuarine reaches develop. Sand bodies from river mouth bars are reworked to form barrier islands at the mouths of the estuaries (Penland 1990). The tidal passes through these barriers restrict the exchange of waters between the coastal ocean and the estuary, while the barriers themselves protect the sensitive marsh behind the islands from erosive wave action. Never-the-less, Louisiana's deltaic plain accounts for 80% of the nation's total tidal wetland loss (Roberts, 1994).

Louisiana's bar-built estuaries are broad and shallow with mean depth's of only a meter or two. The upper ends of these systems often consist of a region of multiply-connected marsh intersected by bayous or creeks, tidal channels and streams. The regional topographic gradient is very small, so the marsh is highly susceptible to flooding. The lack of detailed bathymetry and topography from the region places a significant restriction on our ability to model accurately the subtleties of the circulation features of these systems. The dominant oceanographic feature of the inner shelf in this region is the Louisiana Coastal Current (LCC) (Wiseman et al., 1986). This low salinity current carries much of the fresh water discharged by the Mississippi River westward

along the coast in front of the tidal passes connecting the local estuaries with the Gulf of Mexico. It is separated from the mid-shelf water by a strong haline front. Tidal range in the region is small (less than 60 cm) and strongly diurnal (Marmer, 1954). Never-the-less, tidal currents are important aspects of the dispersive environment of the system (McKee et al, 1992). In summer, steady southeasterly winds dominate the region with time scales of a few weeks (Hsu and Blanchard, 1993). In addition, strong diurnal sea breeze systems develop along the coast. In winter, winds associated with the recurrence of cold air outbreaks with time scales of 3 to 10 days dominate (DiMego et al, 1976). These latter systems drive important meteorological tides which can cause sea level to change by up to a meter (Chuang and Wiseman, 1983; Schroeder and Wiseman, 1986) resulting in important flooding of the marsh and consequent stressing of the associated plant community. Because of natural and man-made levees, these systems largely are isolated from direct river input from the Mississippi-Atchafalaya system. Local rainfall is large, but so too is evaporation. Runoff to these estuaries is poorly gauged and this forcing represents a significant gap in our understanding of the dynamics of the systems.

Louisiana's estuaries are nursery grounds for significant commercial and recreational fisheries, including economically important shrimp and menhaden fisheries. Historically, they have been the site of increasing levels of human activity related to exploration and production of oil and gas. Finally, they are home to an important local culture which the state and the nation have an interest in preserving.

Management decisions concerning these environments will concern control of the dominant physical processes, sediment erosion, transport and deposition, eutrophication, and recruitment to the estuarine nursery grounds, among others. Arguably the most accurately modeled, at this point in time, are the physical processes. There is a moderately long history of physical modeling in Louisiana estuaries. The US Army Corps of Engineers has had a long and successful history of controlling the water flow and salinity regime within the lower Mississippi River. An early physical model of Barataria Bay is briefly described by von Arx (1957). Early numerical models of specific Louisiana estuaries have been described by Hacker (1973), Hart (1978) and Hart and Murray (1978), among others. Wiseman and Swenson (1989) discuss tidal prism models of Terrebonne Bay and Barataria Bay while aspects of the exchange of waters between estuaries and the coastal ocean have been statistically modeled by others (Lee et al, 1990; Chuang and Wiseman, 1983; Schroeder and Wiseman, 1986). To date, though, no one has developed a modeling framework for these systems which has been carefully calibrated, skill-assessed and applied to practical problems. The work described herein is an initial effort to do just this.

This study was initiated in order to examine detailed physical characteristics of these estuaries using a modeling approach, and to identify a class of models which can be used to study the environmental characteristics of these estuaries. This model study arose from a recent interdisciplinary study of physical processes responsible for wetland loss in coastal Louisiana (Wiseman and Inoue, 1994). Specifically, in the present study, circulation, transport and flushing processes in two significantly different estuaries, namely Terrebonne/Timbalier Basin and

Barataria Basin are examined using a depth-integrated, two-dimensional numerical model. While the results of these studies are confined to discussions of the advective-dispersive regimes observed, the resulting insights have important implications for other problems, such as the susceptibility of different regions of the estuarine systems to eutrophication and noxious blooms. Then, the same depth-integrated hydrodynamic model is coupled to an ecological model to study an ecological process in Fourleague Bay, an estuary significantly impacted by the nearby Atchafalaya River.

CHAPTER 2

TERREBONNE/TIMBALIER BASIN STUDY

2.1 Background

Terrebonne/Timbalier Basin (Figures 1a and 5b) is a broad shallow estuary located west of the Mississippi Delta. Bottom depths are typically shallower than 2.5 m. The bay has three openings to the Gulf of Mexico through Whiskey Pass, Little Pass Timbalier, and the main pass encompassing Cat Island Pass and Wine Island Pass. A ship channel runs NNW from Cat Island Pass and is maintained at depths between 5 and 6 m. A natural channel, with depths of approximately 2.5 m extends NNE from Cat Island Pass towards Lake Barre. The estuary results from subsidence, erosion and reworking of sediments from the old LaFourche Delta lobe of the Mississippi River (Penland, 1990). In terms of sediment inputs, the Terrebonne/Timbalier Basin is impacted very little by the annual flood cycle of the Mississippi River in comparison to the Atchafalaya basin located further to the west (Roberts, 1994). Hence, Terrebonne/Timbalier Basin is known as a "sediment-poor" area (Roberts, 1994). Several bayous and canals supply freshwater to the bay, and they are poorly gauged. Those bayous and canals receive fresh water primarily from local runoff. Direct freshwater input from the local rivers to the bay appears to be small (Prager, 1992). Estimates of monthly excess precipitation over the local catchment basin are generally less than 0.5 cm (Prager, 1992).

From early 1990 until the end of the year, five mooring sites in Terrebonne Bay (Figure 1b) were occupied (Wiseman and Inoue, 1993). Due to the shallow water, most mooring sites were instrumented by one Endeco 174 current meter at mid-depth. Site 3 was instrumented with near-surface and near-bottom meters. They recorded average current speed, instantaneous current direction, temperature and conductivity. Salinity was estimated from the latter two parameters. Instruments were serviced every 6 to 8 weeks. The water column was generally well-mixed.

Temporal variability in the recorded time series is characterized by the velocity spectra shown in Figure 2. They exhibit a strong diurnal tide signal with a significant semi-diurnal signal. They also exhibit a flattening of the spectra within the weather band, indicating significant variability. Multiple processes contribute to the observed variability within the weather band. Ekman set-up and set-down at the coast forces water exchange between the bay and the adjacent Gulf of Mexico. The orientation of the principal axes of current variability is strongly associated with the local bathymetry. For the forty-hour low-passed currents, the principal axes' orientation showed significant variability in direction from deployment to deployment within the bay. This variability is coherent with the wind. It appears that the broader scales involved in the bay allow wind stress to make an important contribution to the direction of low-passed current.

The salinity spectra, shown in Figure 3, exhibit peaks at the tidal frequencies due to tidal advection. Within the weather band, salinity variability is still significantly controlled by advection. Observed coherence between currents and salinity was variable from site to site within

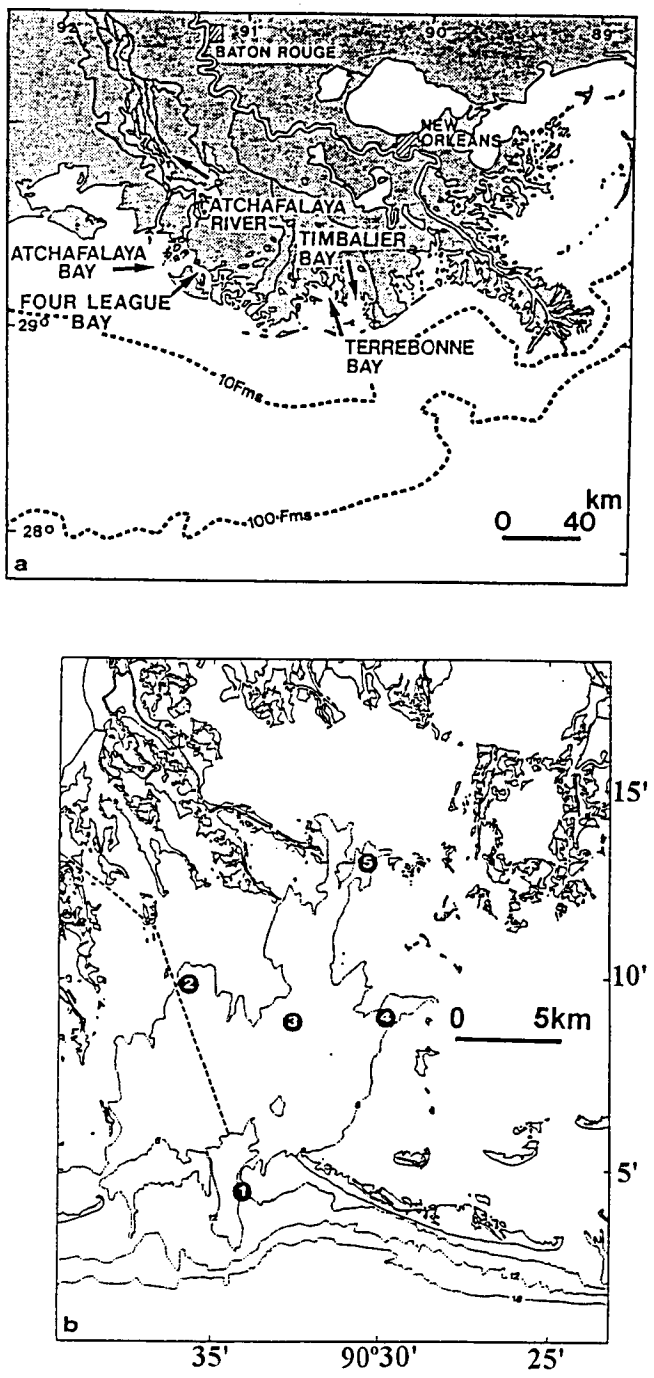

Figure 1. (a) Location map of study area. (b) Chart of Terrebonne/Timbalier Bay. Numbered dots indicate mooring locations. Dashed line is a dredged ship channel.

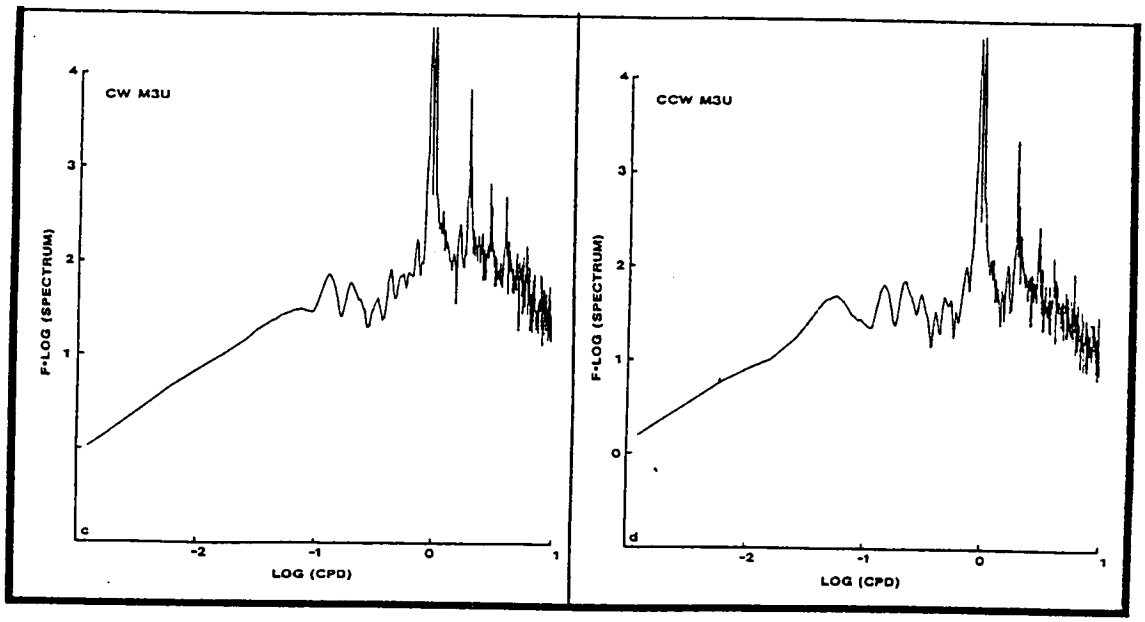

Figure 2. Clockwise (CW) and counter-clockwise (CCW) variance-preserving velocity spectra from a 203-day record at site 3. Spectra were estimated by smoothing the periodogram with an 11-point triangular running filter. Spectra units are ($cm^2\ s^{-2}$).

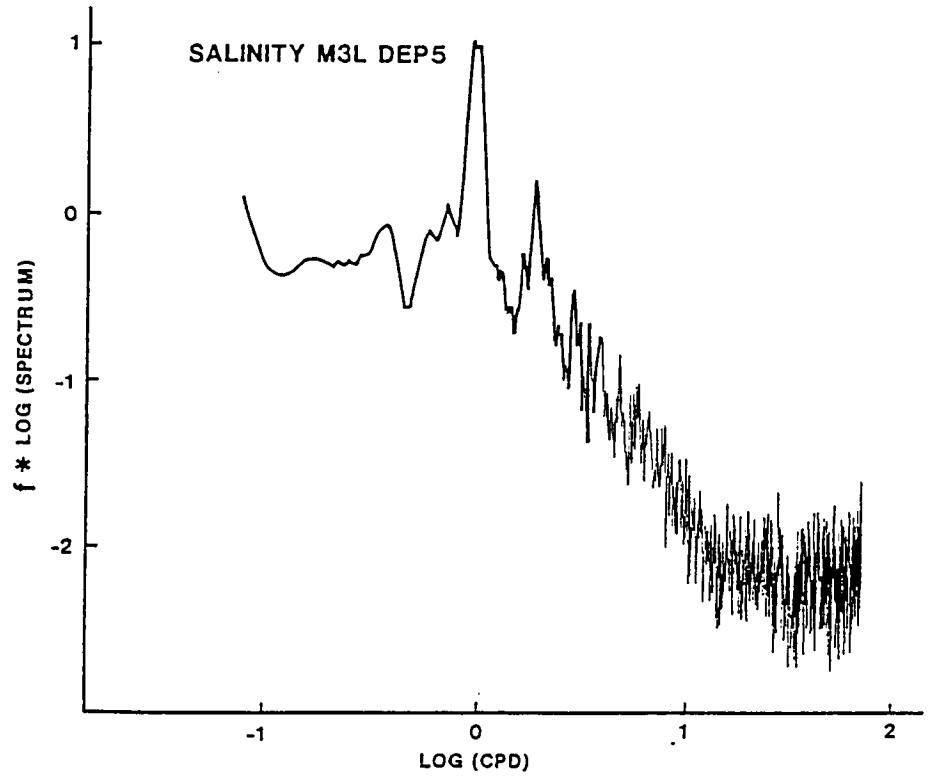

Figure 3. Variance-preserving salinity spectrum for a 77-day record from site 3 (After McKee et al., 1992). Spectrum was estimated by smoothing the periodogram with an 11-point triangular running filter.

the bay. For example, salinity was coherent with eastward currents and water level at site 4 near frequencies of 0.2 cpd while at site 2 the salinity was coherent with the northerly currents within the same frequency band. The importance of topographic control of the flow field by both the dredged ship channel and the western edge of the bay are probably indicated by the latter coherence. At the lowest frequencies observed, the salinity in the bay is correlated with Mississippi River discharge (Figure 4). Anomalous spikes of high salinities in early August 1990 appear to be associated with a breakdown of the LCC and an intrusion of shelf water. Following this event, the high salinity water was gradually flushed from the bay by tidal and wind-driven exchange processes. The sustained high salinities observed for roughly 100 days at the end of 1990 are associated with a period of low Mississippi River discharge. A rapid rise in discharge at the beginning of 1991 is followed within approximately one month by decreasing salinities. As the runoff drops, salinity begins to increase. The lag between discharge and bay salinity is variable and reflects the time required by fresh water to flow from the gauging station to the river mouth, along the coast to the estuary's tidal passes, and to disperse into the estuary.

2.2 Numerical Model Formulation

A two-dimensional depth-integrated hydrodynamic model is used to study circulation in the Terrebonne/Timbalier Basin. Use of a two-dimensional depth-integrated model is deemed adequate considering the generally well-mixed water column and insignificant amount of freshwater runoff inside the bay. Our focus here is on time-scales of a few days which are often dominated by synoptic weather forcing (3 ~ 10 days), therefore the baroclinic pressure gradients were neglected (Elliott and Reid, 1976). The model equations of motion and continuity are written on Cartesian coordinates. The model equations are written for depth-integrated transports (e. g., Leedertse, 1967);

$$\frac{\partial U}{\partial t} + \frac{\partial}{\partial x}\frac{U^2}{H} + \frac{\partial}{\partial y}\frac{UV}{H} - fV = -gH\frac{\partial \zeta}{\partial x} - g\frac{\frac{U}{H}\left[\left(\frac{U}{H}\right)^2 + \left(\frac{V}{H}\right)^2\right]^{1/2}}{C^2} + \frac{\tau^x}{\rho} + A\nabla^2 U$$

$$\frac{\partial V}{\partial t} + \frac{\partial}{\partial x}\frac{UV}{H} + \frac{\partial}{\partial y}\frac{V^2}{H} + fU = -gH\frac{\partial \zeta}{\partial y} - g\frac{\frac{V}{H}\left[\left(\frac{U}{H}\right)^2 + \left(\frac{V}{H}\right)^2\right]^{1/2}}{C^2} + \frac{\tau^y}{\rho} + A\nabla^2 V \qquad (1)$$

$$\frac{\partial \zeta}{\partial t} + \frac{\partial U}{\partial x} + \frac{\partial V}{\partial y} = 0$$

where

$$H = h + \zeta$$

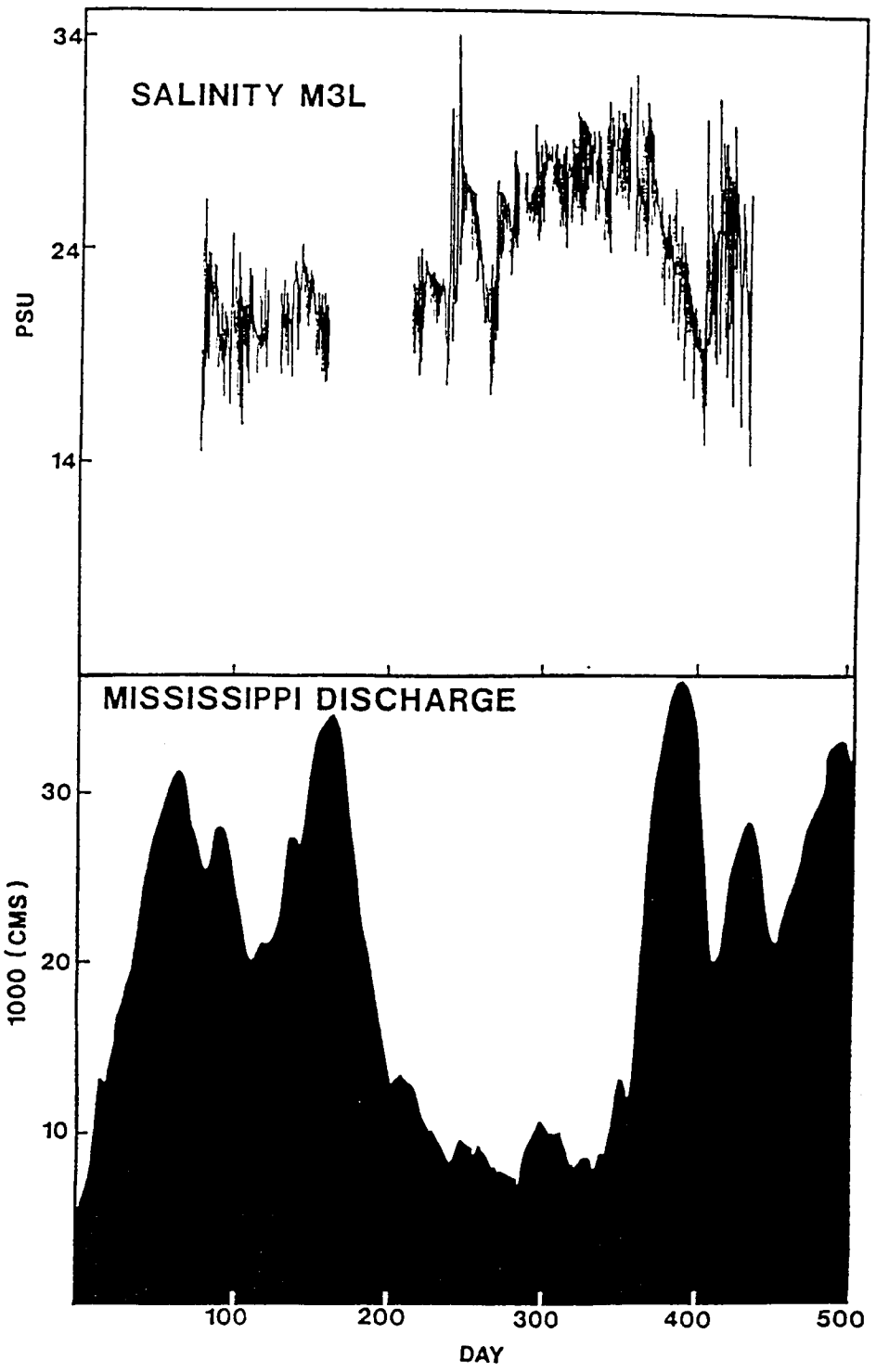

Figure 4. (a) Salinity time series from site 3. (b) Time series of Mississippi River discharge at Tarbert Landing, LA. The time origin (day 0) for these plots is 1 January 1990.

$$U = \int_{-h}^{\zeta} u dz$$

$$V = \int_{-h}^{\zeta} v \, dz$$

where t denotes time, x, y, and z are Cartesian coordinates, u and v are the current components in the x and y directions, respectively, ζ is elevation of the free surface above mean sea level, h is the undisturbed depth of the water, f is the Coriolis parameter (assumed to be a constant), g is the acceleration due to gravity, τ^x and τ^y are the x and y components of wind stress, respectively, ρ is the density of water (assumed to be a constant), A is the horizontal eddy viscosity, and C is the Chezy coefficient which is depth dependent. The bottom roughness is introduced through Manning's n coefficient, such that the Chezy coefficient is evaluated as

$$C = \frac{1}{n} H^{1/6}$$

These model equations are subjected to boundary conditions to complete the model formulation. At land boundaries, no normal flow and no-slip boundary conditions are used. At the open boundary, sea level height is specified. Wind forcing is assumed to be spatially uniform over the entire model domain.

The model equations are discretized on the staggered mesh grid C of Arakawa (Mesinger and Arakawa, 1976). The numerical scheme adopted here is the Grammeltvedt C scheme (Grammeltvedt, 1969) which conserves mass and total energy. A Leapfrog scheme is used for time integration with an Euler scheme inserted at regular time steps to eliminate the computational mode due to the central time differencing. The frictional terms are lagged in time for numerical stability.

The model bathymetry was taken from the Nautical Charts (Scale 1:80,000), and the coastal boundaries were approximated on the model grid as closely as possible (see Figures 5a and 5b). Due to the ongoing land loss which has taken place since the chart was published, some modification of the model land geometry was necessary on the basis of a series of recent aerial photographs. The model grid spacing between like variables is taken to be 463 m, and the time step used for integration is 10 s. The horizontal eddy viscosity used is 10 $m^2 s^{-1}$. The southern boundary of the model domain is taken outside the bay in order to permit less restrictive model simulation of flow fields near the entrances to the bay.

2.3 Computation of Particle Trajectories

Often it is difficulty to interpret an Eulerian velocity field in terms of transport processes, which are inherently Lagrangian. However, a numerical hydrodynamic model can be used to

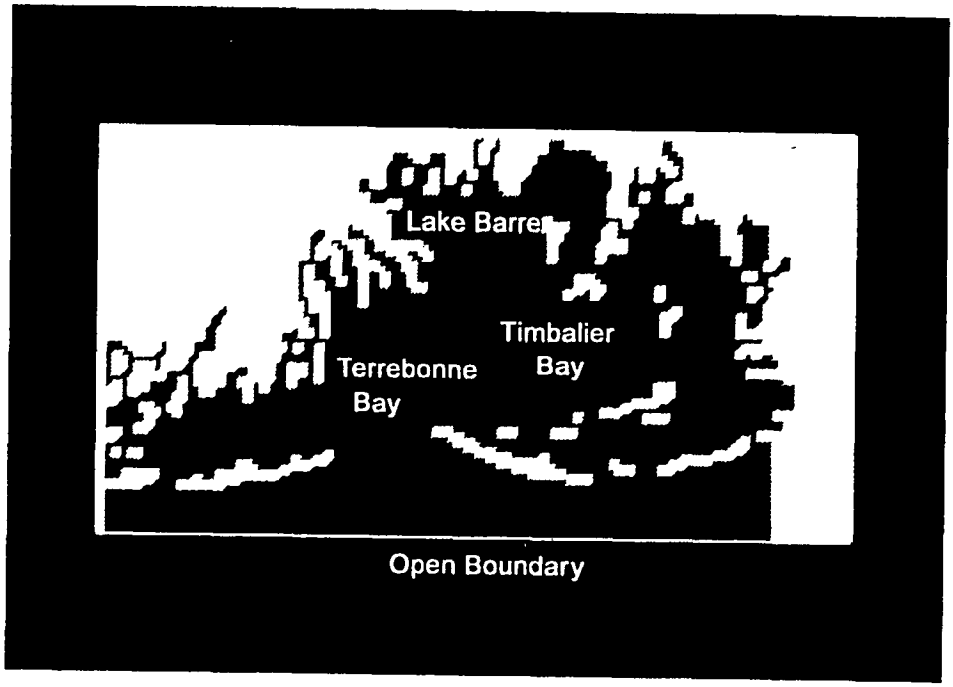

Figure 5a. Model geometry of the Terrebonne/Timbalier Bay Model. The southern boundary is open.

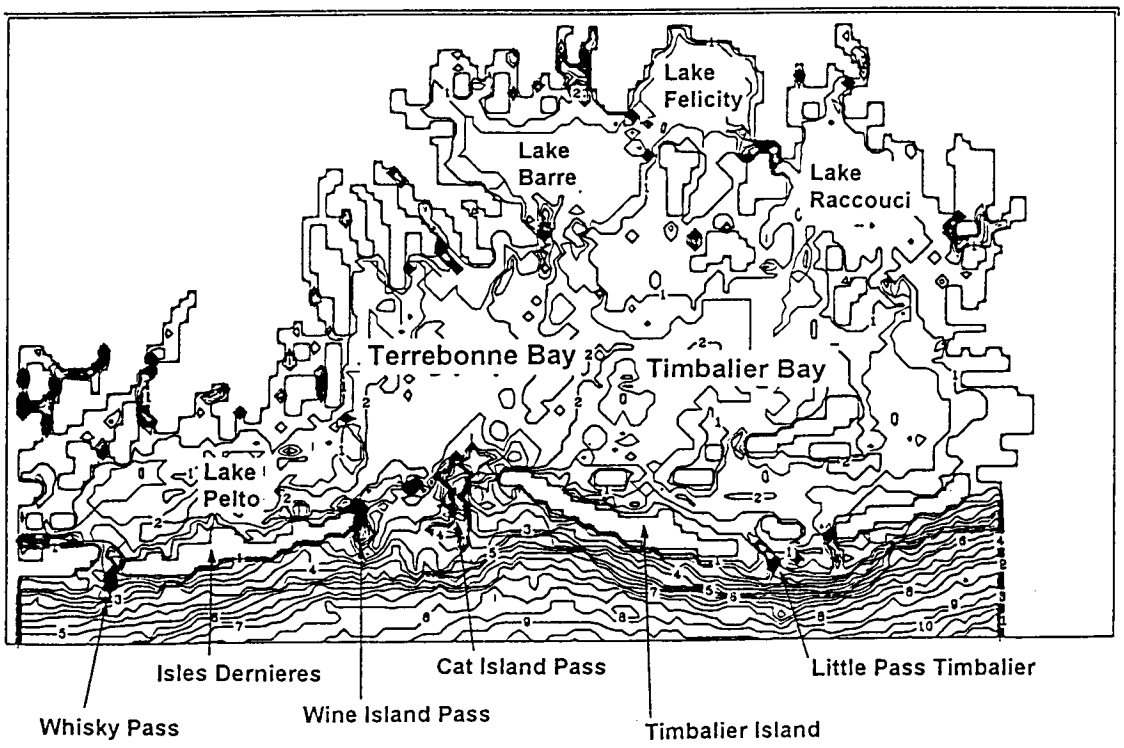

Figure 5b. Model bathymetry of the Terrebonne/Timbalier Bay Model. Bottom bathymetric contours are shown at every 0.5 m.

calculate the Lagrangian movement of a number of labeled particles released in the model in order to directly examine transport processes (e. g., Awaji et al., 1980; Ridderinkhof, 1990; Signell and Butman, 1992; Kapolnai et al., 1996).

In recovering Lagrangian information from an Eulerian data set, careful consideration must be given to limiting computational errors to relatively small values compared to the amplitude of the computed quantity. The objective is to recover Lagrangian particle trajectories, Xn(t), given an Eulerian velocity field, **u** (**x**(t,n),t), from the depth-integrated two-dimensional hydrodynamic model. To do this, the following equation has to be integrated.

$$\frac{dx(t,n)}{dt} = u(x(t,n),t) \qquad (2)$$

where particles are identified as n =1, 2, ..., and the vectors **x** and **u** give the 2-D particle positions and velocities. The computed trajectories can be quite sensitive to the details of the algorithm used (e. g., Haidvogel, 1982).

In order to integrate Eq. (2), first, the velocity **u** has to be estimated at the location of the particle, which is, in general, located between neighboring grid points. Then, the time integration must be computed. Although there are various schemes available for time integration, in this study a simple Euler scheme (Mesinger and Arakawa, 1976) is used. Those simple schemes can be made quite accurate if sufficiently small timesteps are used. Previously, Bøning and Cox (1988) demonstrated that in integrating (2) using the simple Euler scheme, no further significant change in the computed particle trajectory is reached when m, the number of time steps for the integration to cover one grid distance, exceeds O(100). In this study, it was decided to use a time step of integration of (2) equal to Δt, the time step used to integrate the hydrodynamic model, i. e. 10 s. In this study typically, $\mathbf{u}_{max} = O(1.5\ ms^{-1})$, and $\Delta x = \Delta y = 463$m, giving m $\geq O(300)$. Therefore, the use of the simple Euler scheme is expected to produce sufficiently accurate results.

2.4 Model Calibration

The main objective of this model study is to simulate circulation as realistically as possible. Current meter data collected at the five mooring sites were used for model calibration. Shear observations at one site indicated that strong shear and tidal straining of the density field were only present during isolated and short-lived freshets. Therefore, for the purpose of model-observation comparison, currents measured at mid-depth by the current meters were considered to represent depth-averaged currents.

The model was forced by the observed wind and the sea level height data for a period when current meters were producing usable data. For this calibration, the period between 03/21/90 and 03/27/90 was chosen. Wind stresses acting on the sea surface were estimated from wind measurements made at Isles Dernieres (Hsu and Blanchard, 1991). The following empirical relationship derived for Fourleague Bay, a neighboring estuary immediately to the west,

(S. A. Hsu, unpublished data, 1992) is used to convert from wind speed to wind stress.

$$\tau = \rho_a u_*^2 \text{ and } u_* = 0.037\, u_{10} + 0.03$$

where τ is the wind stress, ρ_a is the density of air, u_* is the friction velocity, and u_{10} is the wind speed (m s^{-1}) measured at 10 m height.

Sea level heights along the open boundary are estimated from the observed bottom pressure record collected at site 1. It was assumed that the sea level height measured by the bottom pressure recorder at site 1 represents the incoming sea level signal propagating from the open boundary toward the bay entrances. Initial calibration runs were made by applying the sea level signal measured at site 1 along the open boundary with various values of amplification and phase shift, and the observed sea level records at site 1 were compared to the corresponding model sea level height at site 1. After several calibration runs, it was decided to use the sea level signal measured at site 1 along the open boundary without any amplification and phase shift.

The model was spun up from rest using the observed wind and sea level height. Hourly observed wind and sea-level records were used, and linear interpolation was used to compute wind stress and sea-level height at any particular time step in between. Spin-up time for the model could be estimated as the time required for the tide to propagate from the open boundary all the way up to the other end of the model domain and to propagate back to the open boundary. For the model domain used here, a spin-up time of 24 hours is considered to be sufficient. Various test runs indicate that the initial disturbances due to model initialization appear to have died down after 24 hours.

Next, a series of numerical experiments were carried out to examine the impact of varying the magnitude of the bottom friction with the objective of identifying a realistic bottom friction. A Manning's n value of 0.07 was found to yield simulated currents which are in close agreement with the observed currents. This value is two or three times larger than a typical Manning's n identified for other estuaries. A possible reason could be the shallowness of the bay that could give rise to enhanced bottom friction due to the combined effect of currents and the surface wave field (e. g., Signell et al., 1990; Davies and Lawrence, 1995), which is not explicitly accounted for in the present model formulation. Another reason could be the presence of fine-grained sediments found in the bay (Hebblewaithe, 1990). This Manning's n is much larger than 0.015 used by Prager (1992) in her application of the finite element circulation model of Wang and Connor (1975) to the same bay. However, Prager (1992) used a horizontal viscosity of 100 $m^2 s^{-1}$, in comparison to the 10 m^2 s^{-1} used here, suggesting that most of the energy dissipation in her model was due to the horizontal viscosity rather than to the bottom friction. Examples of model calibration are shown in Figure 6. Mean correlation coefficients between observed and simulated currents computed for east-west and north-south components at each of the five mooring sites generally range from 0.89 to 0.95. The only exception is site 5, which is located close to rather rough bottom topography in a deep channel. Presumably, the model does not have a sufficiently fine resolution to account for the rough neighboring bottom topography.

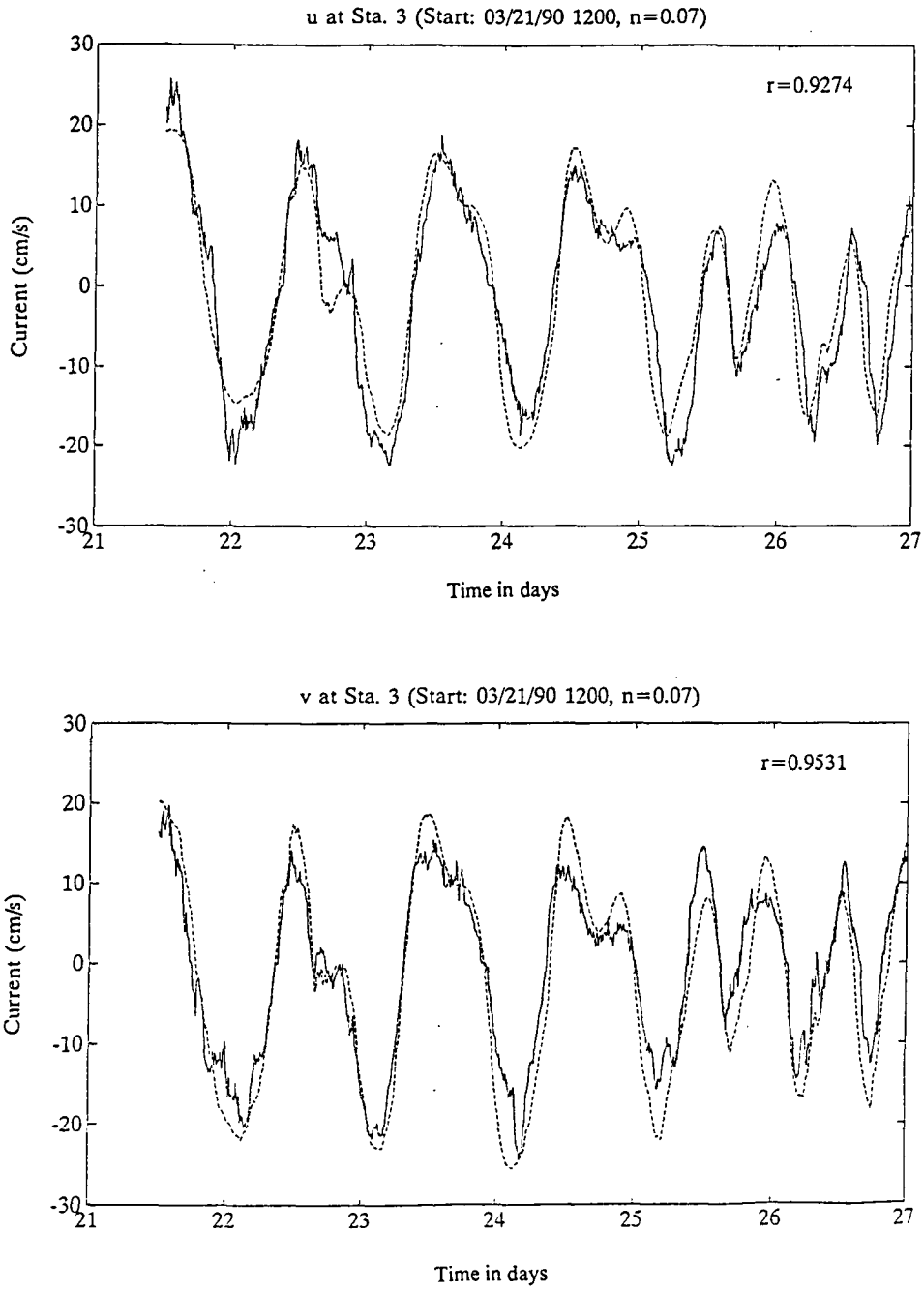

Figure 6. Observed (solid line) and simulated (dashed line) currents at Station 3 located in the middle of Terrebonne Bay for the period 03/21/90-03/27/90. East-west component (top), and north-south component (bottom). r is the correlation coefficient between the observed and simulated currents.

2.5 Model Simulation

Upon the completion of model calibration, the model was used to simulate the circulation inside the bay using the observed sea level height and wind data during May, 1990 (Figures 7 and 8). This period represents typical environmental conditions, predominantly southerly winds of 4~10 m s^{-1} with occasional shifts in wind direction associated with frontal passages (Figure 8). Figure 7 shows typical tidal range of 20 cm for equatorial tides and 80 cm for tropic tides. Starting from rest, the model was forced by the observed wind and sea-level height for the period 05/01/90-05/25/90. The first simulation day was considered as spin-up, and the model output for the subsequent period was analyzed. Examples of current fields simulated in the model are presented in Figures 9a through 9d. Figure 10 shows the maximum current speed simulated in the model while Figure 11 shows mean simulated current speed. It is evident in Figures 9 and 10, that stronger currents are concentrated in deeper parts of the bay, specifically in the deep parts of Terrebonne Bay extending from Wine Island Pass and Cat Island Pass toward Lake Barre. Despite the relatively small tidal range, due to their shallowness, strong tidal currents are observed in the shallow passes, i. e., Whiskey Pass and Little Pass Timbalier. In those shallow passes, tropic tidal currents could reach 130~190 cm s^{-1}. Those strong tidal currents appear to be dependent on the details of the local bathymetry used. Considering the uncertainties regarding the details of the local bathymetry, those strong currents could have been overestimated. However, it is reasonable to assume that strong tropic tidal currents of more than 100 cm s^{-1} could develop in those shallow passes. Extremely strong tidal currents are limited to the shallow passes, however. In the main pass encompassing Wine Island Pass and Cat Island Pass, maximum tropic tidal currents are usually limited to 70~80 cm s^{-1}. During equatorial tides, currents on the order of 20 cm s^{-1} could develop in a large portion of the bay while in the tidal passes they could reach 50~60 cm s^{-1}. In general, during tropic tides, current speeds could easily be double those during equatorial tides. Strong lateral shear in tidal currents could also develop in the vicinity of the entrances (Figures 9 and 11). In terms of relative volume transport through each entrance into Terrebonne/Timbalier Bay, on average, Wine Island Pass-Cat Island Pass dominates, accounting for nearly 60% of the total inflow into the bay, while the remaining inflow is equally split between Whisky Pass and Little Pass Timbalier, each accounting for 20% of the total.

Local wind significantly impacts circulation in the bay. Figure 9b illustrates the influence of the southwesterly winds (6~8 m s^{-1}) (Figure 8) in forcing a general eastward drift in the bay circulation during a equatorial tide. It should be noted that the real influence of the wind forcing includes not only the impact of local wind forcing directly acting on the bay but also the wind influence acting on the shelf that could surely force significant wind set-down or set-up outside the bay that has been incorporated into the sea-level forcing applied at the southern open boundary.

2.6 Flushing characteristics

Residence time defines the average time water particles remain in the sea area. This is an important measure in considering many practical problems such as, the dispersion of suspended

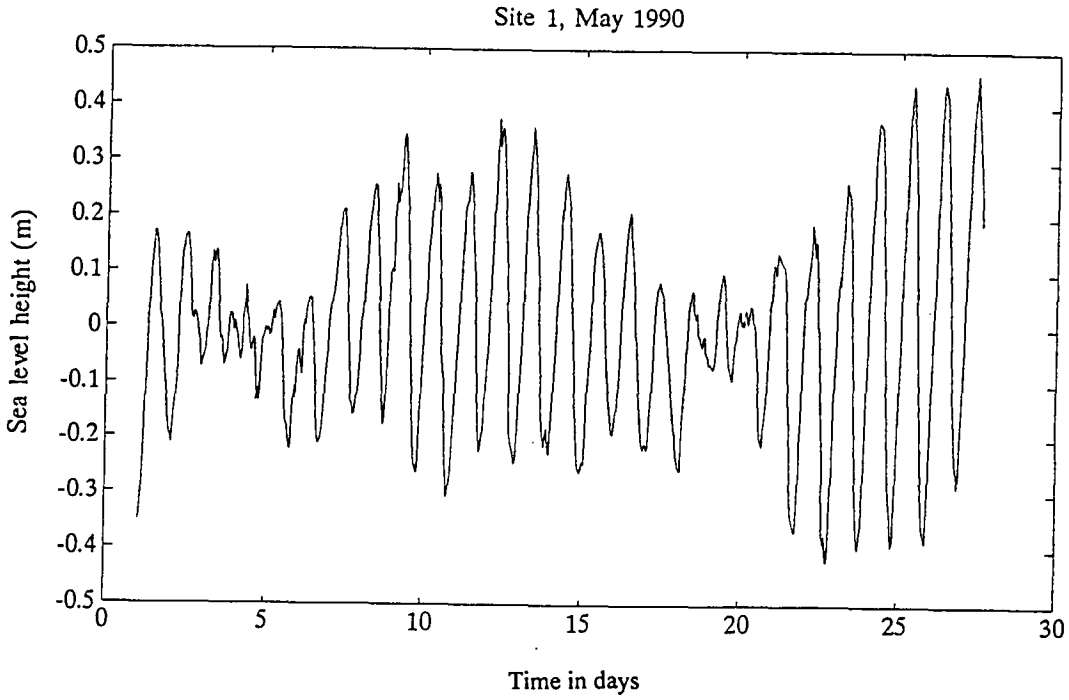

Figure 7. Observed sea-level height at site 1 during May, 1990.

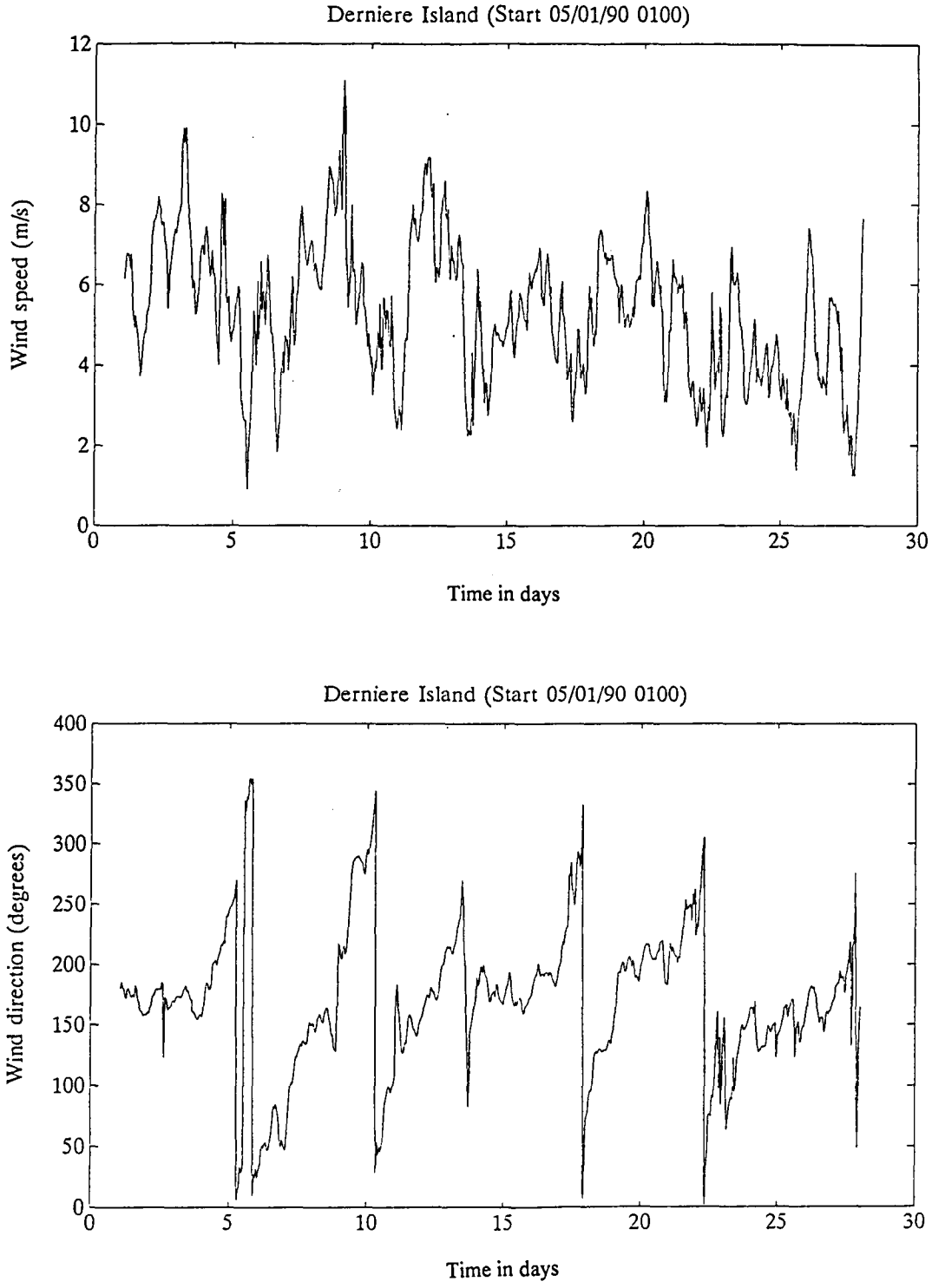

Figure 8. Observed wind at Isles Dernier during May, 1990. (a) Wind speed (m s^{-1}). (b) Wind direction (degrees measured clockwise from North).

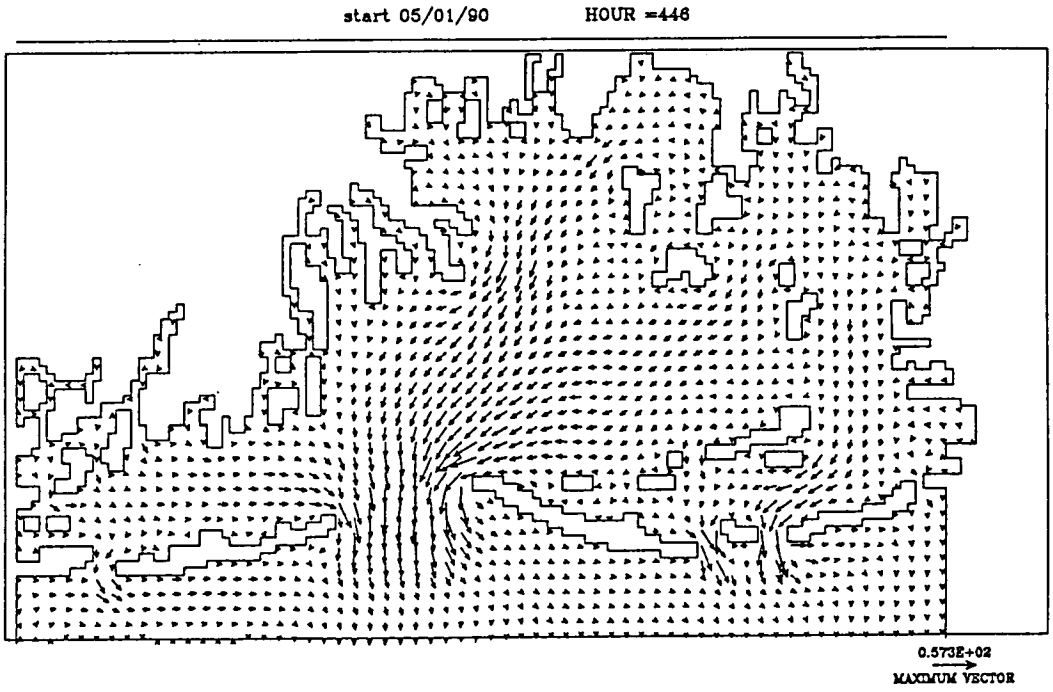

Figure 9a. Simulated currents in Terrebonne/Timbalier Bay. Maximum velocity vector (in units of cm s^{-1}) is shown at the bottom right. Vectors are plotted at every other grid points. Ebb tidal current at equatorial tide at 446 hr from 05/01/90. Maximum current speed of 69 cm s^{-1} in Little Pass Timbalier is not shown.

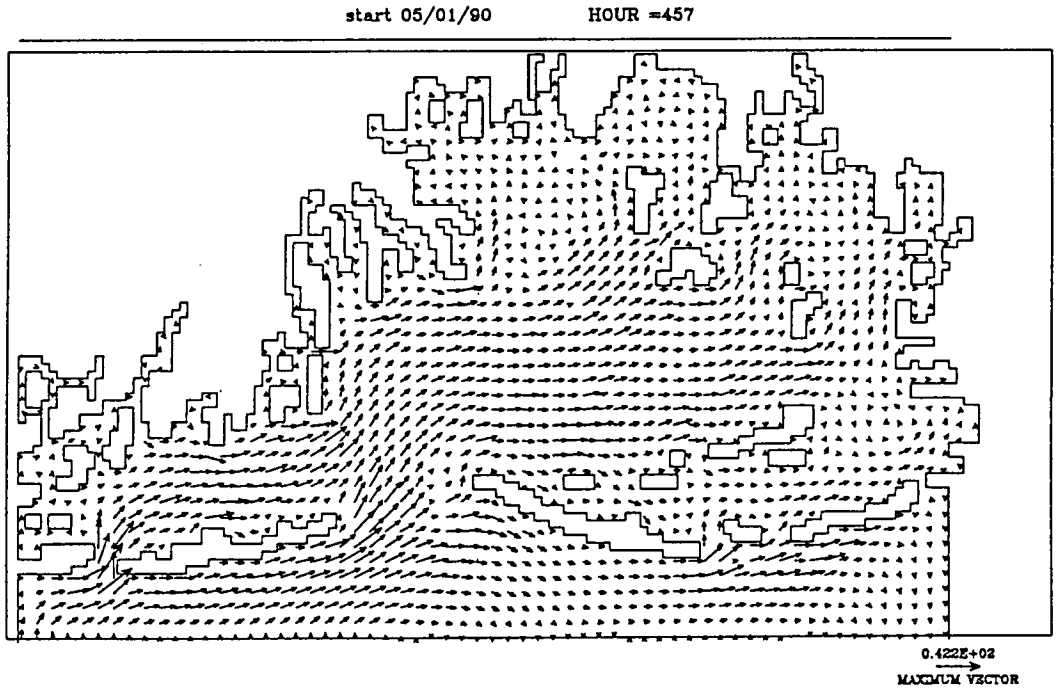

Figure 9b. Flood tidal current at equatorial tide at 457 hr from 05/01/90. Maximum current speed of 59 cm s^{-1} in Whisky Pass is not shown.

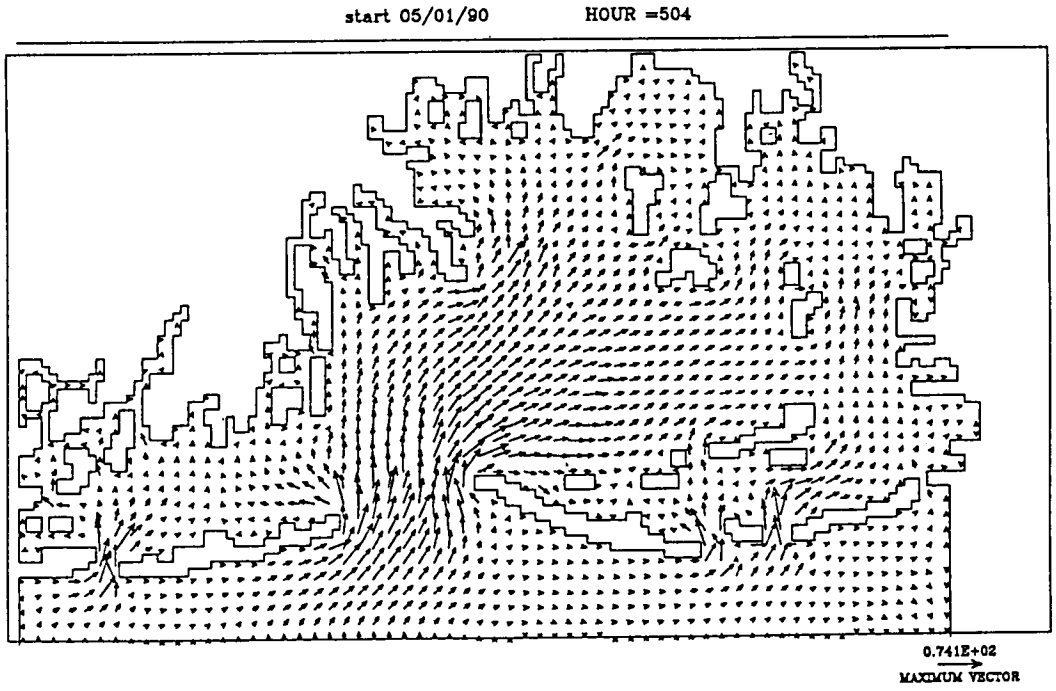

Figure 9c. Flood tidal current at tropic tide at 504 hr from 05/01/90. Maximum current speed of 110 cm s^{-1} in Whisky Pass is not shown.

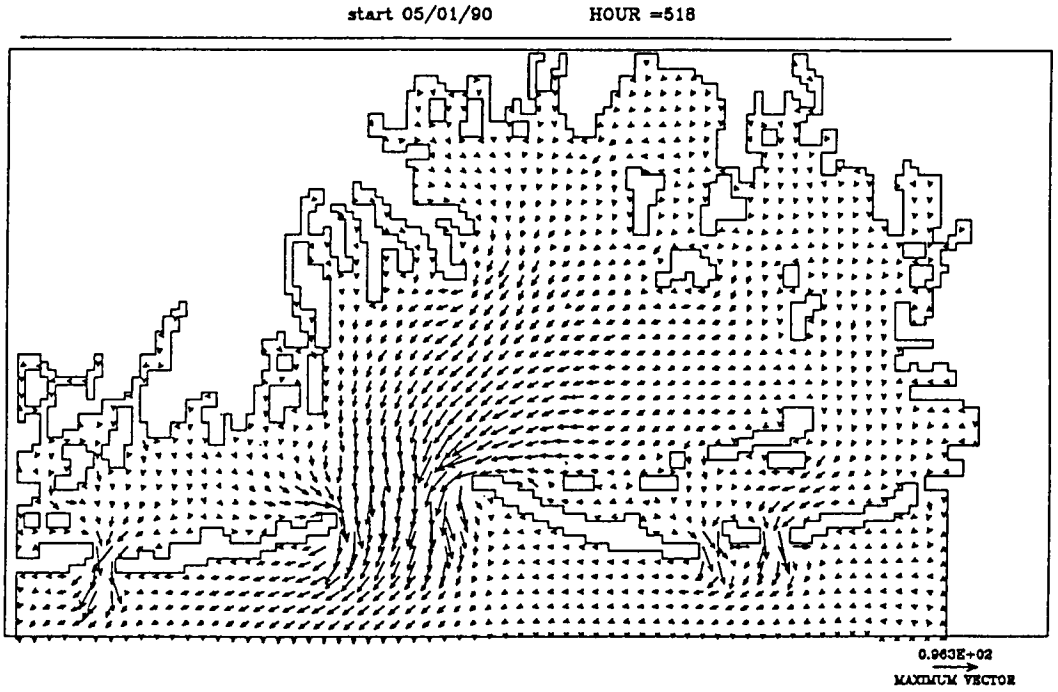

Figure 9d. Ebb tidal current at tropic tide at 518 hr from 05/01/90. Maximum current speed of 192 cm s^{-1} in Whisky Pass is not shown.

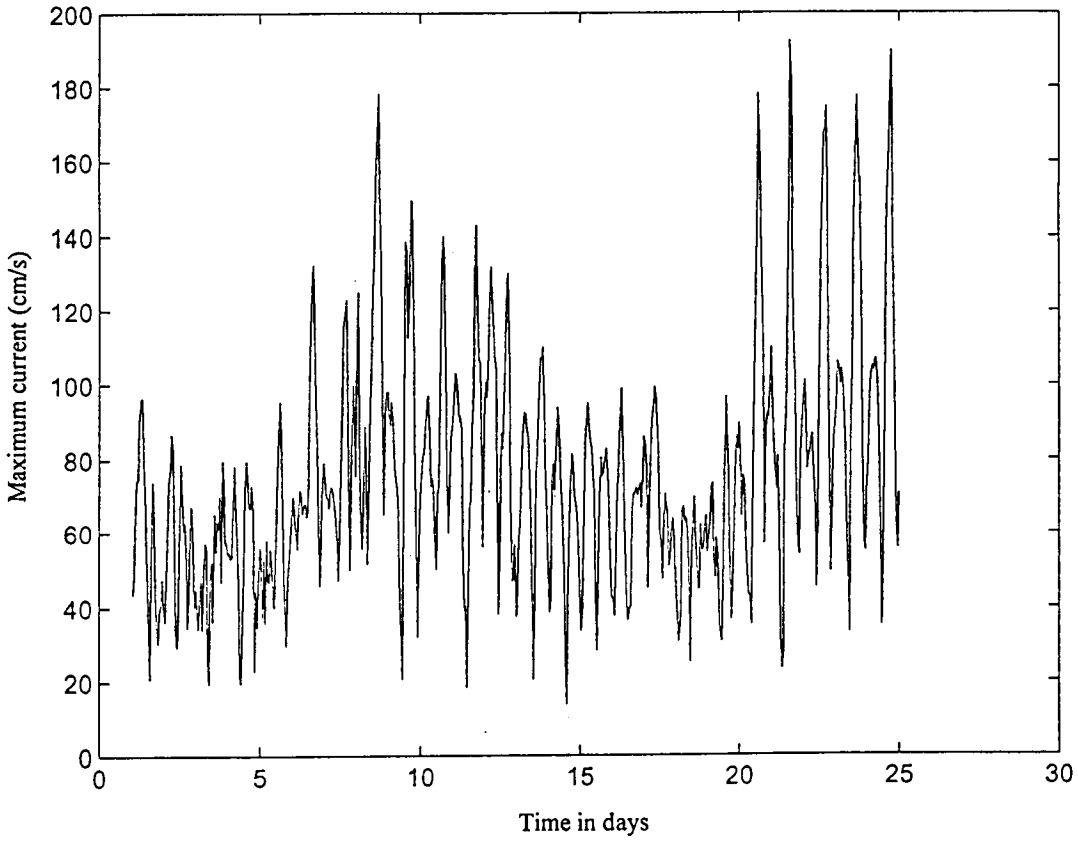

Figure 10. Maximum current speed (in cm s^{-1}) simulated for the period 05/01/90-05/25/90. Very large currents are always located either in Little Pass Timbalier or in Whisky Pass.

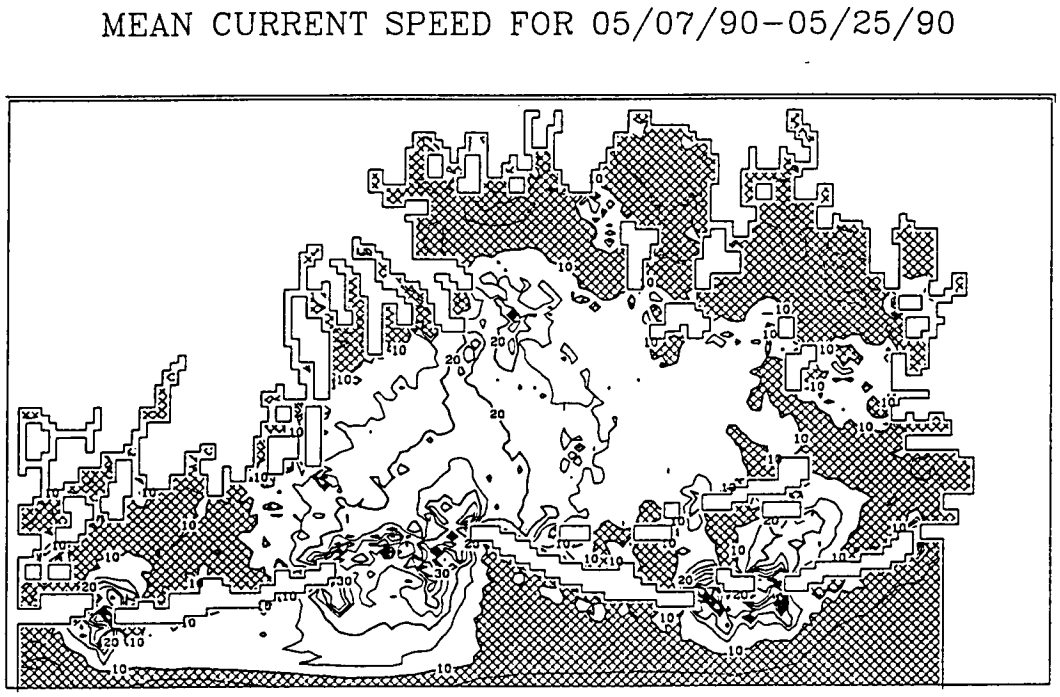

Figure 11. Mean simulated current speed (in cm s^{-1}) for the period 05/07/90-05/25/90. Hatched areas have current speeds less than 10 cm s^{-1}.

sediments, pollutants, and floating biological particles. In order to shed light on this issue, labeled tracer particles were released in the hydrodynamic model to represent water particles, and their trajectories were continuously tracked. In carrying out those tracer particle experiments, the objective was to examine details of advective transport processes by realistic currents driven by the observed tides and winds.

For this experiment, the same simulation period used in the previous section was considered. After a model spin-up of one simulation day, more than 5,000 particles were initially released with one particle at every grid point throughout the bay (Figure 12a). Then, the trajectories of the particles were tracked for the next 24 simulation days. The Lagrangian movements of the labeled particles clearly indicate the principal flow paths associated with subtidal circulation. For the simulation period examined, subtidal circulation includes a consistent inflow through Little Pass Timbalier and a variable inflow through Whiskey Pass. It should be noted that the winds, though variable, were predominantly from the southeast (Figure 8). A consistent outflow appears to take place through the main pass. Wind appears to dictate the flushing characteristics. Under more easterly wind conditions (Figures 12c and 12e), the outflow exhibits a more westward component, flowing out of the bay through Wine Island Pass and Whiskey Pass. While under more southerly wind conditions (Figure 12d), the outflow acquires a more southward direction, exiting the bay through Cat Island Pass.

The time it takes to flush out most of the tracer particles appears to be rather long. For example, after five days, 87% of the particles still remain within the bay. This drops to 70% after 10 days, 60% after 15 days, 51% after 20 days, and 41% after 25 days. If flushing time is defined as the time required to flush out a fraction $1-e^{-1}$ (=1-0.36788) of the particles initially deployed inside the bay (e. g., Ridderinkhof, 1990), it is estimated to be approximately 27 days. This estimate appears to be in good agreement with the time scale observed to flush out the high salinity water that first intruded into the bay in early August 1990 (see Figure 4 and section on Background). This is also in good agreement with previous estimates derived from tidal prism modeling (Wiseman and Swenson, 1989).

2.7 Particle Dispersion

Particle tracking also reveals that some initially adjacent particles end up widely scattered within a short time period while others tend to remain in proximity of each other for an extended period, giving rise to dispersion of particles (Figure 13).

Historically, many previous studies (e. g., Bowden, 1965; Okubo, 1967; Csanady, 1973) treated water dispersion in estuaries in terms of shear dispersion due to the combined effects of velocity shear and turbulence. However, more recent studies (e. g., Awaji, 1982) clearly demonstrated the dominant role of the tidal current in exchanging large amounts of water through the estuary entrance and, consequently, giving rise to extensive water dispersion. The tracer particle tracking technique has been used to study diffusion and dispersion characteristics in the ocean and lakes (e. g., Okubo et al., 1976; Ichiye et al., 1981; Krauss and Bøning, 1987; Bøning and Cox, 1988; Sanderson et al., 1995). For each cluster of tracer particles, the variances of the

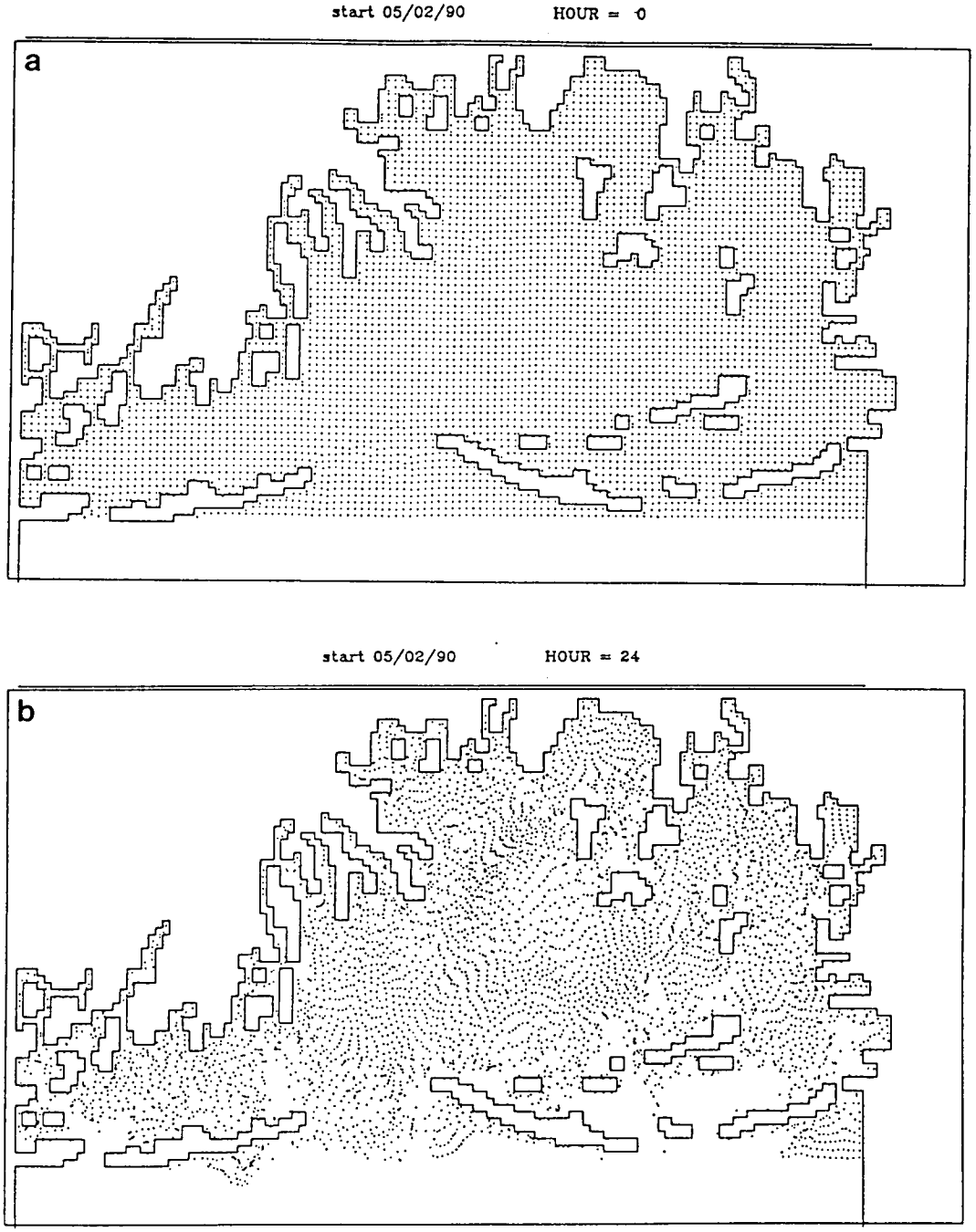

Figure 12. Distribution of tracer particles simulated for the period 05/02/90-05/25/90. a) At time of release (0 hr 05/02/90). b) After 24 hours.

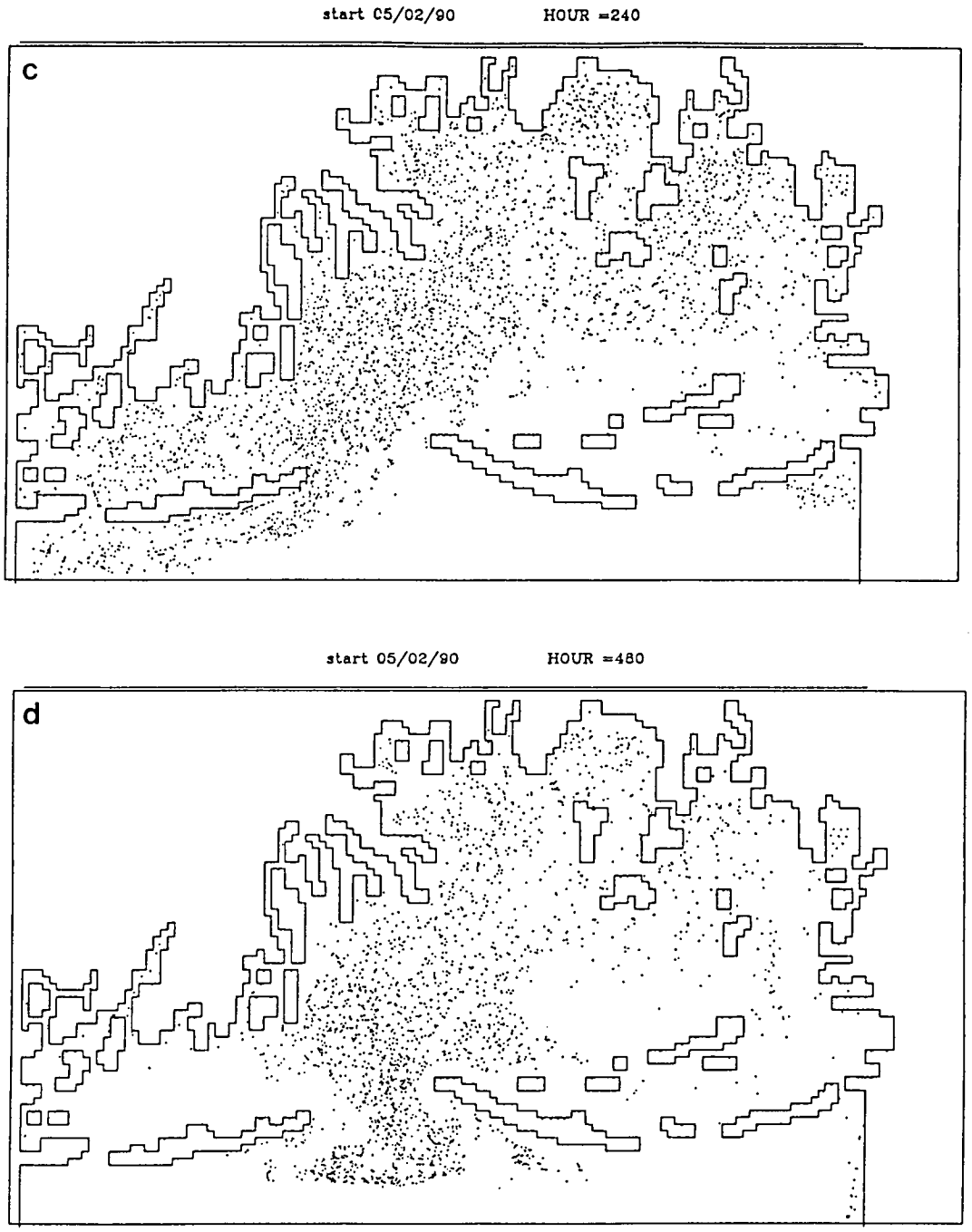

Figure 12. Distribution of tracer particles simulated for the period 05/02/90-05/25/90. c) After 240 hours. d) After 480 hours.

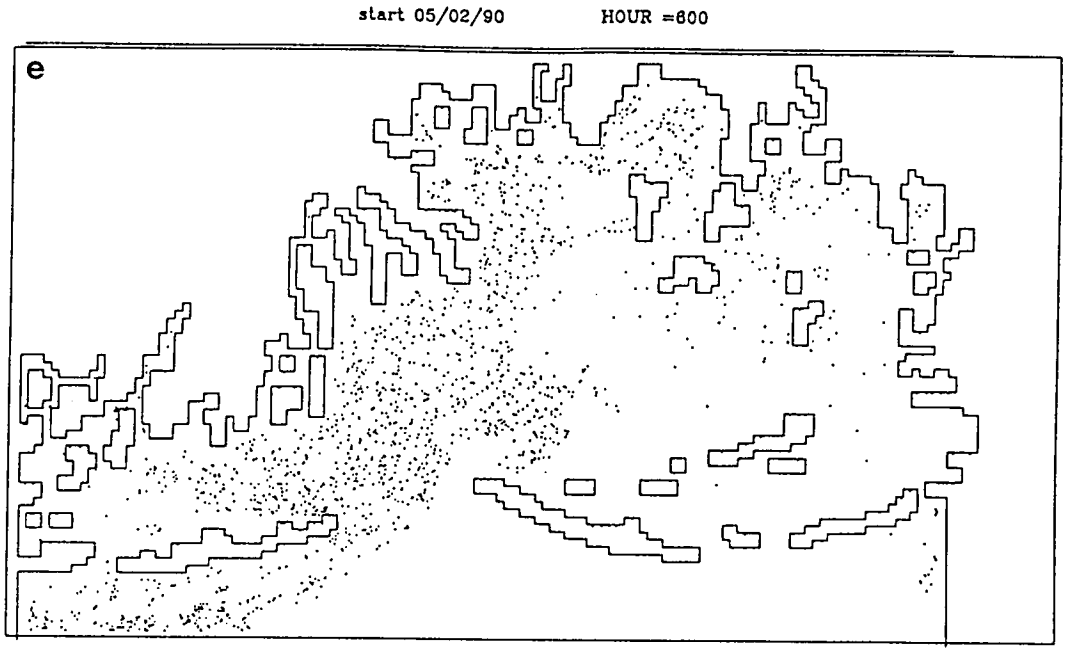

Figure 12. Distribution of tracer particles simulated for the period 05/02/90-05/25/90. e) After 600 hours.

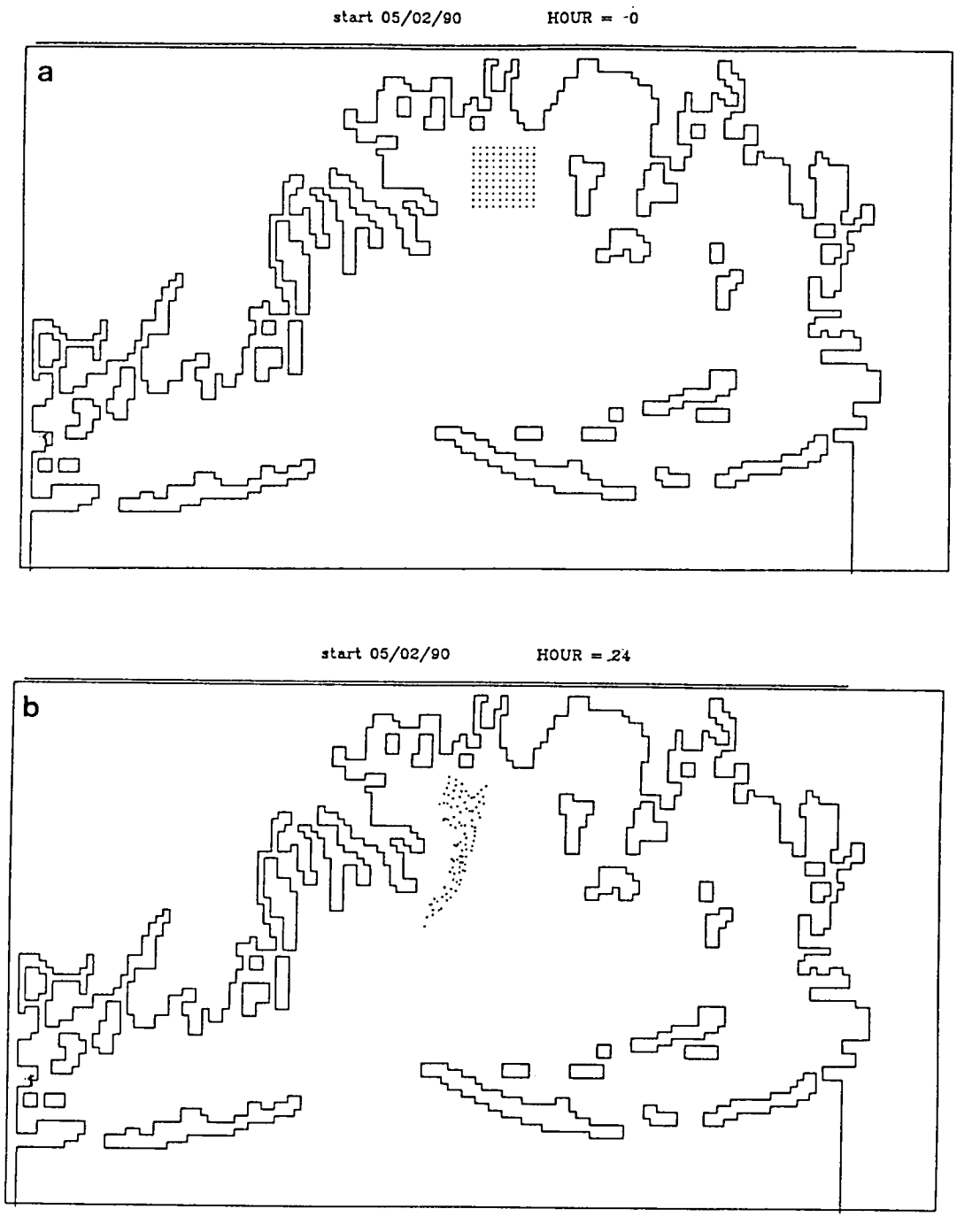

Figure 13. A subset of tracer particles used in Figure 12. a) At time of release (0 hr 05/02/90). b) After 24 hours.

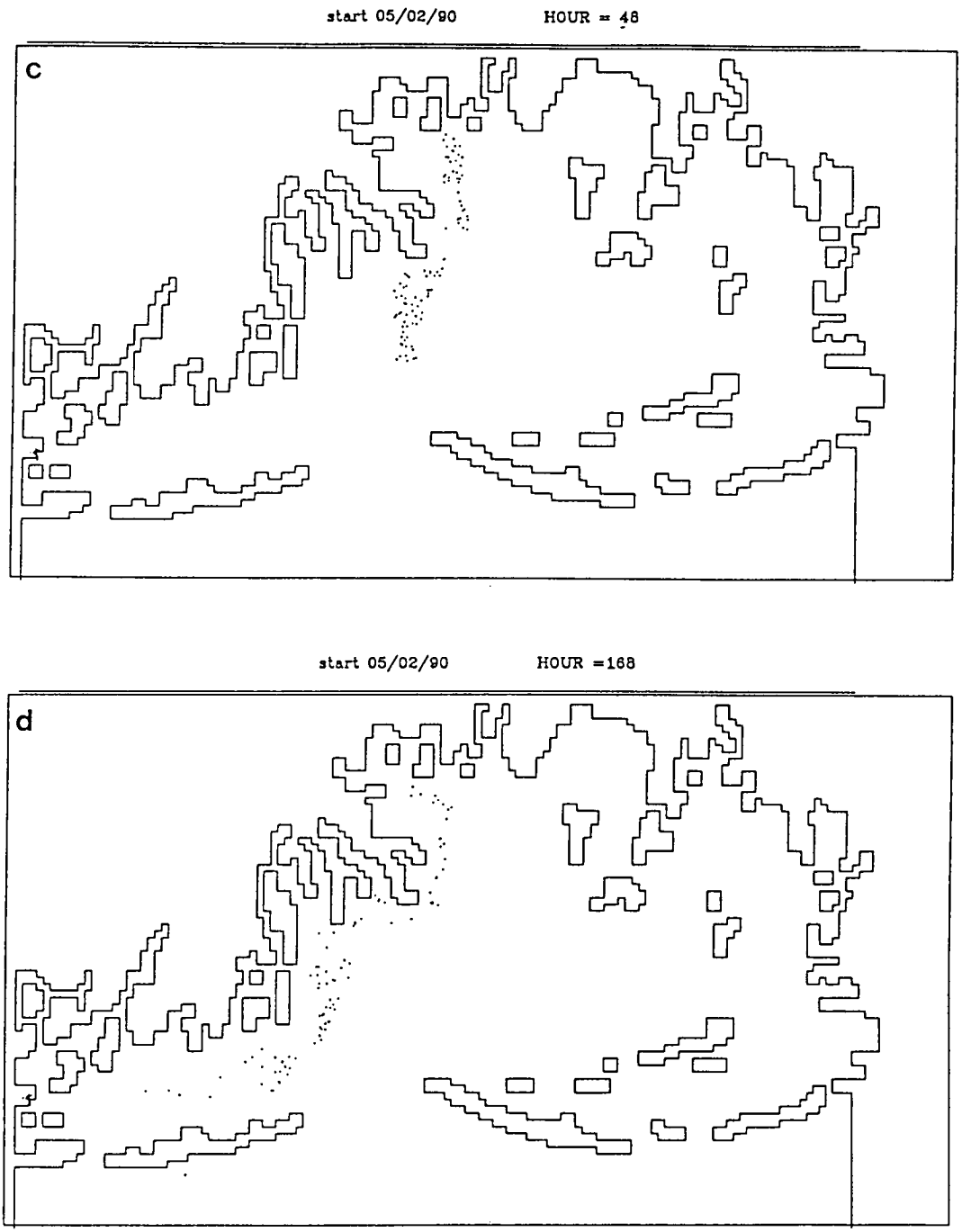

Figure 13. A subset of tracer particles used in Figure 12. c) After 48 hours. d) After 168 hours.

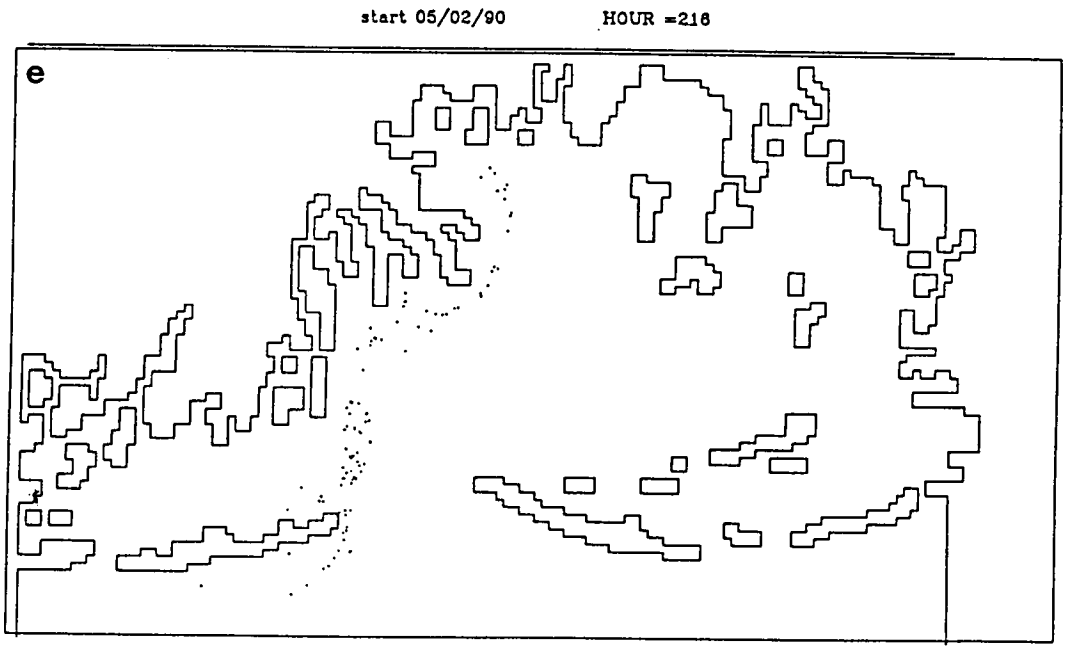

Figure 13. A subset of tracer particles used in Figure 12. e) After 216 hours.

particle positions σ_X^2 and σ_Y^2 along the major and minor axes of the cluster ellipse can be computed. The dispersive characteristics of a water mass can be described by the time evolution of these variances. The horizontal diffusivities K_X and K_Y along the major and minor axes are given by (Okubo, 1971),

$$K_x = \frac{1}{2}\frac{d\sigma_x^2}{dt}, \quad K_y = \frac{1}{2}\frac{d\sigma_y^2}{dt}$$

The mean horizontal diffusivity K_{XY} is defined as

$$K_{xy} = \frac{1}{2}\frac{d\sigma_x\sigma_y}{dt}$$

As was shown previously (e. g., Ridderinkhof, 1990), dispersive characteristics of a water mass are strongly dependent on time and space due to the significant spatial and temporal variations in the velocity field of the basin of interest.

In this study, the dispersion characteristics are evaluated by computing the time-dependent variances of the spread of 100 tracer particles released at various locations in the model domain. Figure 13 shows a time sequence of 100 tracer particles released in Lake Barre, and Figure 14 shows the time evolution of $\sigma_X\sigma_Y$ of those tracer particles. The particles were initially released in a square (Figure 13a). After one day, the shape of the cluster developed an elongation with the main axes oriented along the dominant tidal current direction (Figure 13b). During the first 24 hours, while the shape of the initial square evolved into an elongated form, the size of the cluster, measured by $\sigma_X\sigma_Y$ (Figure 14), showed a relatively small increase. During the next 24 hours (Figure 13c), the size of the cluster increased dramatically (Figure 14). This coincided with further elongation of the cluster that exhibited an appearance of coastal topographic trapping, resulting in a break-up of the cluster (Figure 13c). Further spreading of the cluster was due to continuing elongation of the cluster combined with coastal topographic trapping (Figure 13d). Even after nine days, some particles still remained in the vicinity of the initial release point due to coastal topographic trapping (Figure 13e). After the first three days, the size of the cluster underwent rather regular oscillations with time (Figure 14). This was due to coastal topographic trapping of the particles modulated by tides. The rate of dispersion, as measured by the horizontal diffusivities (Eq. (3)), was 19.5 $m^2 s^{-1}$ for the first 6.8 days after which some of the particles were advected out of the model domain. Similarly, dispersion characteristics of tracer particles released at other parts of the bay were examined and the computed horizontal diffusivities are shown in Figure 15. The values of the diffusivity vary from 3.8 to 19.5 $m^2 s^{-1}$. Those values are smaller than the range of 50 - 200 $m^2 s^{-1}$ generally obtained by previous studies (e. g., Fischer et al., 1979; Prandle, 1984; Young et al., 1982; Zimmerman, 1986). This discrepancy appears to be due to the question of spatial-scale dependence of the horizontal diffusivity (e. g., Richardson, 1926; Okubo, 1971). In his tracer particle tracking experiment using a similar numerical model, Ridderinkhof (1990) found that a large dispersion coefficient is obtained if a larger volume is used to compute the dispersion coefficient. This is due to the fact that a greater part of the particle spreading is attributed to dispersion instead of advection if a larger water mass is used to make a distinction between the advective and dispersive component (Richardson, 1926; Ridderinkhof, 1990). In those previous studies, a relatively large grid size was used with the parameterization of

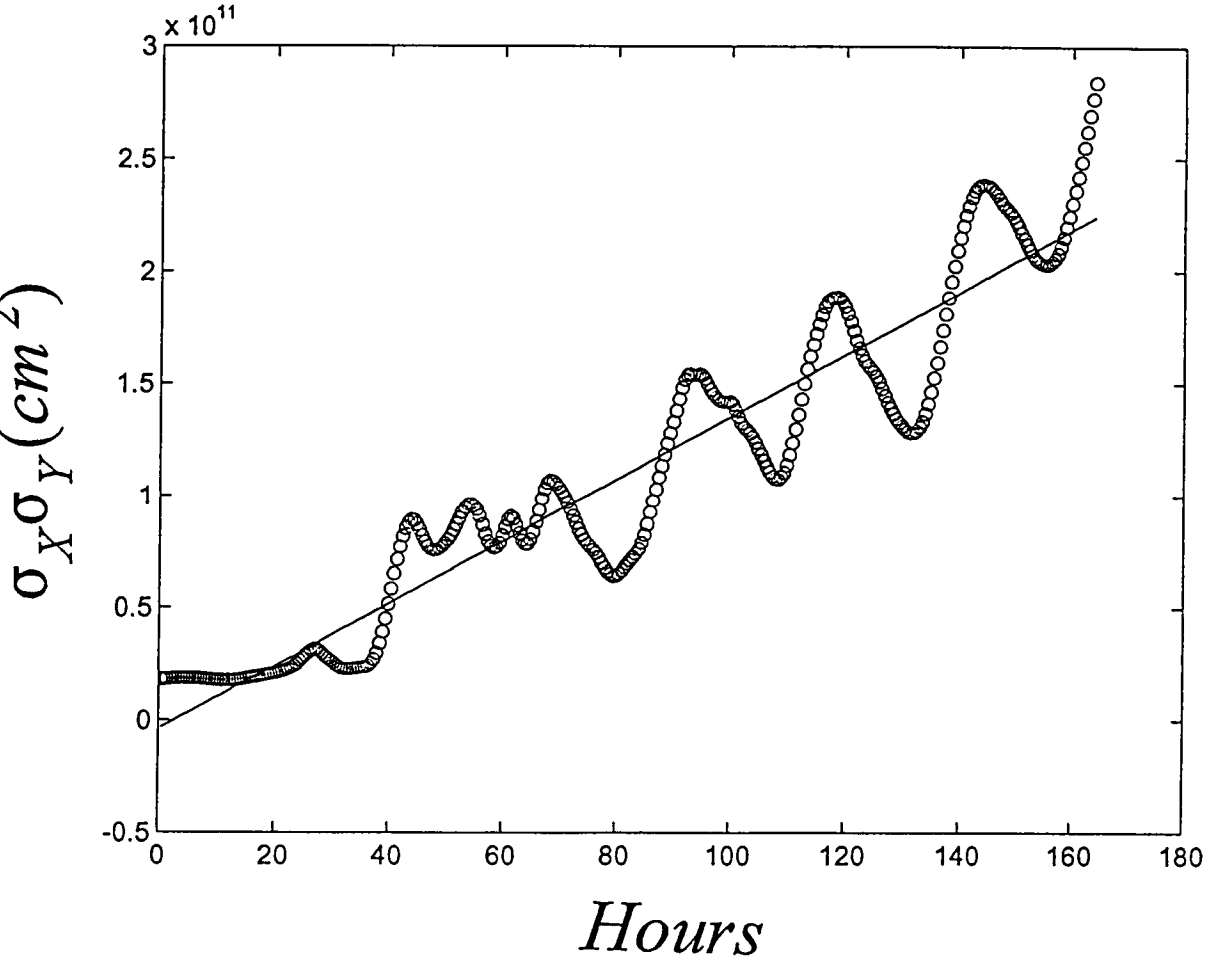

Figure 14. Variance (open circle), $\sigma_X\sigma_Y$, versus time for the particle cluster shown in Figure 13. Solid line is a least square fit.

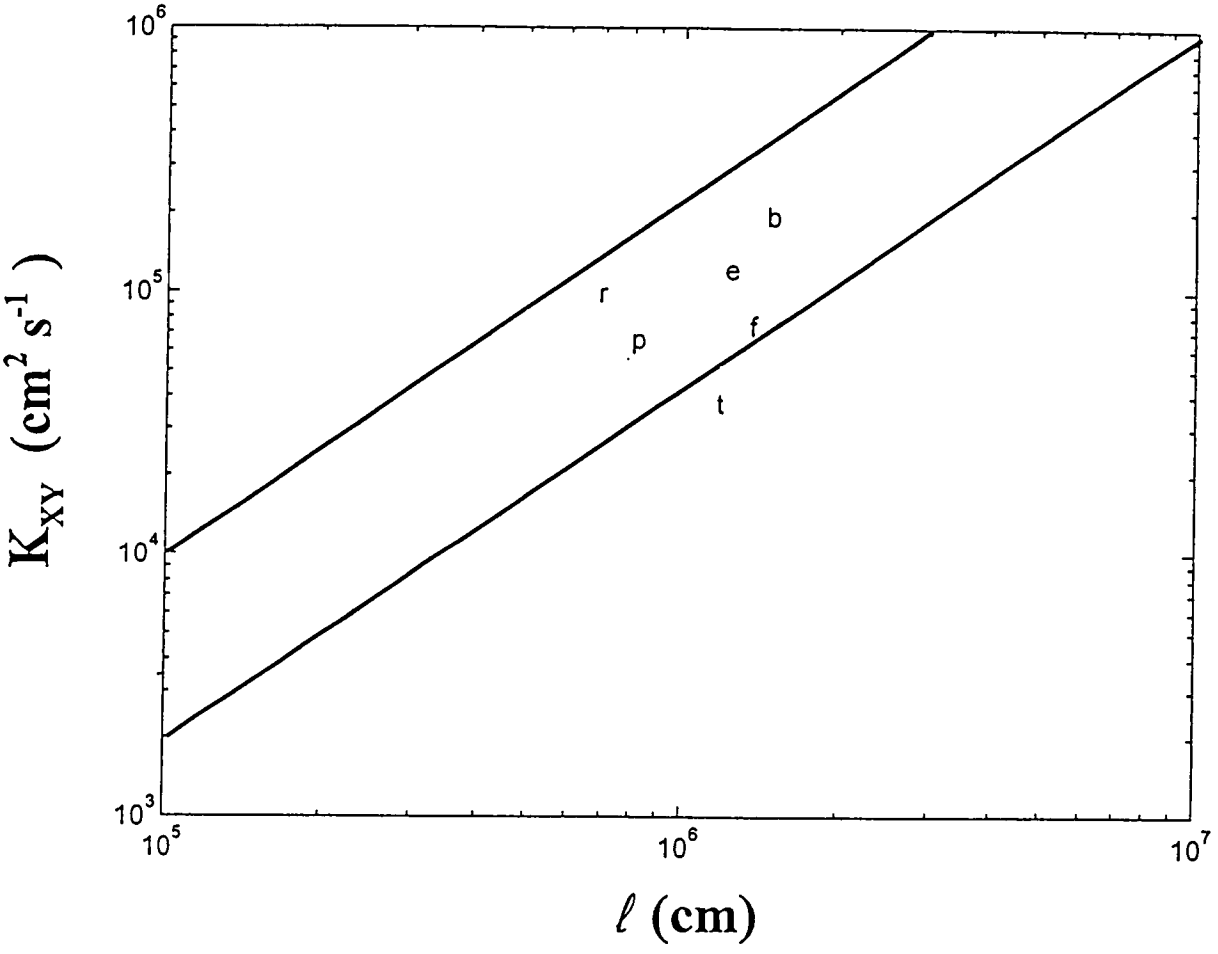

Figure 15. Horizontal diffusivities (cm^2 s^{-1}) of 100 particles released at various locations (b: Lake Barre; e: Terrebonne; f: Lake Felicity; p: Lake Pelto; r: Lake Raccourci; t: Timbalier) versus scale of diffusion, $l = 3\sqrt{2\sigma_X\sigma_Y}$ (Okubo, 1971). Range of Okubo's data (1974) is bounded by the two solid lines, $K_{XY} = 0.01\left(\frac{l^2}{9}\right)^{2/3}$ and $K_{XY} = 0.002\left(\frac{l^2}{9}\right)^{2/3}$ (Fischer et al., 1979).

the horizontal dispersion coefficient chosen such that the model salinity agrees with observations. Hence, the relatively small grid resolution used in this model study accounts for the difference. It should be noted here that those previous studies, using fine-resolution models with similar model grid size (e. g., Awaji, 1982; Ridderinkhof, 1990; Kapolnai et al., 1996), obtained values of the dispersion coefficient comparable to those found in this study, i. e., 1~10 $m^2 s^{-1}$ in the central parts of bays and 10~100 $m^2 s^{-1}$ in the vicinity of tidal passes. However, some (Awaji, 1982; Ridderinkhof, 1990) of those studies obtained dispersion coefficients of well over 100 $m^2 s^{-1}$ in the vicinity of a tidal pass (reaching values of 700~800 $m^2 s^{-1}$) with much stronger tidal currents. Those observations suggest that the magnitude of horizontal diffusivity depends not only on the length scale of the cluster but also on the surrounding flow regime characteristics (e. g., Geyer and Signell, 1992).

In comparison to the diffusion diagram compiled by Okubo (1974) based on dye patch diffusion and float dispersion, the values obtained here are comparable to Okubo's data (Figure 15). It is interesting to note that the larger values appear to be due to coastal topographic trapping. An example is illustrated in Figures 13 and 14. The particle cluster deployed in Lake Barre, initially exhibits a slow rate of spreading (Figure 14) until part of the cluster begins to be trapped by the coastal topography (Figure 13c). Thereafter, the rate of spreading increases significantly (Figure 14). Enhancement of horizontal dispersion by coastal topographic trapping is due to the presence of critical points in the flow field near a coastal boundary where a small difference in the particle position leads to a large difference in the subsequent trajectory. Those observations suggest that particle dispersion involving coastal topographic trapping appears to give rise to larger horizontal diffusivities. An analytical model to explain the enhancement of dispersion in estuaries due to the entrapment by shoreline irregularities was first proposed by Okubo (1973). Signell and Geyer (1990) investigated the influence of a headland on horizontal dispersion using a depth-integrated numerical model. They found that the intense shear zone associated with the flow separation at the tip of the headland is responsible for the explosive dispersion. Similar critical points in the flow field could be found near an island, and interaction of a oscillating tidal flow around islands could also lead to the enhancement of particle dispersion, i. e., "island trapping." Recently, Sanderson et al. (1995) demonstrated that the particle dispersion away from island obstacles is an order of magnitude less than that associated with an oscillating flow around islands. An example of the "island trapping" effect, can be found in Figure 13e (see also the following section). These observations suggest that coastal topographic trapping, that includes not only trapping by shoreline irregularities, such as headlands and inlets, but also trapping by islands could significantly enhance particle dispersion.

2.8 Mixing and Stirring of "Bay Water" with "Open Gulf Water"

Tracer particle techniques can be used to examine detailed mixing processes between "bay water" and "open Gulf water." Tracer particles can be deployed in such a way as to mark the boundary between two adjacent water bodies, and subsequent tracking of the tracer particles could be used to mark the time evolution of the boundary. For this experiment, initially 9800 tracer particles were deployed at uniform intervals along a straight line across the major pass into the bay system between Isles Dernieres and Timbalier Island, encompassing Wine Island Pass and

Cat Island Pass (Figure 16a). A line formed by those tracer particles could be considered as the boundary between "bay water" and "open Gulf water" at the time of the deployment. The tracer particles were released at Hour 0 05/02/90, and the particles were tracked over the next nine simulation days. Figures 16b through 16g show successive tracer particle locations after 1, 2, 3, 4, 5 and 6 days. One day after the time of release, the line of tracer particles has undergone stretching by the temporally and spatially varying velocity field (Figure 16b). The right half of the line has been stretched rather smoothly while the left half of the line displays more complex stretched and folded structures. This might indicate that the flow field in the vicinity of the main pass contains more complex flow characteristics on the left side of the pass. The entire line has been slightly displaced toward the interior of the bay, an indication of a net inflow during the first 24 hours. Two days after the release, the line has undergone further stretching with the left side of the line developing more complex stretched and folded structures (Figure 16c). A short segment of the line at the left side has completely broken off from the rest of the line, and further stretching and folding of this short segment have taken place. At this time, the middle segment of the line protrudes slightly out of the bay with both ends of the line exhibiting further intrusion into the bay, i. e., outflow of "bay water" taking place at the central portion of the pass with inflow of "open Gulf water" sandwiching this outflow tongue. After three days, stretching and folding continue with more segments broken up (Figure 16d). The overall outflow and inflow through the main pass remain similar to those seen before with the outflow tongue of "bay water" spreading laterally just outside the pass. This pattern continues after four days (Figure 16e). After five days, there is some indication of general westward flow developing in response to the strengthening easterly wind (Figure 16f). This westward flow continues through day 6 (Figure 16g). After six days, the original tracer particle line has undergone significant stretching, folding and break up.

Figure 17a shows the mean separation distance of the tracer particles as a function of time over the six day period. It is noteworthy in Figure 17a that during the first four days separation distance increases almost linearly. Then, it enters a period of rapid increase as the line of particles stretches. The transition to this rapid stretching coincides with a break-up of a major segment of the line caused by a flow separation at the eastern edge of Isles Dernieres (Figure 16e), an example of "coastal topographic trapping." This suggests that the time and space variable flow around the tip of an island can cause some particles to become greatly separated whereas others travel as a group and remain close neighbors for an extended period (Sanderson et al., 1995). Thereafter, the mean separation distance of particles increases quite rapidly, reminiscent of exponential growth, a characteristic of chaotic behavior (Ottino, 1989). Moreover, the computed mean separation distance during the later stages of the simulation period, should be an underestimate, because as more tracer particles exit the model domain (Figure 17b), they become excluded from the computation. These observations suggest that coastal topographic trapping gives rise to significant stretching and folding, a sign of a "chaotic" regime.

It has been suggested that dispersion is strongly dependent on the initial tidal phase when particles are released (e. g., Ridderinkhof, 1990). In order to examine the dependence of stretching of the boundary between the two water bodies on the time of the release in the tidal cycle, three additional experiments were carried out with the time of the release lagged by 6, 12

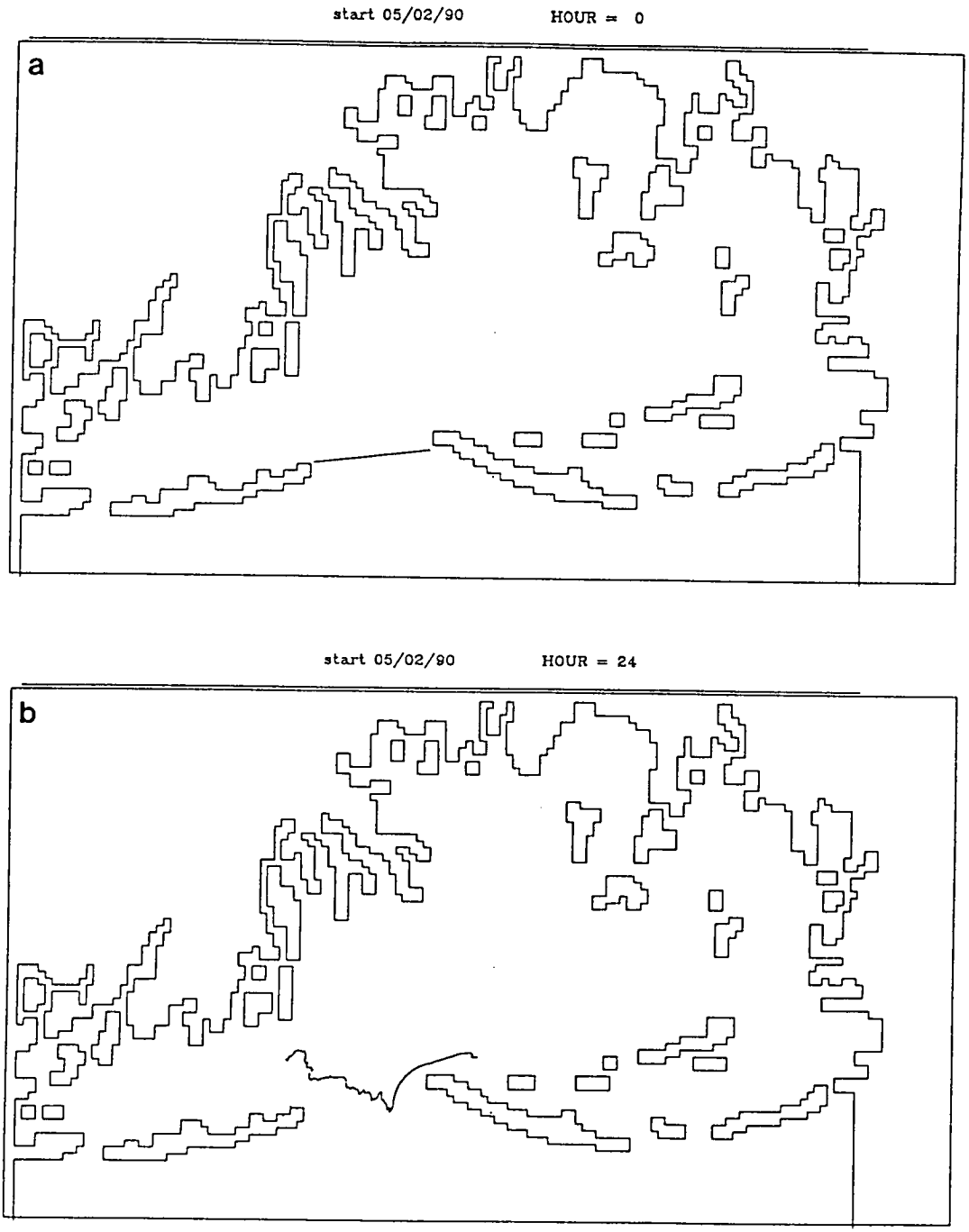

Figure 16. Distribution of tracer particles simulated for the period 05/02/90-05/25/90. A total of 9800 particles were released along a straight line across Wine Island and Cat Island Passes. a) At time of release. b) After 24 hours.

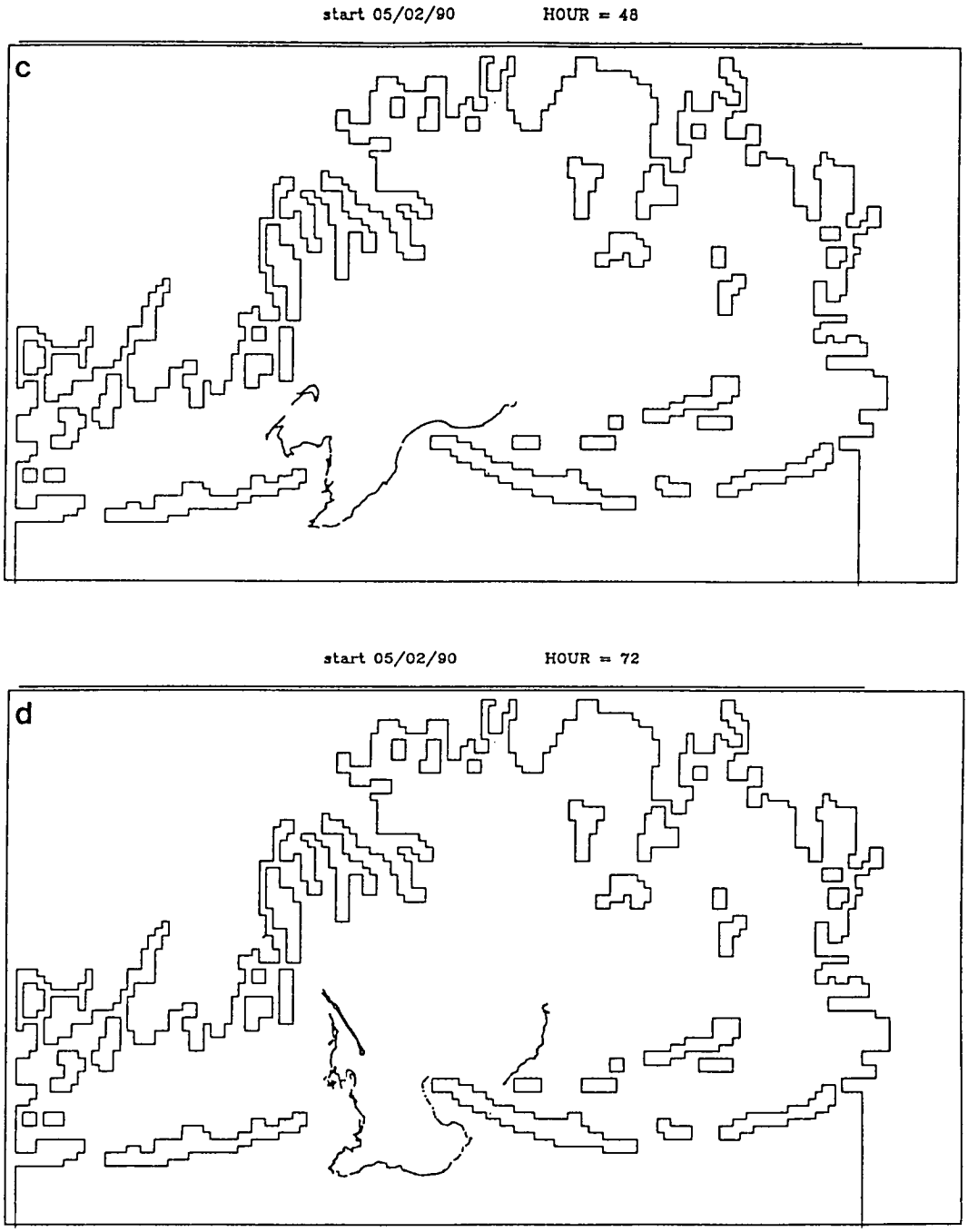

Figure 16. Distribution of tracer particles simulated for the period 05/02/90-05/25/90. A total of 9800 particles were released along a straight line across Wine Island and Cat Island Passes. c) After 48 hours. d) After 72 hours.

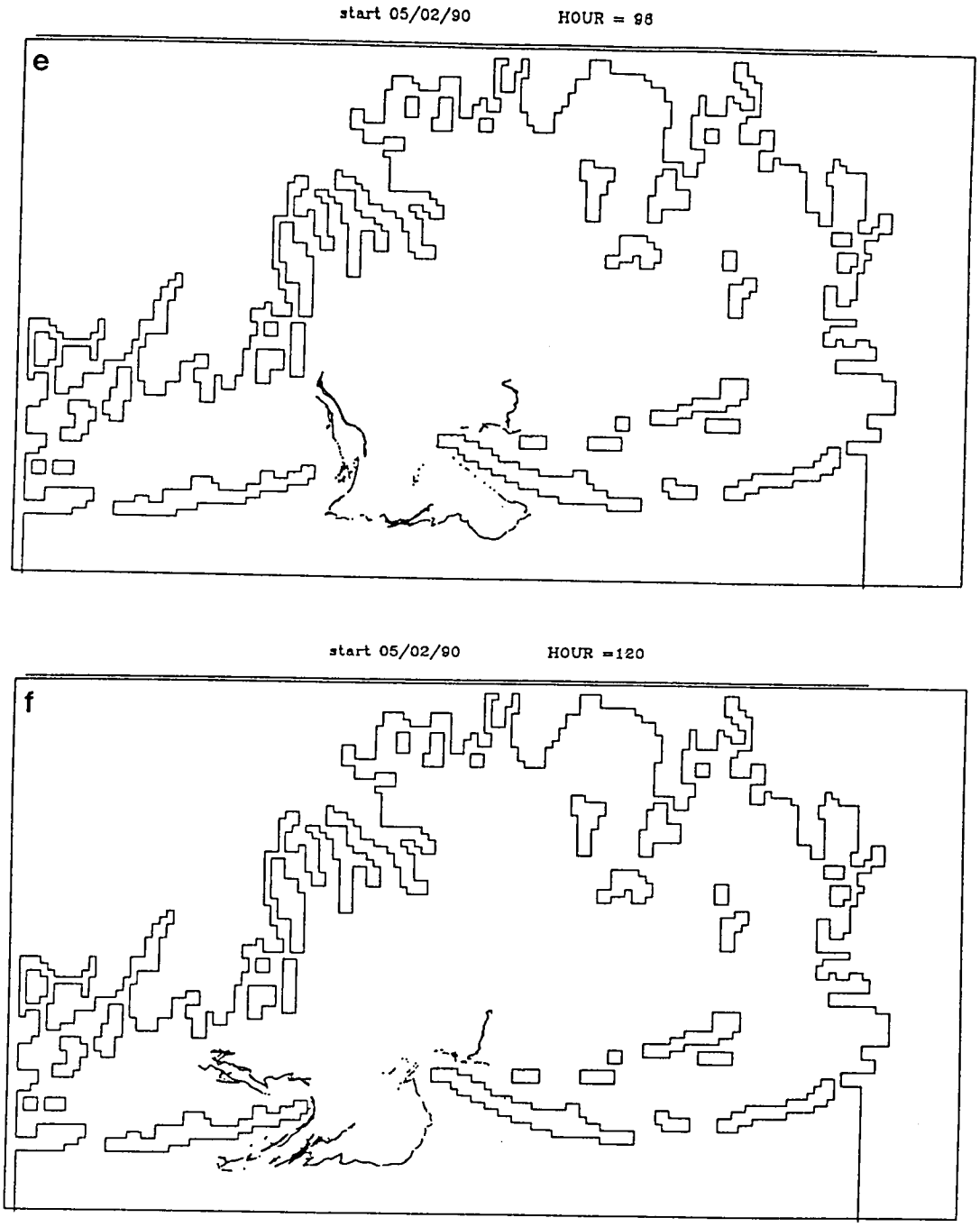

Figure 16. Distribution of tracer particles simulated for the period 05/02/90-05/25/90. A total of 9800 particles were released along a straight line across Wine Island and Cat Island Passes. e) After 96 hours. f) After 120 hours.

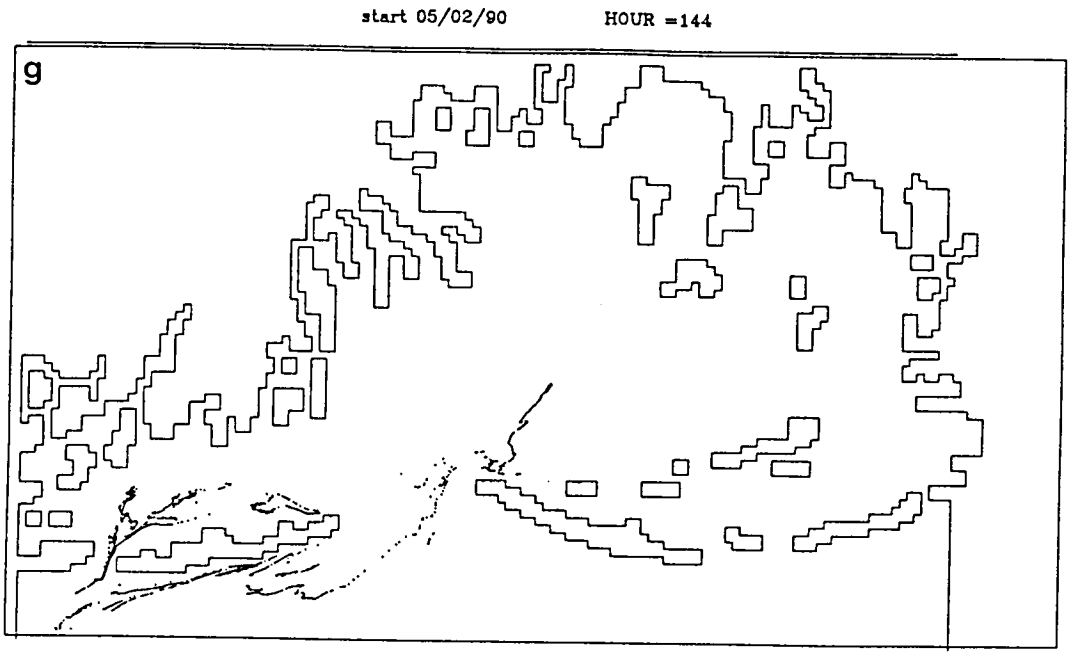

Figure 16. Distribution of tracer particles simulated for the period 05/02/90-05/25/90. A total of 9800 particles were released along a straight line across Wine Island and Cat Island Passes. g) After 144 hours.

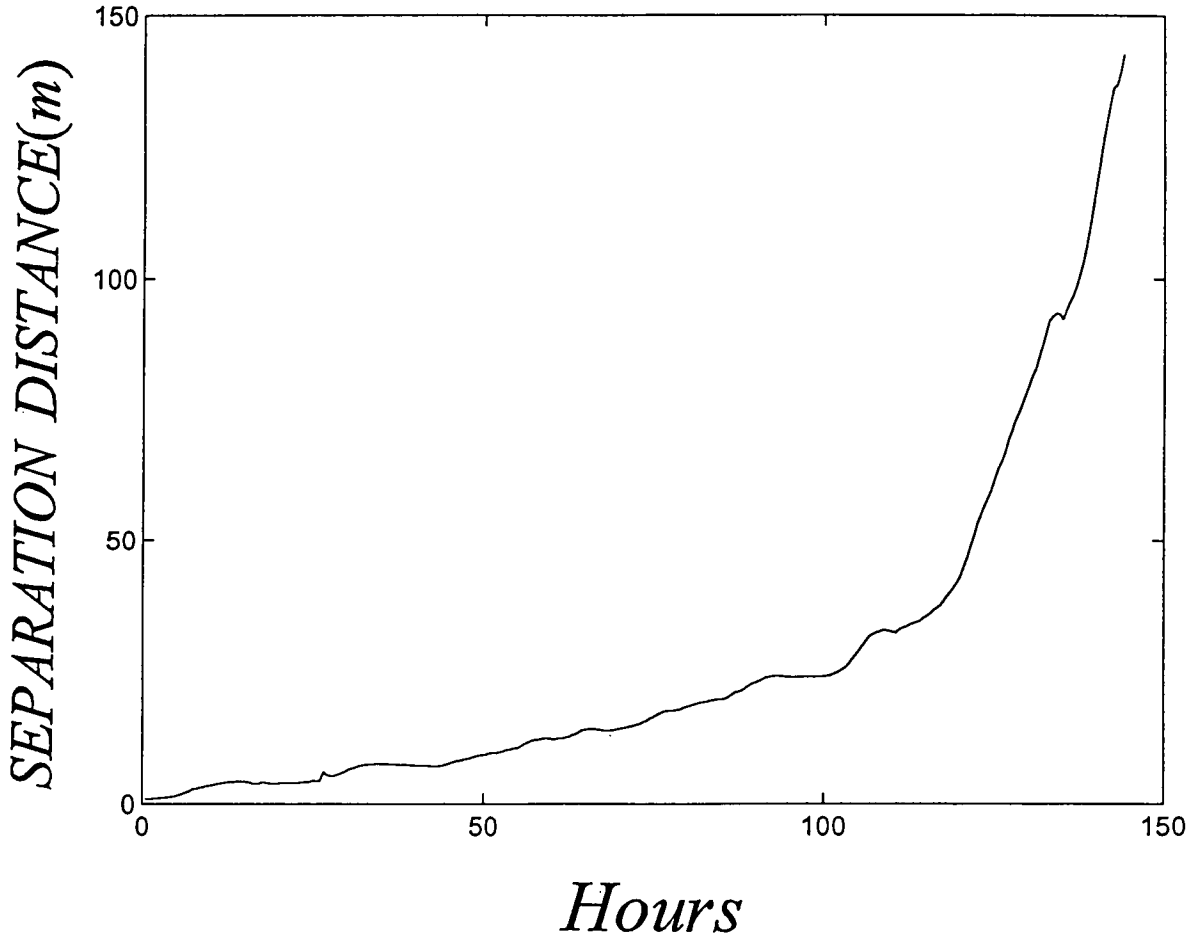

Figure 17a. Mean separation distance between neighboring particles along the line formed by 9800 particles as a function of time.

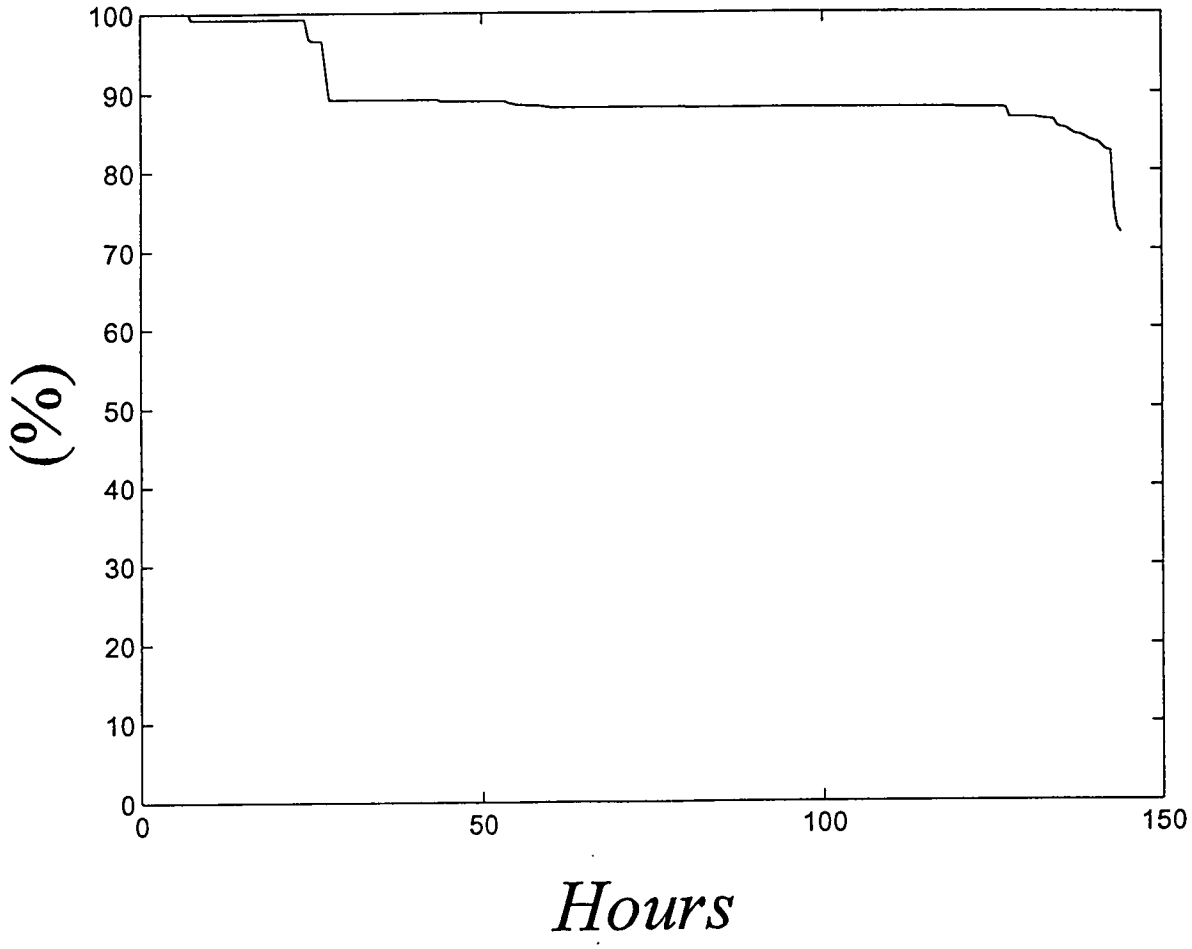

Figure 17b. Fraction of the particles remaining within the model domain as a function of time.

and 18 hours, respectively (Figures 18a through 18c). It is clear in Figure 18a that the initial stretching of the boundary is strongly dependent on the initial tidal phase. However, approximately 6 days after the release, tracers in all of the four experiments appear to undergo a period of rapid stretching, and the resulting rates of stretching in all the experiments converge to similar values (Figure 18b). This suggests that the dependence on the initial tidal phase is limited in duration, lasting for several days for the case under study, beyond which the memory associated with the initial time of release relative to the tidal cycle appears to be lost. It appears that as long as coastal topography does not become the most dominant agent for increasing the separation of neighboring tracer particles, the resulting stretching strongly depends on the time of release in the tidal cycle, however, once "coastal topographic trapping" becomes dominant, the dependence on the initial tidal phase is diminished.

It should be noted that the time-dependent evolution of the interface between the two water masses examined here is what Eckart (1948) refers to as "stirring" in contrast to "mixing." In studying the phenomena accompanying the mixture of two incompressible fluids, Eckart noted that the "stirring" stage whereby the two fluid masses are being stretched and folded by advection with a rapid increase in the extent of the interfacial regions having high concentration gradients, precedes the "mixing" stage whereby molecular diffusion smoothes out the gradients with the liquid becoming homogenous. Following Eckart's terminology, the time evolution of the boundary between "bay water" and "open Gulf water" in this study should be referred to as "stirring." Presumably, the sharp gradients arising from "stirring" would be smoothed out by diffusion processes during the final stages of mixing of the two water masses. The observed rapid growth of the interface appears to suggest "chaotic advection" (Aref, 1984), "chaotic dispersion" (Brown and Smith, 1991), and "chaotic stirring" (Ridderinkhof and Zimmerman, 1992). The hallmark of fluid motion in which particle trajectories are chaotic is that material lines of fluid grow exponentially in time due to extreme sensitivity to initial conditions (Ottino, 1989). When particle trajectories in a fluid are chaotic, the fluid is stirred efficiently, which, in turn, enhances diffusive mixing within the fluid. Regular (nonchaotic) particle trajectories, on the other hand, are not associated with efficient stirring (Brown and Smith, 1990). Recently, chaotic advection and stirring have been recognized to play a significant role in transport and mixing processes in estuaries (e. g., Ridderinkhof, 1990; Ridderinkhof and Zimmerman, 1992; Geyer and Signell, 1992), coastal seas (e. g., Ridderinkhof and Loder, 1994; Sanderson et al., 1995), intergyre exchange between a subpolar gyre and a subtropical gyre, (Liu and Yang, 1994), and an equatorial ocean (Li et al., 1996). The observed chaotic dispersion due to coastal topographic trapping is reminiscent of mixing and dispersion in a furrowed channel studied by Sobey (1985). It was observed that if the channel is furrowed so that unsteady separation occurred, then dispersion of particles is greatly increased (Sobey, 1985). Other previous applications of a similar model can be found, for example, in civil engineering for natural streams with pockets (e. g., Thackston and Schnelle, 1970).

2.9 Summary and Conclusions

Transport and mixing processes in a broad and shallow estuary in Louisiana, Terrebonne/Timbalier Basin, have been examined using a depth-integrated two-dimensional

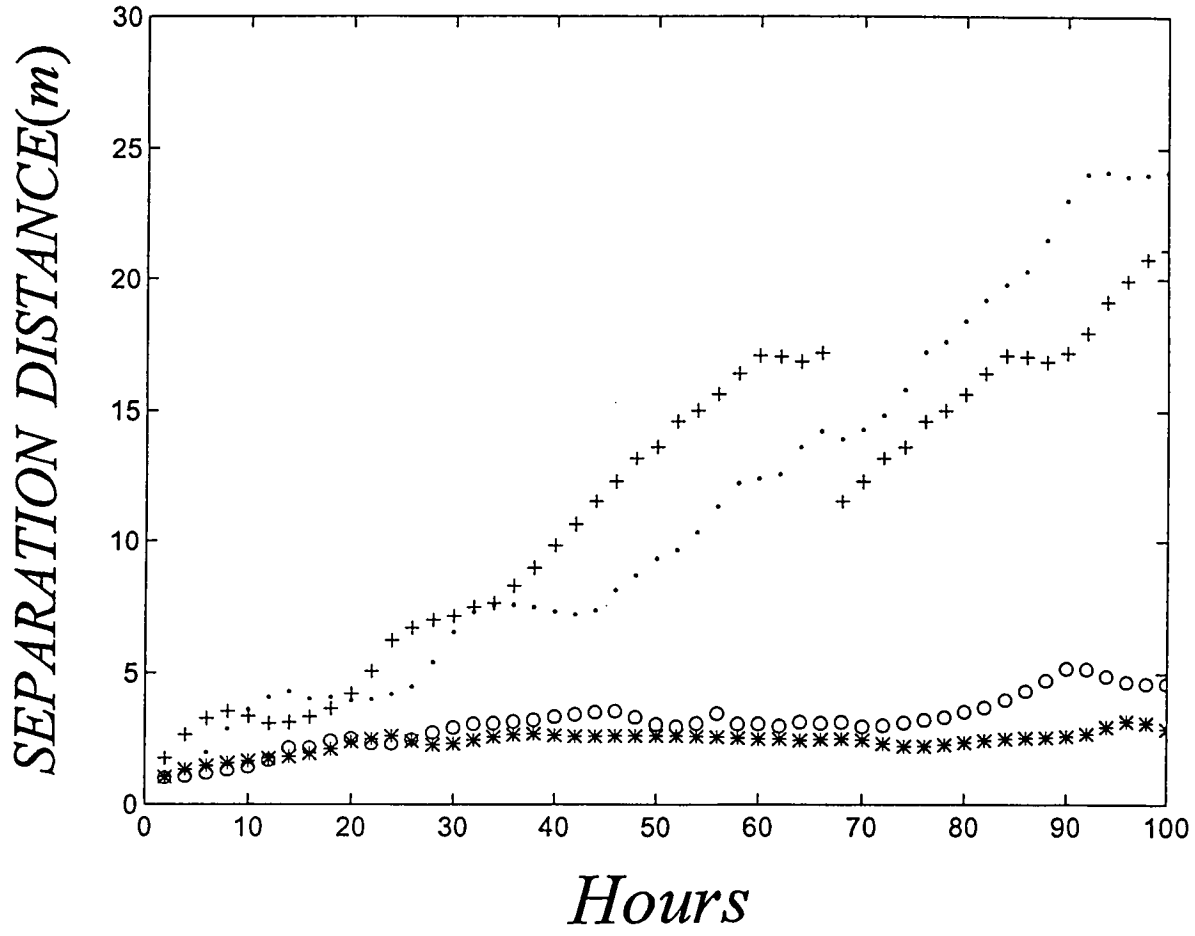

Figure 18a. Mean separation distance between neighboring particles along the line formed by 9800 particles as a function of time for the first 100 hours. Points indicate the case shown in Figure 17. + , open circle, and * indicate three cases with the initial release time lagged by 6, 12, and 18 hours, respectively relative to the first case shown in Figure 17.

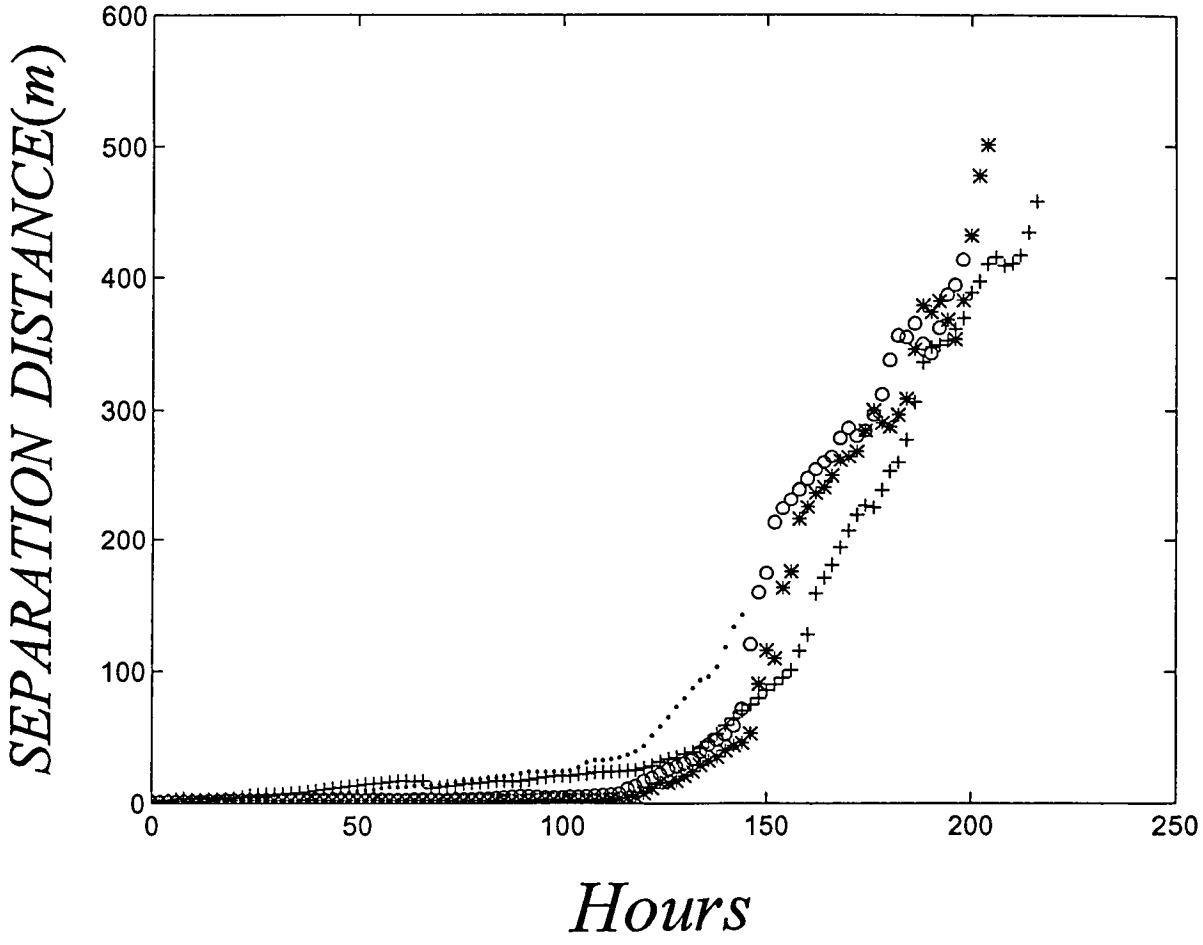

Figure 18b. Same as (a) expect shown for the entire period of the experiments.

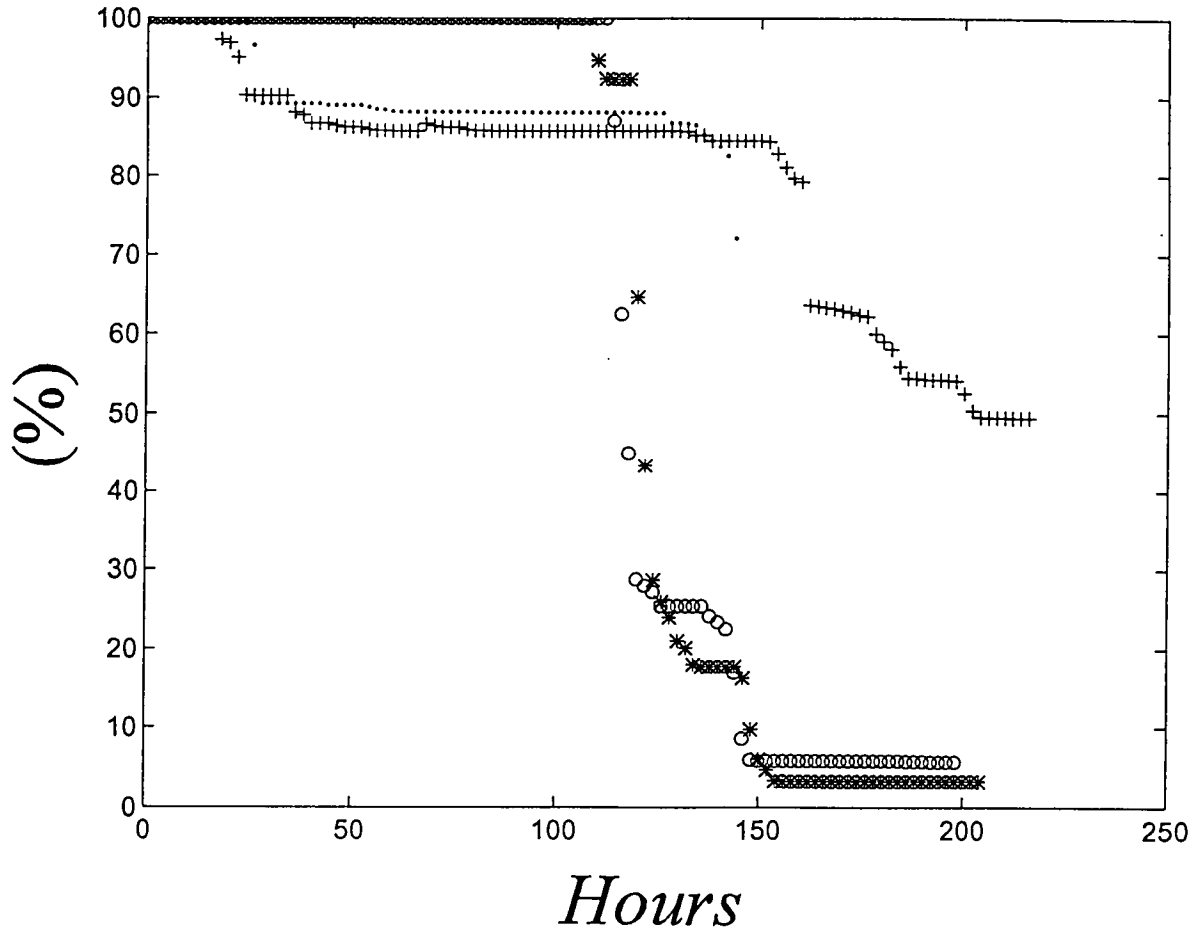

Figure 18c. Fraction of the particles remaining within the model domain as a function of time. Symbols are same as for (a) and (b).

numerical model. The model was calibrated against the current meter records previously obtained. The calibrated model yielded correlation coefficients between simulated and observed current components of 0.89~0.95. It appears that the bottom friction in the bay is relatively large with a Manning's coefficient of 0.07 producing the best results. The large bottom friction appears to be due to a combined effect of currents and the surface wave field which is not explicitly accounted for in the numerical model. Despite its small tidal range, the model, forced by the observed wind and sea-level heights, points to the significant impact of tidal forcing in dominating circulation in the bay. Even during equatorial tides, tidal currents on the order of 20 cm s^{-1} could develop in a broad area of the bay while in tidal passes currents could reach 50~60 cm s^{-1}. During tropic tides, strengths of the currents in the bay could easily be double those during equatorial tides. Local wind forcing is important in controlling the general flow direction inside the bay. In particular, the impact of wind forcing becomes comparatively more important during equatorial tides. In terms of relative volume transport, Wine Island Pass-Cat Island Pass dominates, accounting for nearly 60% of the total inflow into the bay, with two shallower passes (Whiskey Pass and Little Pass Timbalier) each accounting for 20% of the total.

A tracer particle tracking technique was used to examine transport and mixing characteristics inside the bay. Flushing time, estimated by the particle tracking technique, was 27 days. This appears to be in agreement with observations. Horizontal diffusivities computed using tracer particles range from 3.8 to 19.5 $m^2 s^{-1}$. Those values are comparable to the range of horizontal diffusion coefficients compiled by Okubo (1974) based on dye patch diffusion and float dispersion. The larger values appear to be due to coastal topographic trapping that gives rise to more "efficient" dispersion of particles. Enhancement of horizontal dispersion by coastal topographic trapping is due to the presence of critical points in the flow field near a coastal boundary where a small difference in the particle position leads to a large difference in the subsequent trajectory. Coastal topographic trapping gives rise to rapid stretching of the material lines, a sign of "chaotic stirring."

Mixing of "bay water" with "open Gulf water" is examined by tracking the time evolution of the boundary between the two water bodies marked by tracer particles. The time evolution of the boundary strongly depends on the initial tidal phase. However, this dependence lasts only until "coastal topographic trapping" becomes dominant in controlling the time evolution of the boundary. Eventually, the dominance of "coastal topographic trapping" results in more "chaotic dispersion."

Historically, Okubo (1973) first presented an analytical model to explain the enhancing effect of shoreline irregularities on horizontal dispersion in estuaries. More recently, the chaotic nature of mixing processes in estuaries has been recognized (Ridderinkhof, 1990; Ridderinkhof and Zimmerman, 1992; Geyer and Signell, 1992). Exceeding the ratio of the periodic particle excursion length to the horizontal length scale of spatial variations in the current field has been recognized to be important to the onset of chaotic stirring (Geyer and Signell, 1992; Ridderinkhof and Zimmerman, 1992; Ridderinkhof and Loder, 1994). The numerical model studies of Awaji (1982) and Signell and Geyer (1990) suggest that topographic trapping due to shoreline irregularities has a significant influence on horizontal dispersion where flow separation occurs.

Recently, Sanderson et al. (1995) noted that chaotic dispersion could result from oscillating flow around islands. This is due to the presence of critical points in the flow field near islands. The results of this study suggest that coastal topographic trapping, that includes not only trapping by shoreline irregularities but also trapping by islands, could significantly enhance particle dispersion. Mixing of water masses, based on particle tracking, is found to consist of continuous stretching, folding and break-up of material lines due to interaction of wind-driven and tidal currents with bottom and coastal topography. These observations point to the need to resolve small-scale shear flow patterns, in both space and time, and detailed bottom and coastal topography in order to understand transport, stirring and mixing processes in the broad, shallow estuaries typical of the northern Gulf of Mexico. It is interesting to note that many of the estuaries in the northern Gulf of Mexico have rather complex shoreline irregularities and numerous islands, and the results of this study suggest that the interaction of variable currents with complex topographic features is likely to lead to chaotic and efficient dispersion in those estuaries.

CHAPTER 3

BARATARIA BASIN STUDY

3.1 Background

Barataria Basin is situated immediately west of the Mississippi Delta. It is only 1 m to 2.7 m deep. Unlike Terrebonne/Timbalier Bay to the west, connectivity of Barataria Bay System to the surrounding vast network of tidal channels and lakes is extensive (Figure 19). Barataria Bay, Lake Salvador, Lac des Allemands, and connecting water bodies form the major links for water exchange between the Gulf and the inner basin. Fresh water and sediment input to the Barataria Basin is limited by flood protection levees along the Mississippi River and the closure of Bayou Lafourche at Donaldsonville. The total fresh water run-off is largely due to rainfall and agricultural run-off over the basin (Marmer, 1954; Kjerfve, 1972; and Van Sickle et al., 1976).

The dominant water exchange route between the upper and lower basin is through Little Lake and Bayou Perot, and Lake Salvador. Secondary exchange is through Mud Lake, Barataria Bay Waterway. A chain of barrier islands and barrier beaches separates the basin from the Gulf of Mexico. The tidal currents off the Barataria Bay-Caminada Bay complex are characterized by clockwise rotation (Wiseman et al., 1975). Currents at Barataria Pass at maximum flood were cited as being 1.26 knots and at maximum ebb as 0.82 knot. Ebb currents dominated in duration (Marmer, 1948).

The model bathymetry was taken from Nautical Charts (Scale 1:80,000) (Figure 19). Some difficulties were encountered in estimating the depths of upper reaches of the basin where reliable depth data were scarce. The same model grid spacing, time step, and horizontal eddy viscosity as in the Terrebonne/Timbalier Basin Model were used. Some narrow waterways have widths smaller than the model grid spacing of 463 m. It should be noted that the use of an uniform grid spacing over the entire model domain results in over-representation of the cross-sectional area of those narrow waterways. However, this maintains faithful representation of the channel depths, resulting in a correct representation of the tidal propagation characteristics throughout the basin.

In comparison to Terrebonne/Timbalier Basin, more extensive measurements of tides and currents are available in the Barataria Basin that can be used for model calibration (Figure 20). Historical water level and current data in 1988 were collected by US Army Corps of Engineers (USECOE), New Orleans District. Water level data were recorded using Endeco Type 1029 water level recorders at sites St. 01, St. 02, St. 03, St. 11, and St. 16, and using Endeco Type 1152 density compensating water level recorders at sites St. 12, St. 18, and St. 20. Historical current data at three tributaries, C04, C07, and C08, were obtained by USACOE using Endeco 174 current meters.

For this study, wind data were available at both New Orleans International Airport and at Grand Isle. Due to the separation distance between those two sites, the two wind records are not

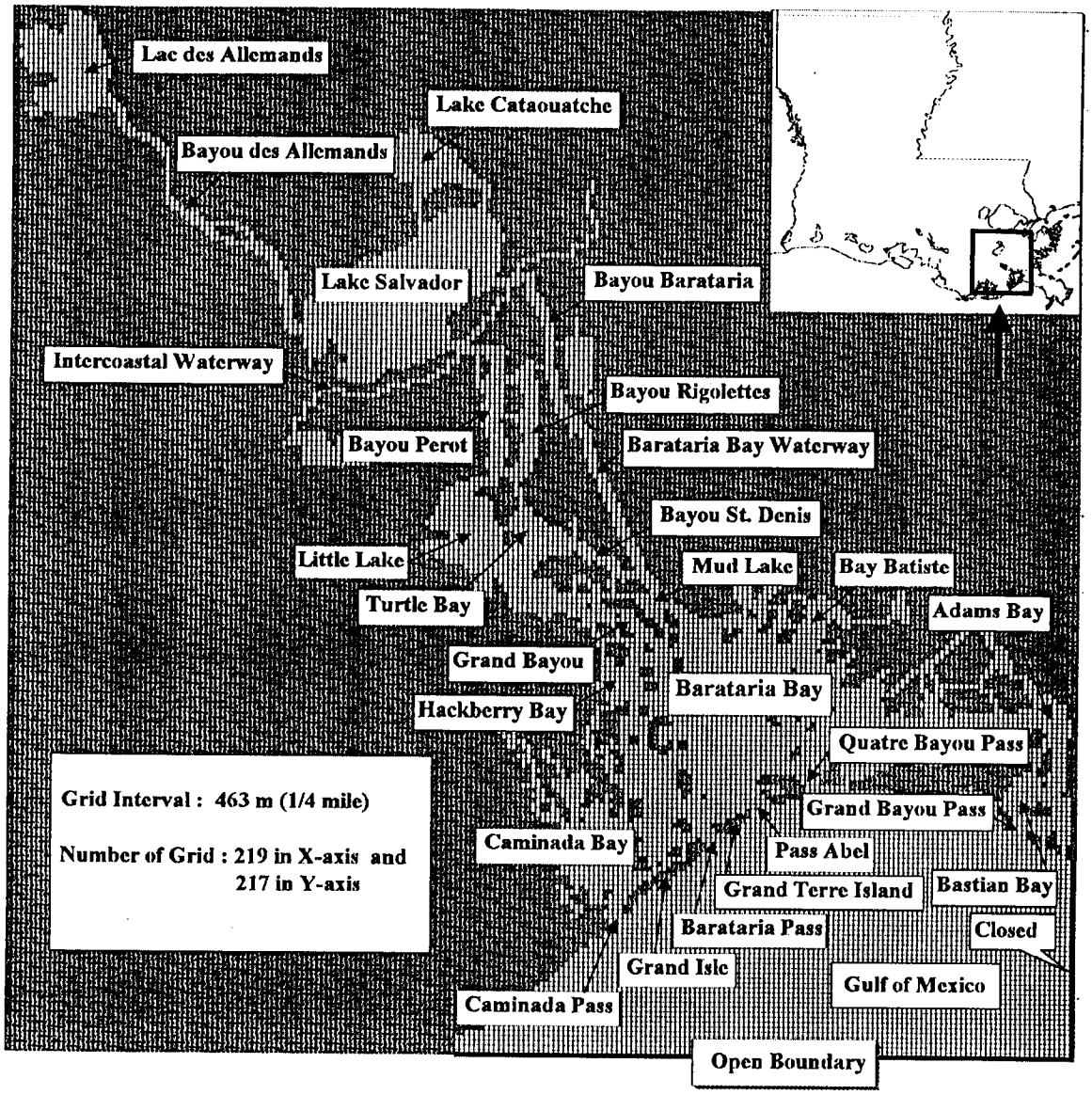

Figure 19. Location map of Barataria Basin and model geometry. The southern boundary is open.

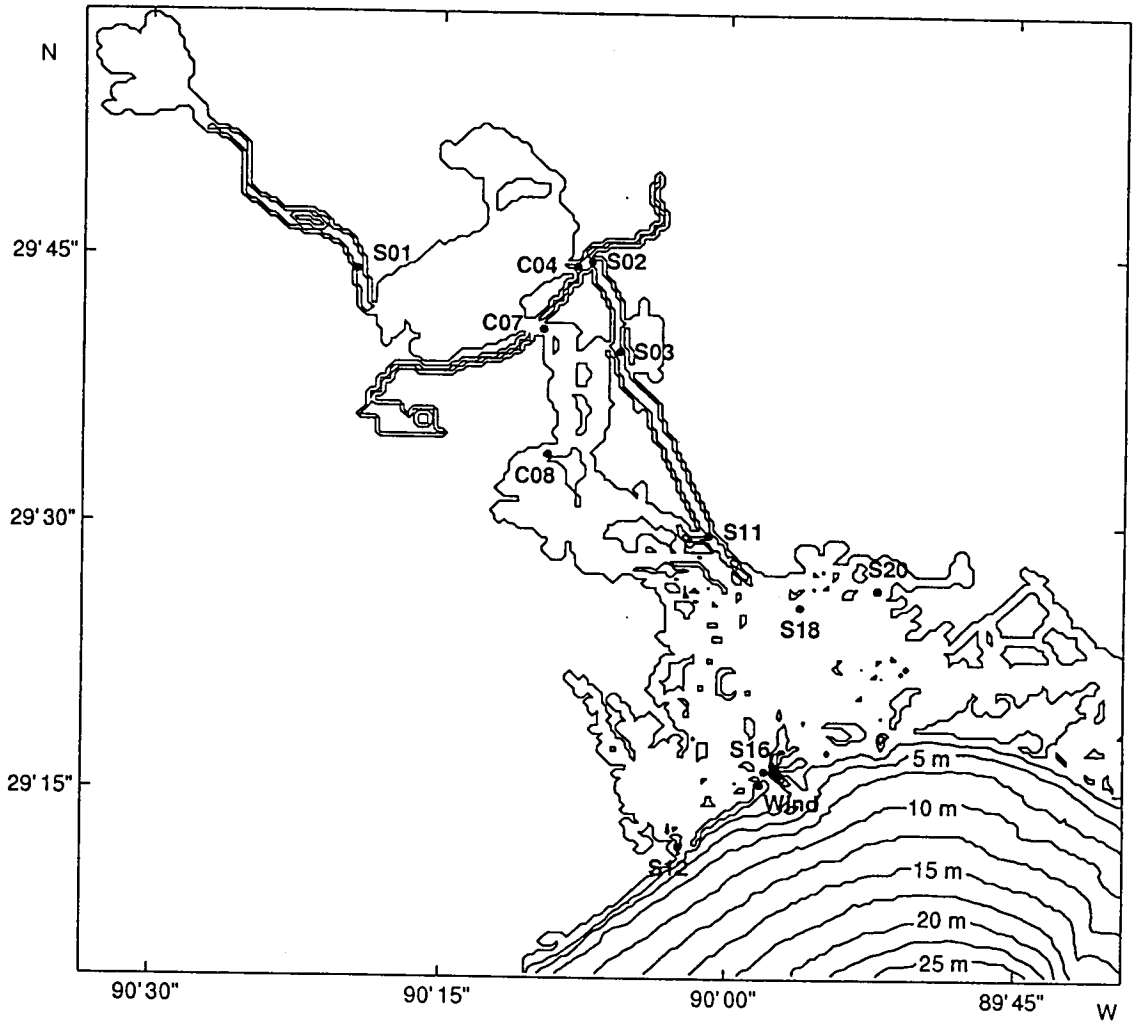

Figure 20. Locations of stations where data on sea level height (denoted by S), currents (denoted by C) and winds are available for model calibration. Bottom bathymetric contours are shown at every 2.5 m.

identical. Since the wind data measured at both sites were not from the standard reference heights, conversion to the standard 10-m reference height was done based on the logarithmic wind profile (e. g., Panofsky and Dutton, 1984). Initial calibration runs were made by forcing the model using both wind data sets, and the model simulated sea level at various sites was compared to the observed sea-level records. The use of the wind data from Grand Isle resulted in a better model-observation comparison everywhere except at St. 01, which is located furthest from Grand Isle and closest to New Orleans International Airport. It was decided to adopt the wind data from Grand Isle for the wind forcing.

3.2 Model Calibration

The model is forced by the incoming tides from the open Gulf and the wind forcing over the model domain. Due to the lack of sea level height measurements near the southern open boundary (Figure 19), the observed water level data from St. 12 was used to represent sea level height along the southern open boundary. After initial calibration runs, it was decided to use the sea level height measured at St. 12 with an amplification factor of 1.13 and a 2-hour phase lead as the open boundary conditions.

Since the model domain extends over a large area, it is conceivable that there exits significant spatial variation in the local wind forcing. However, due to the limited availability of local wind data, spatial uniformity was assumed for the local wind forcing over the entire model domain. The following empirical relationship, derived specifically for the Barataria Basin (Hsu, 1996, personal communication), was used to convert from wind speed to wind stress.

$$u_* = 0.055\, u_{10} - 0.025$$

The model was spun up from rest using the observed hourly wind and sea level height for the period 07/07/88-07/27/88. Due to the extensive upper reaches of Barataria Basin, spin up for Barataria Basin took much longer than for Terrebonne/Timbalier Basin. Figure 21 shows simulated and observed sea-level heights at Sts. 01 and 12. It takes approximately 10 days for the model to loose memory of the initial conditions, and 10 days appears to be a reasonable estimate for the spin-up time. This is much longer than the estimated travel time of the tidal signal to complete a round trip from the open boundary all the way up to the northern end of the model domain. Apparently, the tidal signal must complete several round trips throughout the model domain to reach statistical quasi-equilibrium with the forcing.

Extensive spatial coverage by the available sea level height records provided the necessary calibration data to identify an appropriate bottom friction parameter to be used in the model. The model calibration was done by adjusting the Manning's coefficient until the best model-observation comparison was achieved in terms of tidal propagation throughout the basin. A series of calibration runs was carried out by varying Manning's coefficient and comparing the observed and simulated sea level height at various stations. Specifically, amplitude and phase lag were estimated by computing lagged cross correlation (Tables 1 and 2). Additional calibration runs included cases with spatially varying Manning's coefficients (not shown here). An appropriate

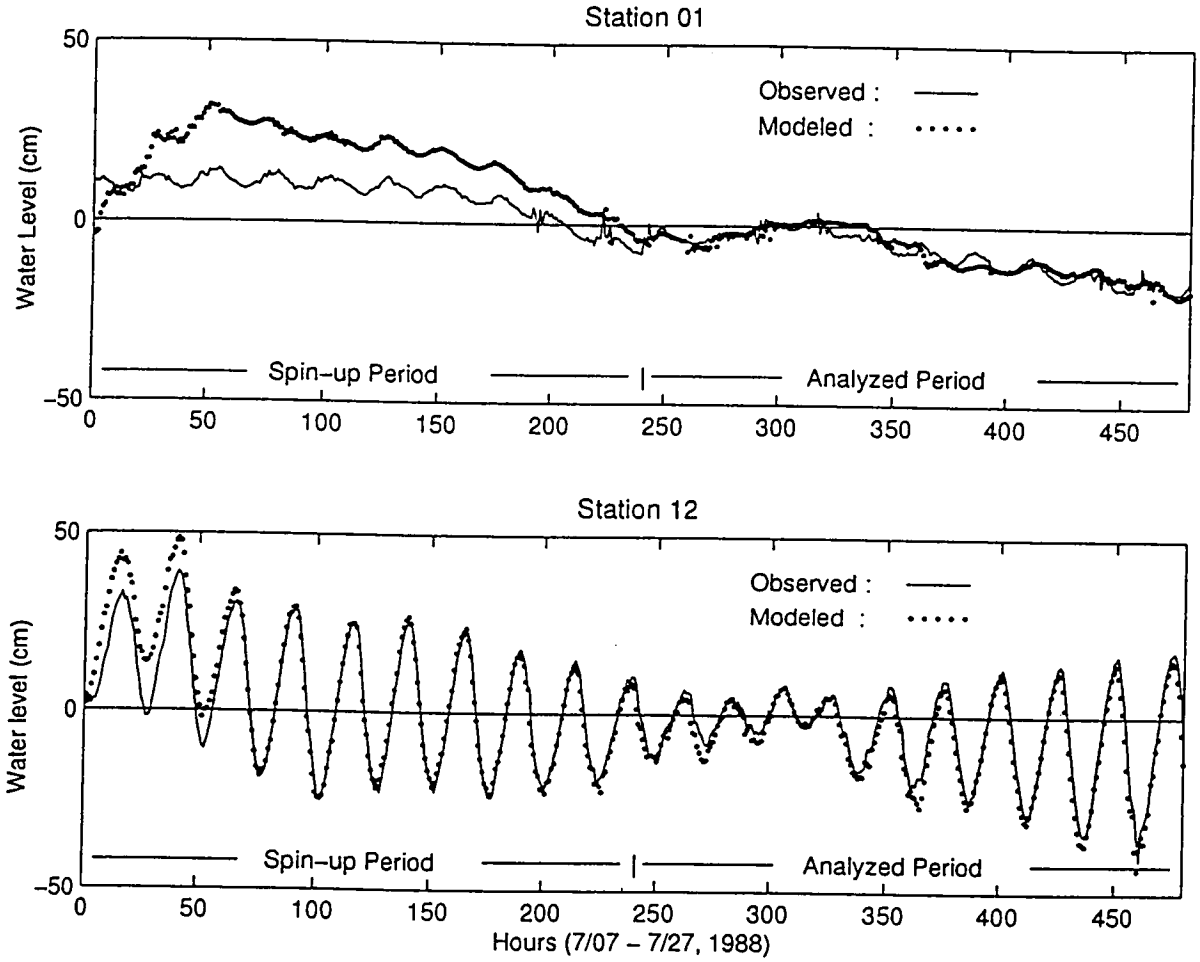

Figure 21. Simulated and observed sea level height at Sts. 01 and 12. Spin-up period is indicated during which the model initialization from rest appears to have died down. Analysis of model output is performed excluding the spin-up period.

Table 1

Observed and simulated phase lag (minutes) in sea level height relative to St. 16 for three different Manning's coefficients.

	Observed	n=0.03	n=0.04	n=0.05
ST01	725	750	765	795
ST02	595	645	655	670
ST03	415	425	440	460
ST11	165	175	190	210
ST16	0	0	0	0
ST18	85	90	105	120
ST20	90	95	115	130

Table 2

Ratio of amplitude between simulated and observed sea level heights for three different Manning's coefficients.

	n=0.03	n=0.04	n=0.05
ST01	0.998	0.992	0.983
ST02	0.878	0.871	0.860
ST03	1.032	1.008	0.992
ST11	1.048	1.011	0.996
ST12	0.999	0.998	0.997
ST16	0.924	0.921	0.921
ST18	1.070	0.999	0.994
ST20	1.000	0.962	0.931

Manning's coefficient should result in overall optimum match between the model and the observations in terms of amplitude and phase. Consequently, a Manning's coefficient of 0.04 was selected. It should be noted that there were some uncertainties in the exact location of some of the stations relative to the model grid, and a difference of just one model grid could result in phase differences of a few minutes. The model's ability to simulate the observed sea level height variations at eight stations is presented in Figures 22a through 22h. Although there are slight differences in observed and predicted phase at all sites, simulations are in general agreement with the observations. The phase differences between simulated and observed sea level could partly be attributable to the inaccuracies in model bathymetry, in open boundary specification, and in wind stress forcing. Unfortunately, only three current meter sites produced useful current measurements for model-observation comparison. Figures 23a through 23c present model-observation comparison for the three current meter sites located in the upper reaches of the basin. It is evident that the model tends to underestimate the current magnitude. This discrepancy appears to arise from the inaccuracies of the model grid representation of the upper reaches of the basin, primarily resulting from the inadequate bathymetric data and the inability of the coarse model grid spacing to represent many narrow channels. Another potential problem arises from the assumption adopted here regarding the representativeness of the measured currents to indicate the depth-averaged currents. It should also be remembered that the observations may contain a signal driven by runoff which is not present in the model.

3.3 Model Simulation

Once the model calibration was completed, the model output for the period 07/17/88-07/27/88 was analyzed. The wind data used to force the model and the simulated sea level height at St. 16 (at the mouth of Barataria Bay) for the period 07/17/88-07/27/88 are shown in Figures 24 and 25, respectively. The first half of the simulation period is characterized by moderate southerly wind while the second half is punctuated by several wind reversals associated with the passage of weak fronts. Tidal range varies from 10 cm to 60 cm at St. 16 located near the mouth of Barataria Bay, and from 0.34 cm to 2.56 cm at Lac des Allemands during the simulation period. It is evident that the tides are significantly damped as they propagate upstream through the basin.

In order to isolate the response of Barataria Basin to tidal forcing only, the model was forced by two different tidal ranges without wind forcing, one with a tidal range of 10 cm, representing equatorial tides, and the other with a tidal range of 60 cm, representing tropic tides. The model was run for 20 days, and the model sea level height field was analyzed for the second 10-day period, i. e., the first 10-day period was considered as spin-up. The phase of tidal propagation throughout the basin simulated in the model is shown in Figure 26. Time lags between the mouth of Barataria Bay, specifically Station 16, and the interior of the bay were calculated by computing cross-correlations. The time lag with respect to the tidal passes is less than 3 hours in Barataria Bay and Caminada Bay, between 5 and 6 hours in Little Lake, between 6 and 7 hours in Bayou Perot, and between 11 and 12 hours in Lake Salvador. Beyond Lake Salvador it gradually increases until a maximum of 15 hours is reached in the middle of the Bayou des Allemands, then it decreases. The noted complex spatial pattern of time lags beyond Lake

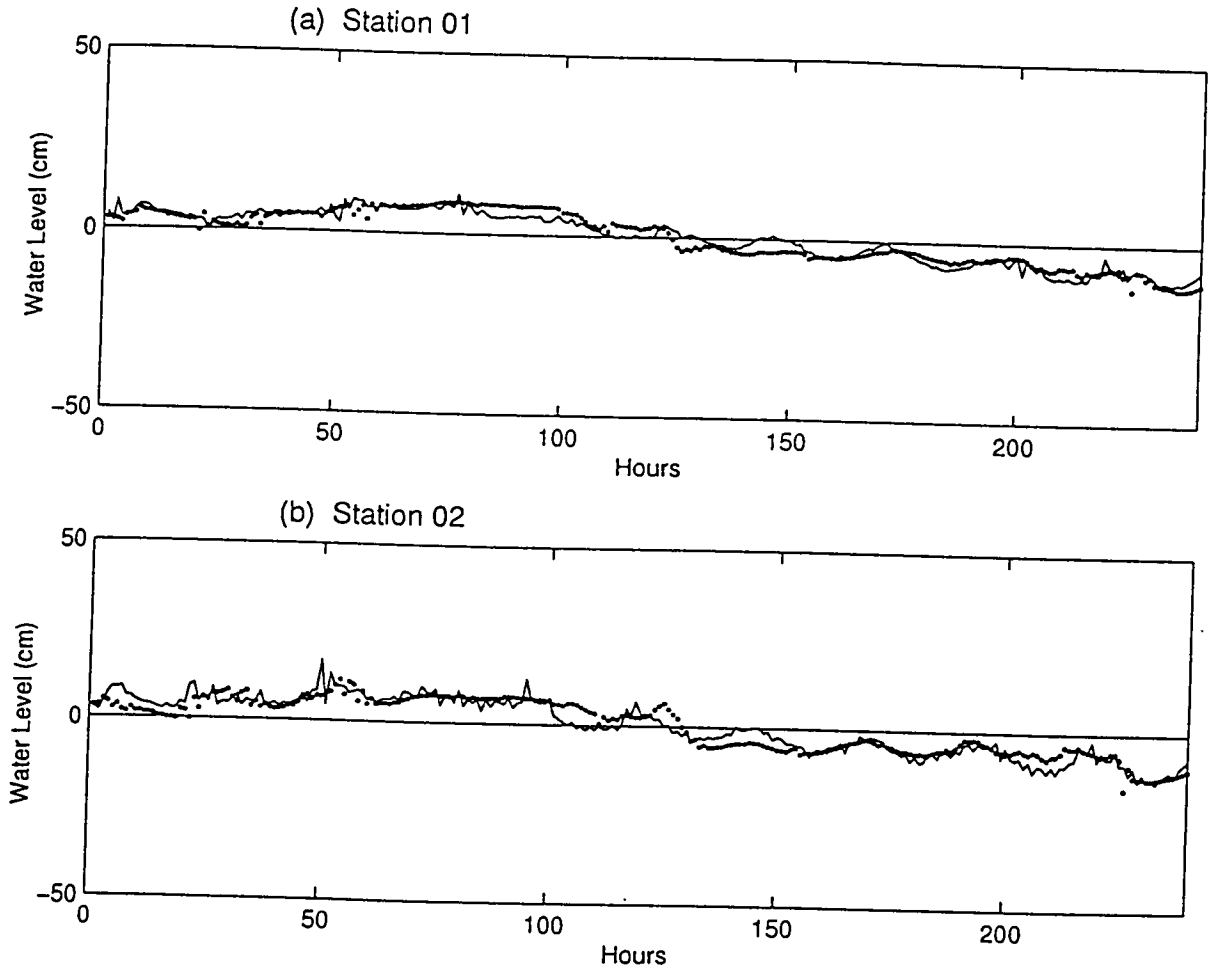

Figure 22. Comparison of the observed (solid line) and the simulated (dotted line) sea level height. (a) At St. 01. (b) At St. 02.

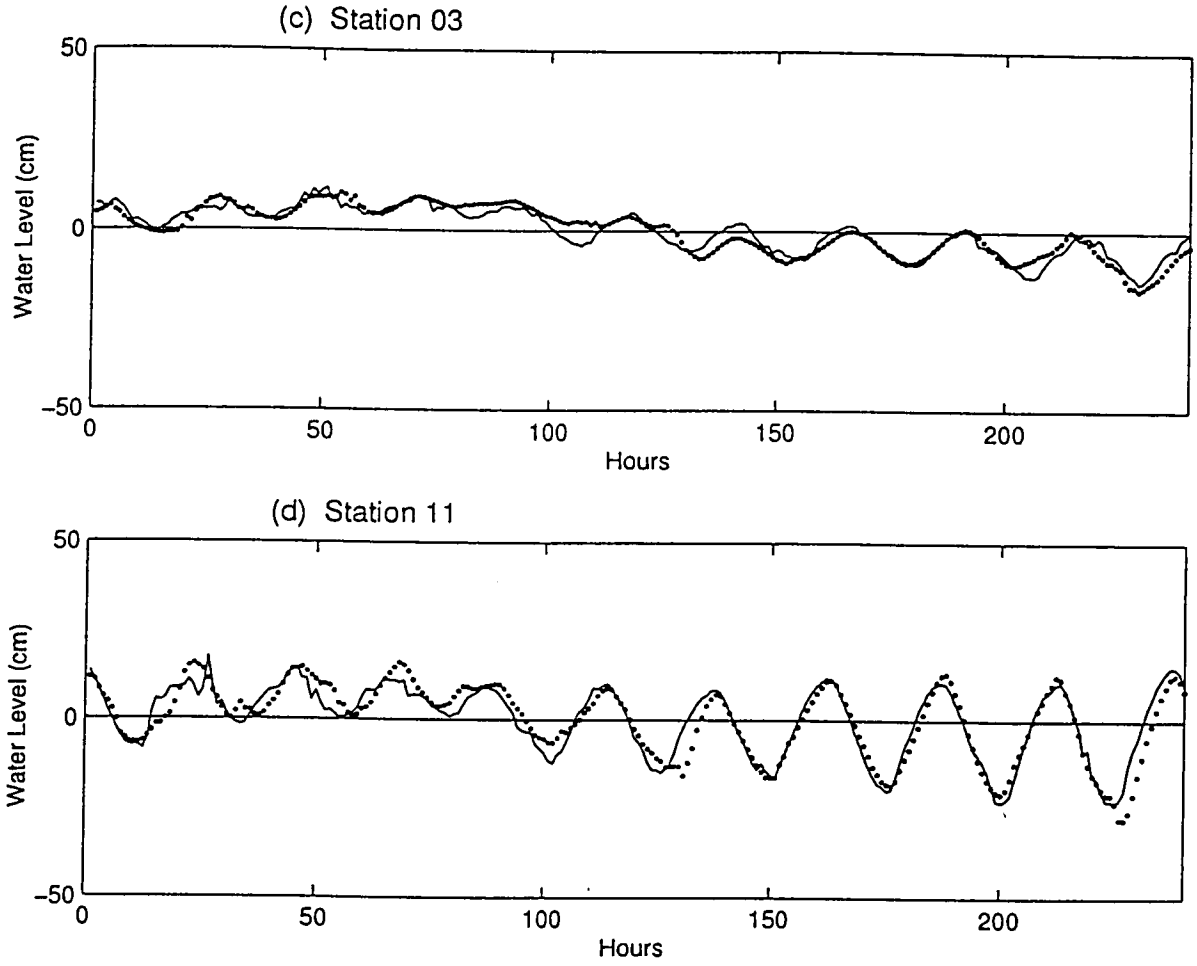

Figure 22. Comparison of the observed (solid line) and the simulated (dotted line) sea level height. (c) At St. 03. (d) At St. 11.

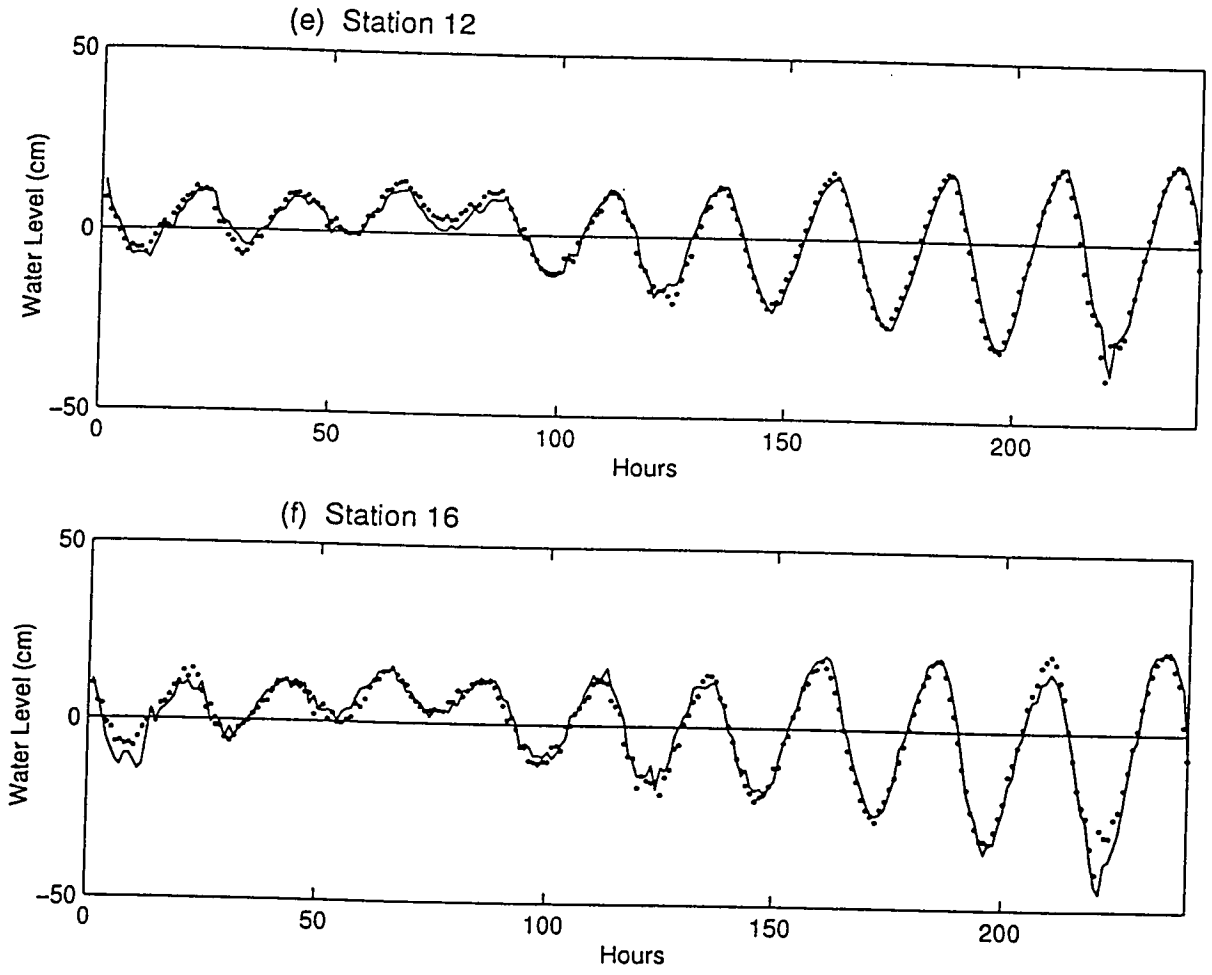

Figure 22. Comparison of the observed (solid line) and the simulated (dotted line) sea level height. (e) At St. 12. (f) At St. 16.

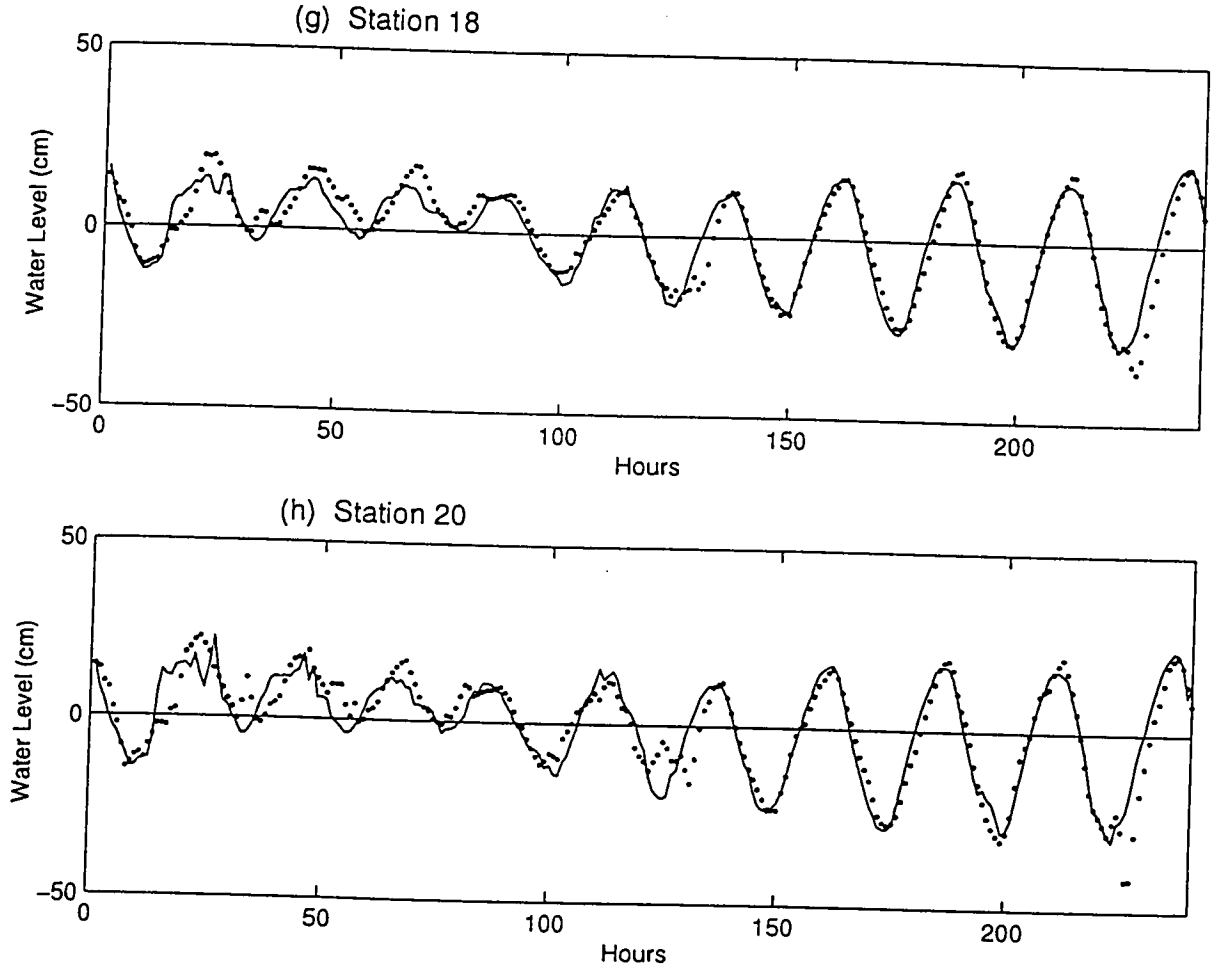

Figure 22. Comparison of the observed (solid line) and the simulated (dotted line) sea level height. (g) At St. 18. (h) At St. 20.

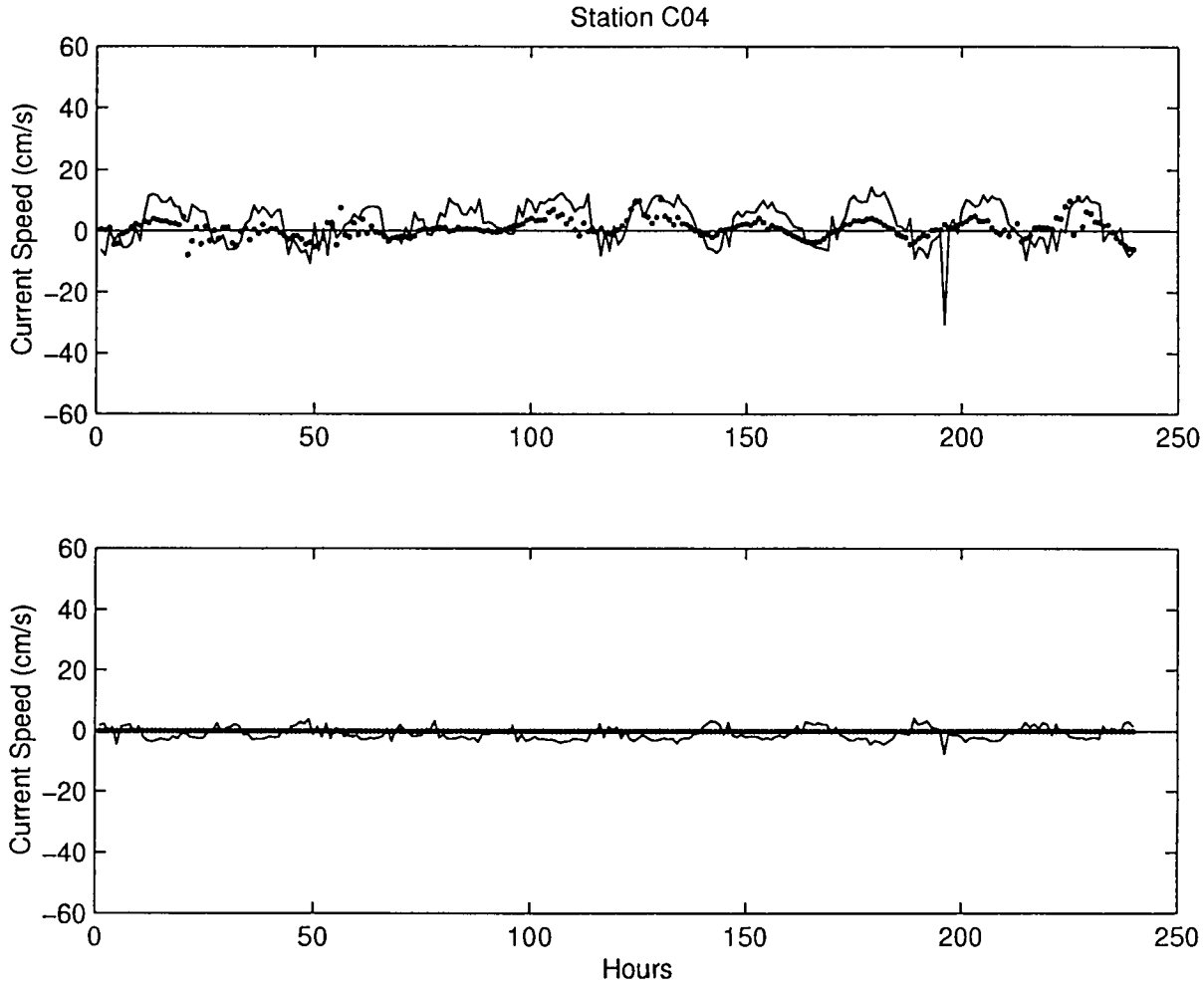

Figure 23a. Comparison of the observed (solid line) and the simulated (dotted line) current components. East-west component (top figure) and north-south component (bottom figure) at St. 04.

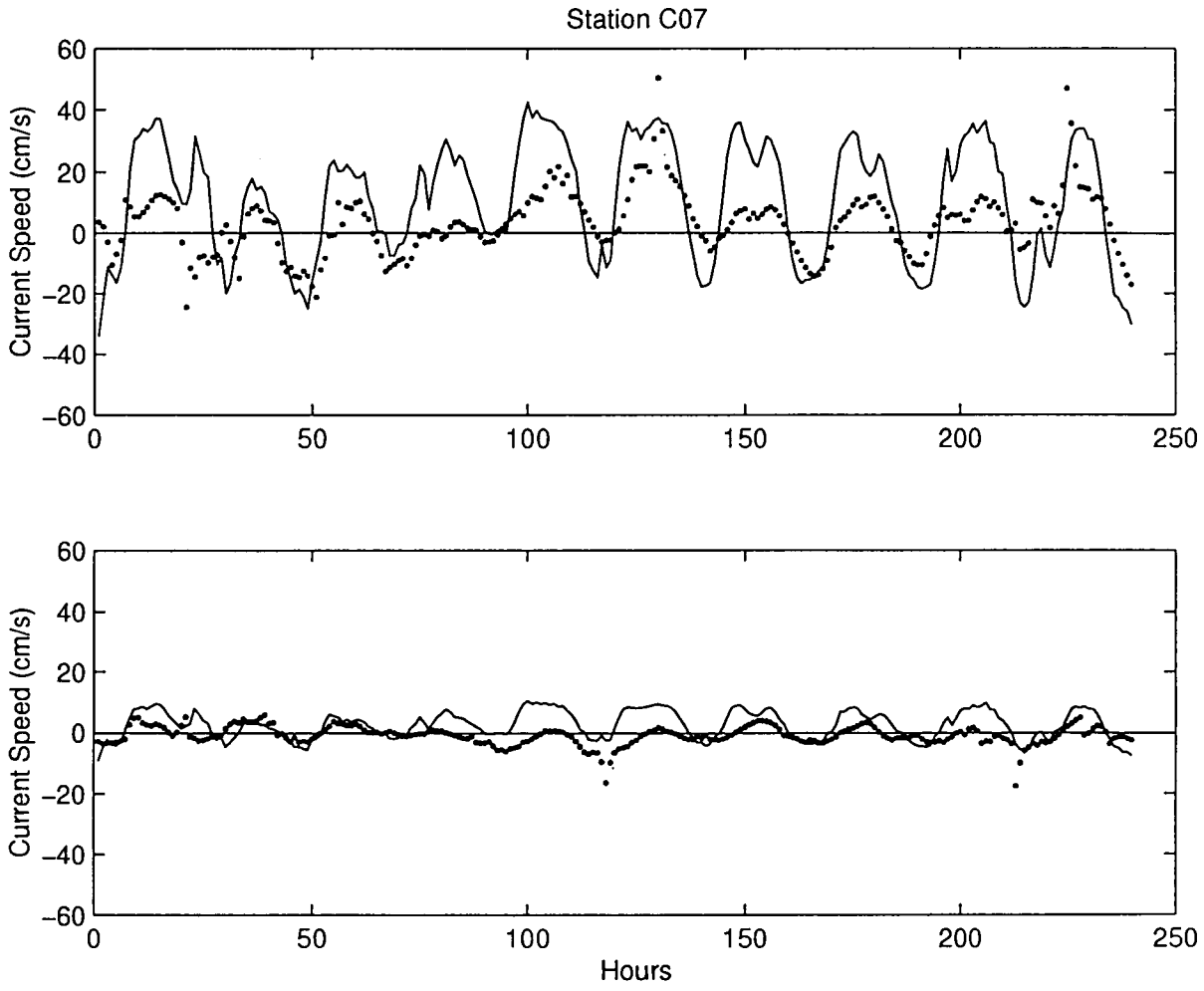

Figure 23b. Comparison of the observed (solid line) and the simulated (dotted line) current components. East-west component (top figure) and north-south component (bottom figure) at St. 07.

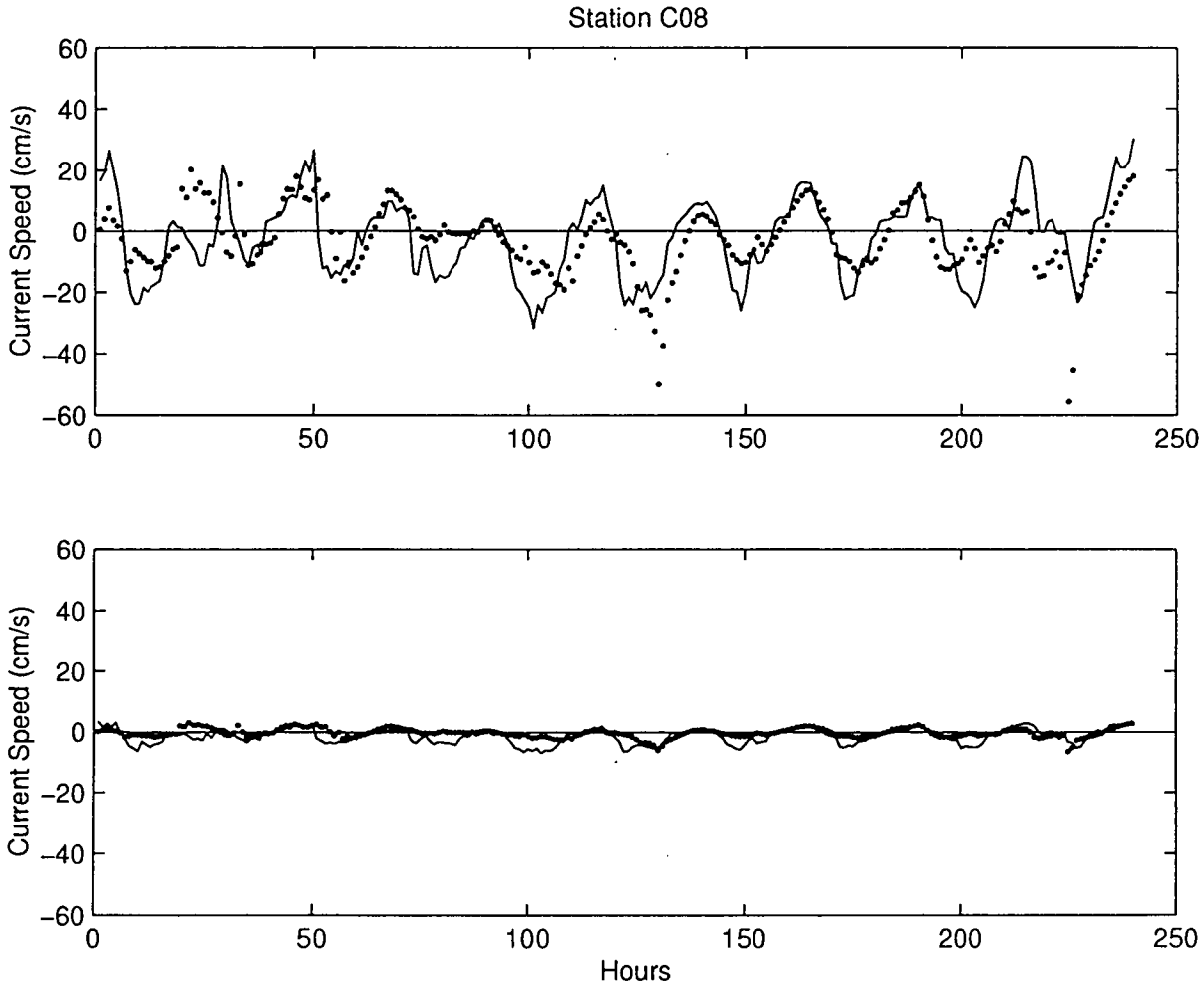

Figure 23c. Comparison of the observed (solid line) and the simulated (dotted line) current components. East-west component (top figure) and north-south component (bottom figure) at St. 08.

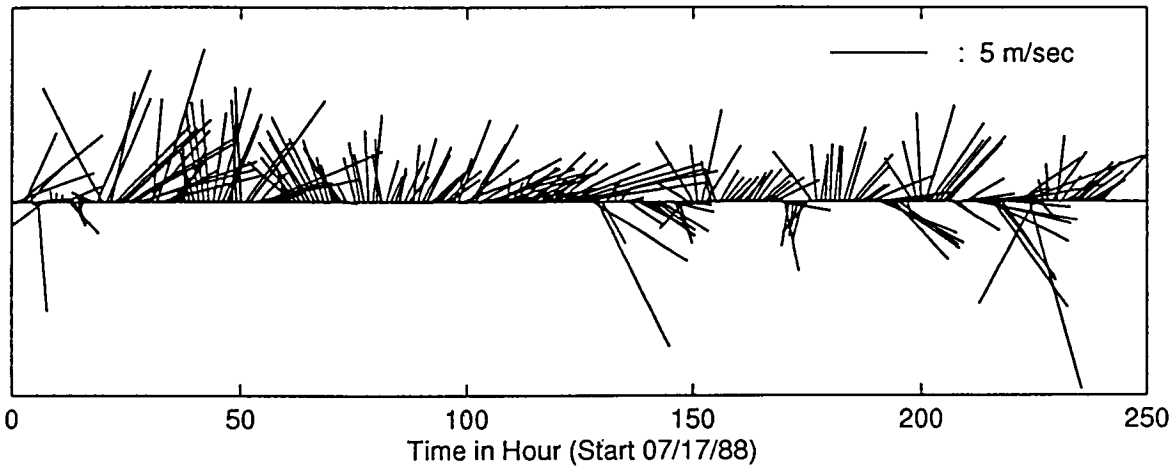

Figure 24. Wind vectors observed at Grand Isle for the period 07/17/88-07/27/88.

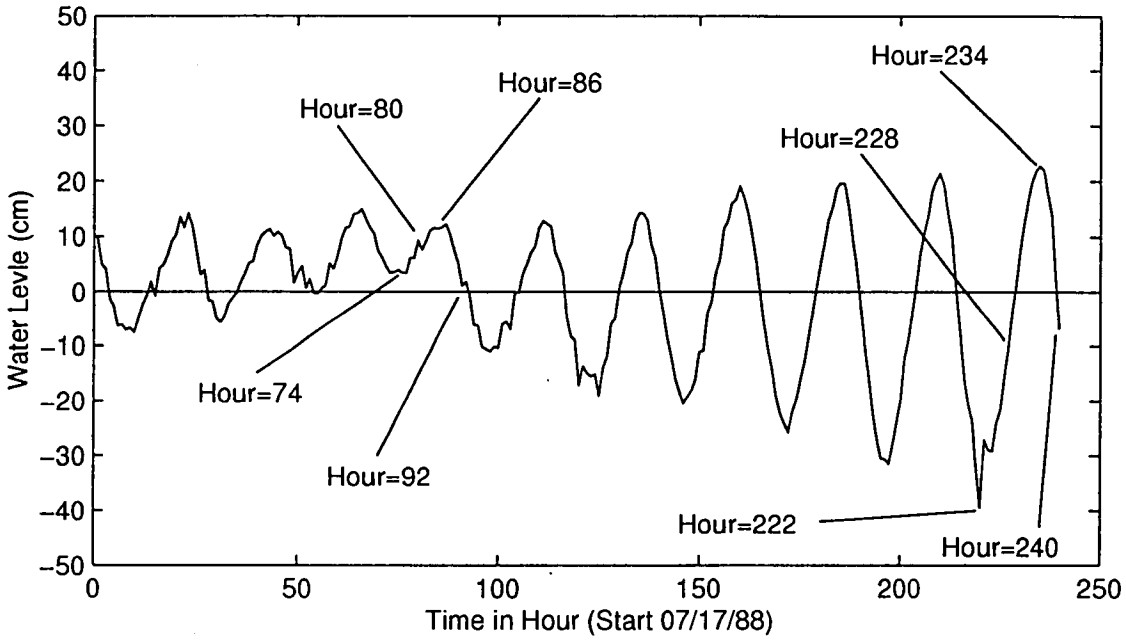

Figure 25. Sea level height simulated at St. 16 (at the mouth of Barataria Bay) and eight instantaneous moments (74th, 80th, 86th and 92nd hour represent low, maximum flood, high and maximum ebb tides, respectively, during a tidal cycle of equatorial tide; 222nd, 228th, 234th and 240th hour represent low, maximum flood, high and maximum ebb tides, respectively, during a tidal cycle of tropic tides).

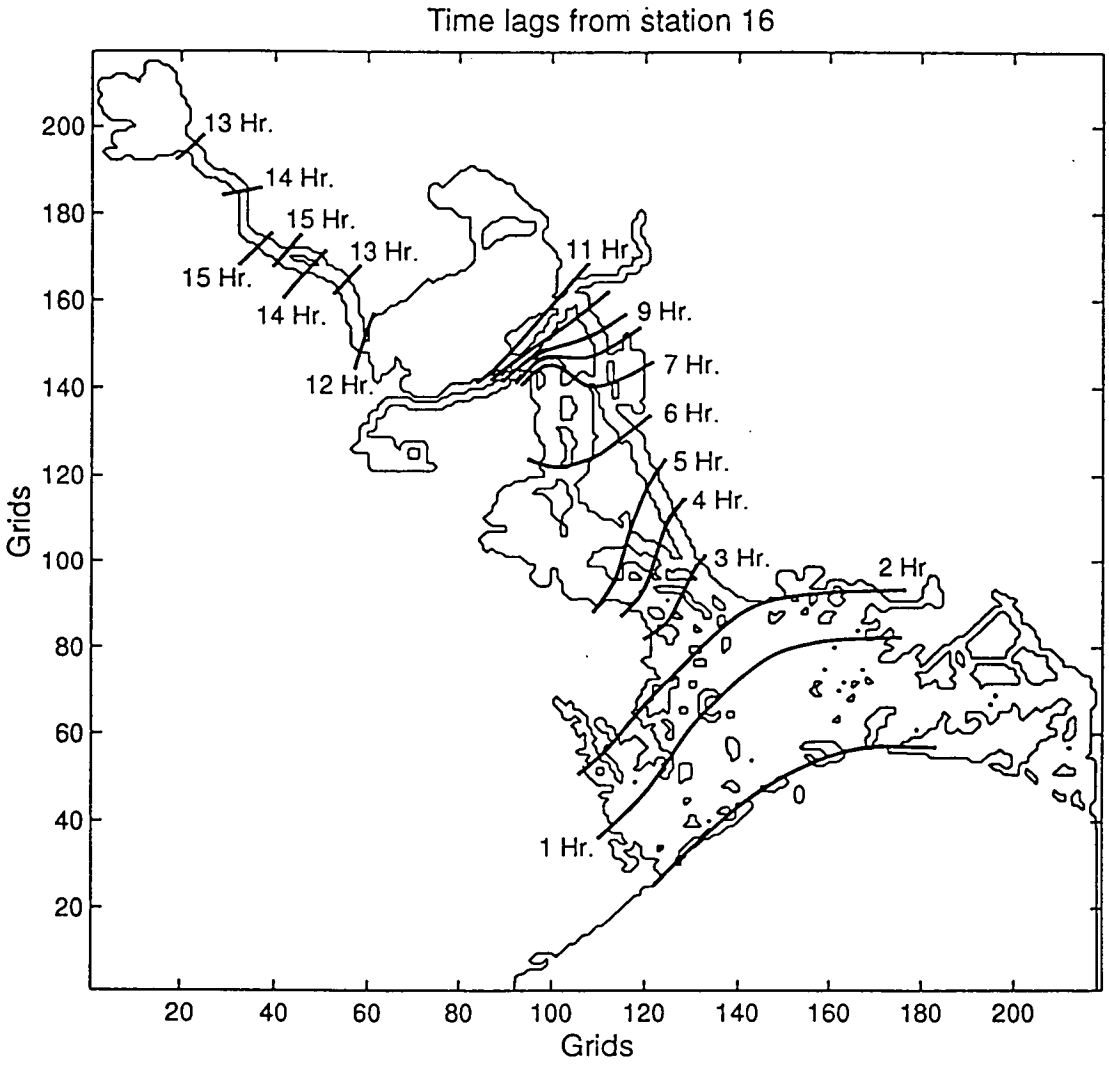

Figure 26. Tidal propagation simulated in the model. Time lags relative to station 16 are shown.

Salvador appears to be the result of the superposition of the propagating tides and the basin mode. It is interesting to note that Byrne et al. (1976) identified gentle diurnal oscillations in the upper reaches of Barataria Bay that appear to be forced by sea breeze and not by tide coming from the Gulf of Mexico. Due to the complexity of waterways and canals, it takes longer for the tides to propagate between Bayou Perot and Lake Salvador than other areas.

Examples of simulated current fields are presented in Figures 27a through 27h. It is clear that the lower domain of the basin is characterized by much stronger currents compared to the upper domain, because the primary forcing, which is tidal, comes from the open Gulf. It is evident that the main tidal flow enters the basin primarily through two deep passes, Barataria Pass and Pass Abel, and follows the deeper bathymetric contours toward Bayou Rigolettes and Little Lake. Tidal currents dominate flow along the axis of the basin, while wind plays a significant role in controlling lateral movement of water. Within the lower domain, stronger currents are found in deeper parts of the basin. Maximum flood as well as ebb tidal currents could approach 100 cm s^{-1} in tidal passes such as Barataria Pass and Pass Abel, in agreement with previous observations (Marmer, 1948). In other tidal passes, such as Caminada Pass, maximum currents are usually limited 50~60 cm s^{-1} . Within the upper reach of the basin, significant currents are found only in the narrow waterways, often exceeding 25 cm s^{-1}. Tidal currents are significantly diminished in the uppermost reach of the basin, namely Lac des Allemands. It appears that the local wind forcing becomes more important in the upper reaches of the basin compared to the tidal forcing. A sensitivity test was carried out with and without wind forcing to evaluate the impact of local wind forcing. It turns out that the effects of wind forcing at Sts. 12 and 16, located at the mouth of the basin, were negligible. However, it was significant at other stations inside the bay.

3.4 Flushing Characteristics

Flushing characteristics of the basin were examined by releasing tracer particles, and tracking the trajectories of those particles. After a model spin-up of ten simulation days, tracer particles were released in the model with one particle at every grid point throughout the basin (Figure 28a). The tracer particles were tracked for the next ten simulation days. The principal subtidal circulation pattern revealed by the tracer experiment (Figures 28a - 28f) indicates that an inflow tends to occur through passes located on the western side, while outflow tends to occur through eastern passes. However, the resulting net subtidal circulation pattern appears to be dictated by the wind pattern as observed for Terrebonne/Timbalier Basin. The significant westerly wind component observed during the simulation period is anomalous (see Gutierrez de Velasco and Winant, 1996). It should be noted that the accumulation of tracers just outside the basin on its eastern side is an artifact. It is due to the presence of an artificial solid wall along the eastern side of the model basin with no specification of long-shore currents in the model.

Efficiency of flushing of a basin can be measured by computing flushing time, which is defined here as the time required to flush out a fraction $1-e^{-1}$ of the particles initially deployed. Flushing time is computed for a subset of tracer particles to define flushing time for eight sub-basins shown in Figure 29. Initial as well as final distribution patterns of tracer particles after ten simulation days for each of the eight sub-basins are presented in Figures 30a - 30c. Estimated

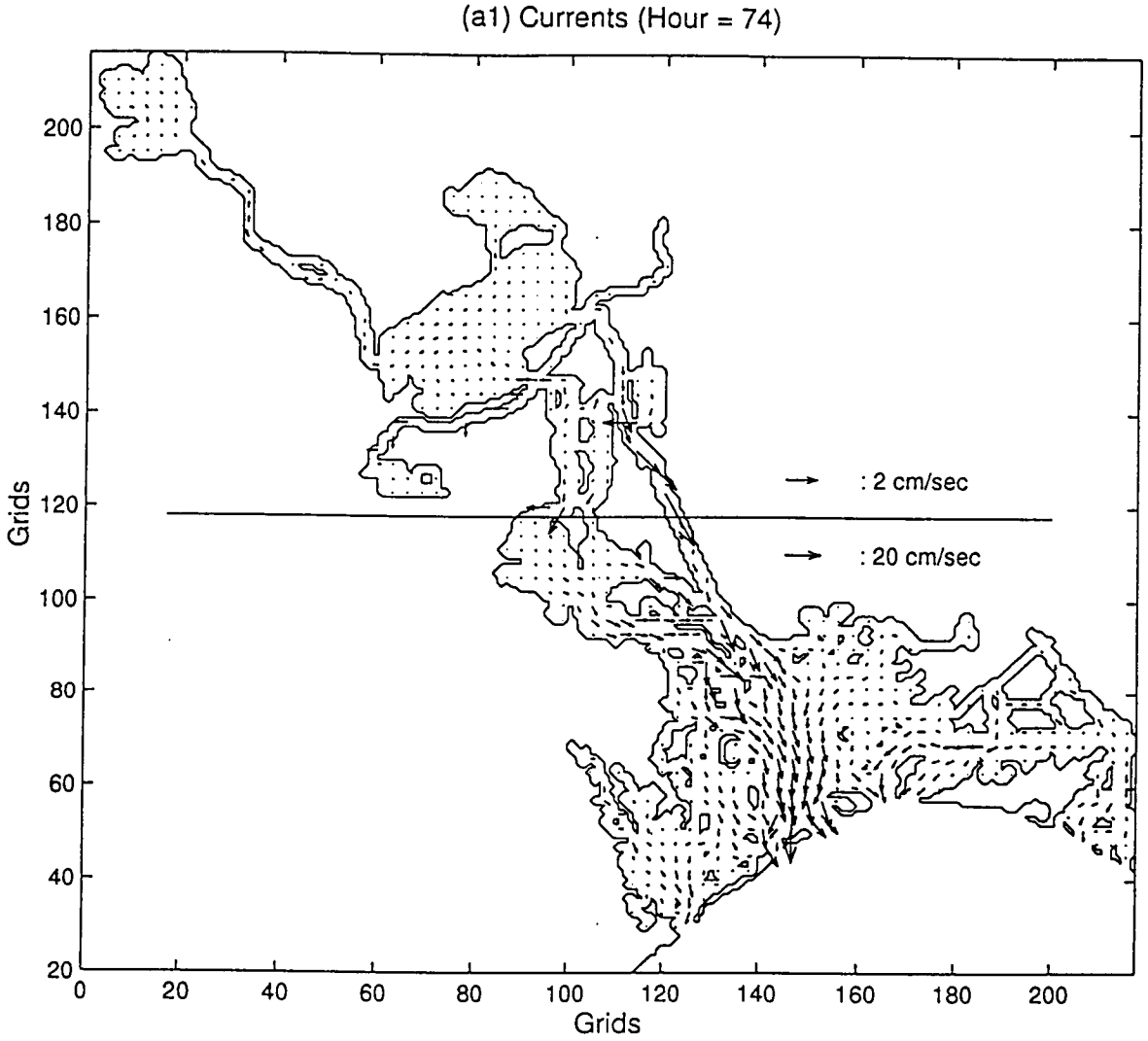

Figure 27a. Simulated currents in Barataria Basin at Hour 74. Different scalings for velocity vector are used for the upper and lower domains. Reference velocity vectors are indicated.

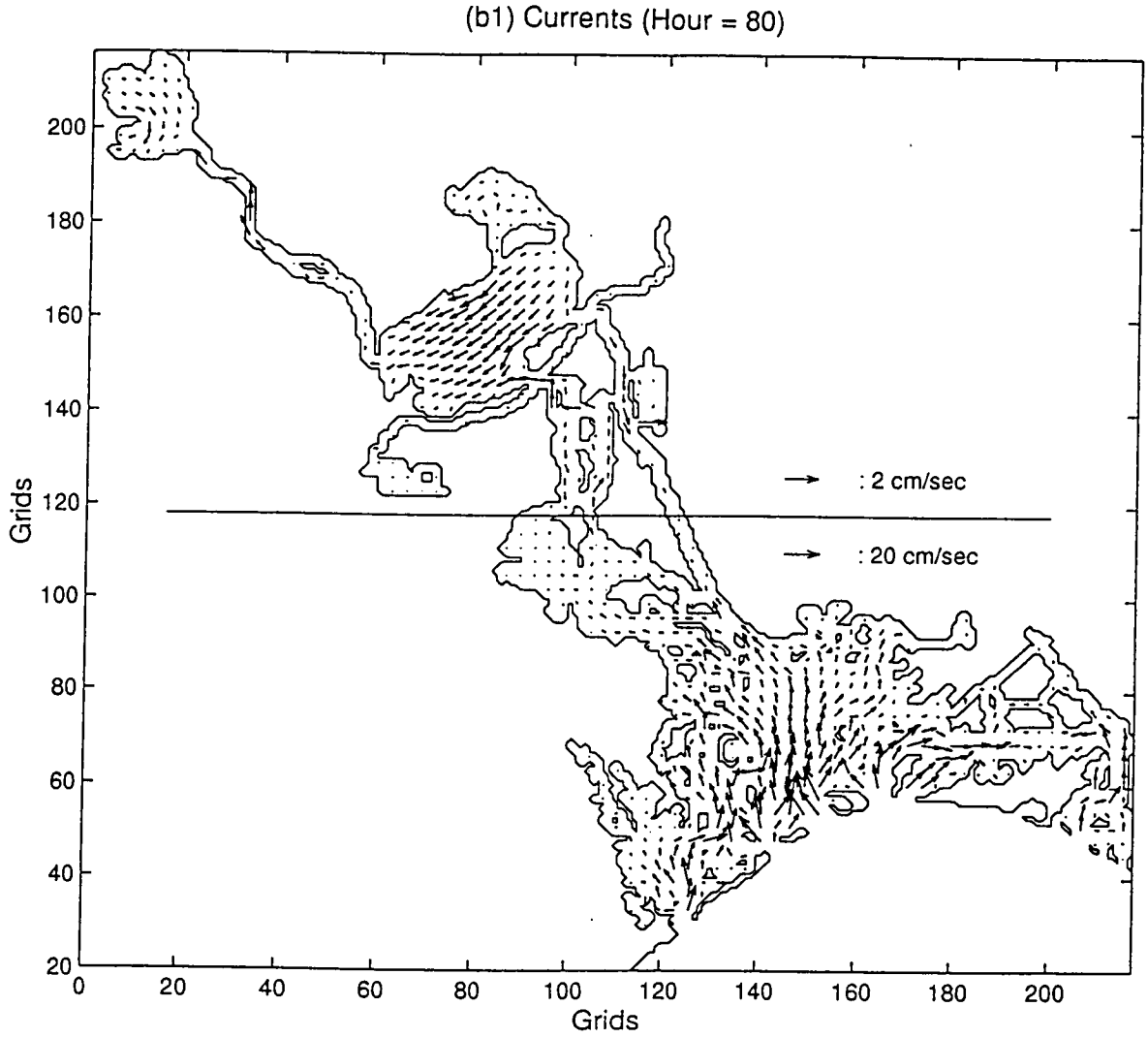

Figure 27b. Simulated currents in Barataria Basin at Hour 80. Different scalings for velocity vector are used for the upper and lower domains. Reference velocity vectors are indicated.

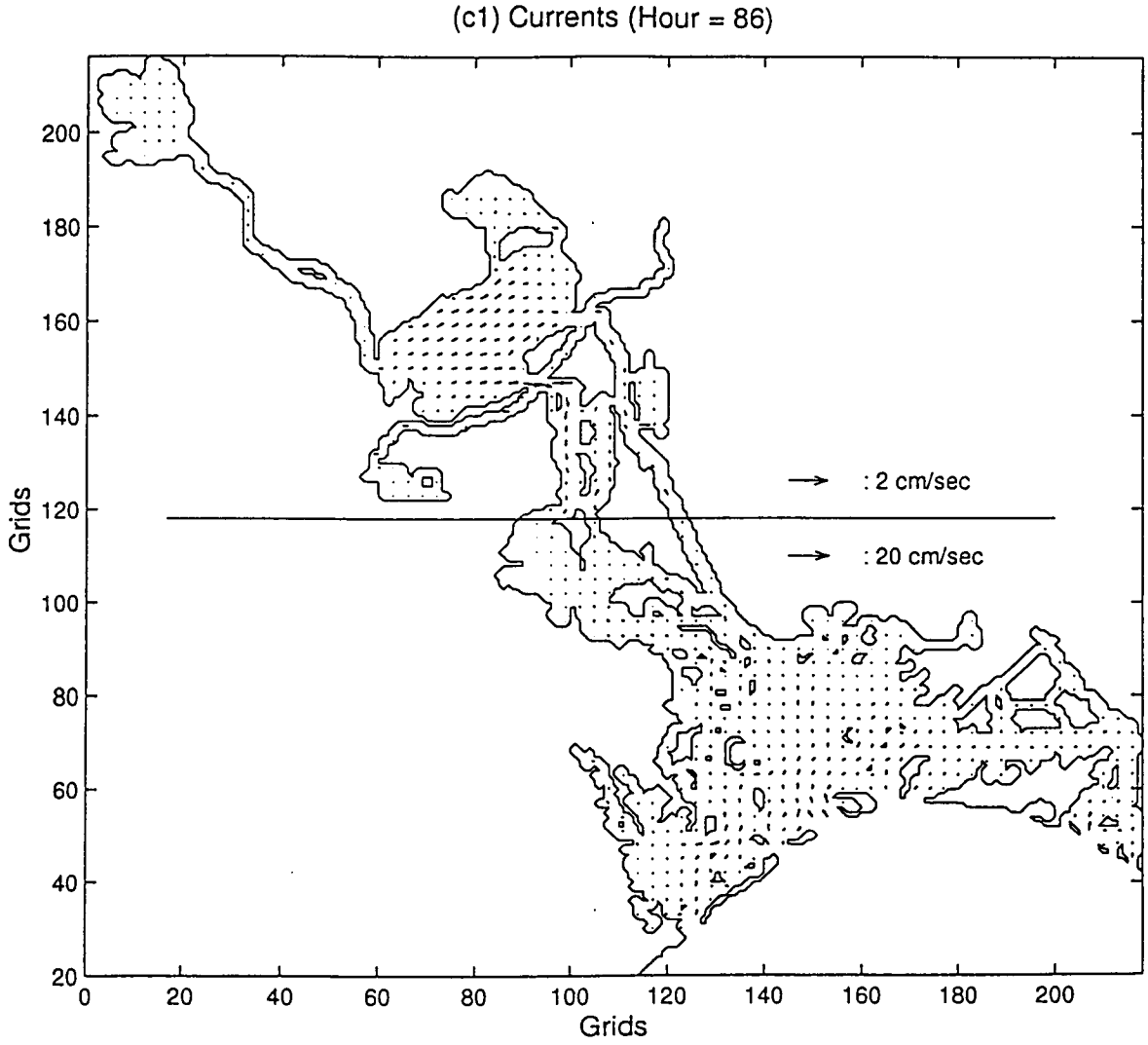

Figure 27c. Simulated currents in Barataria Basin at Hour 86. Different scalings for velocity vector are used for the upper and lower domains. Reference velocity vectors are indicated.

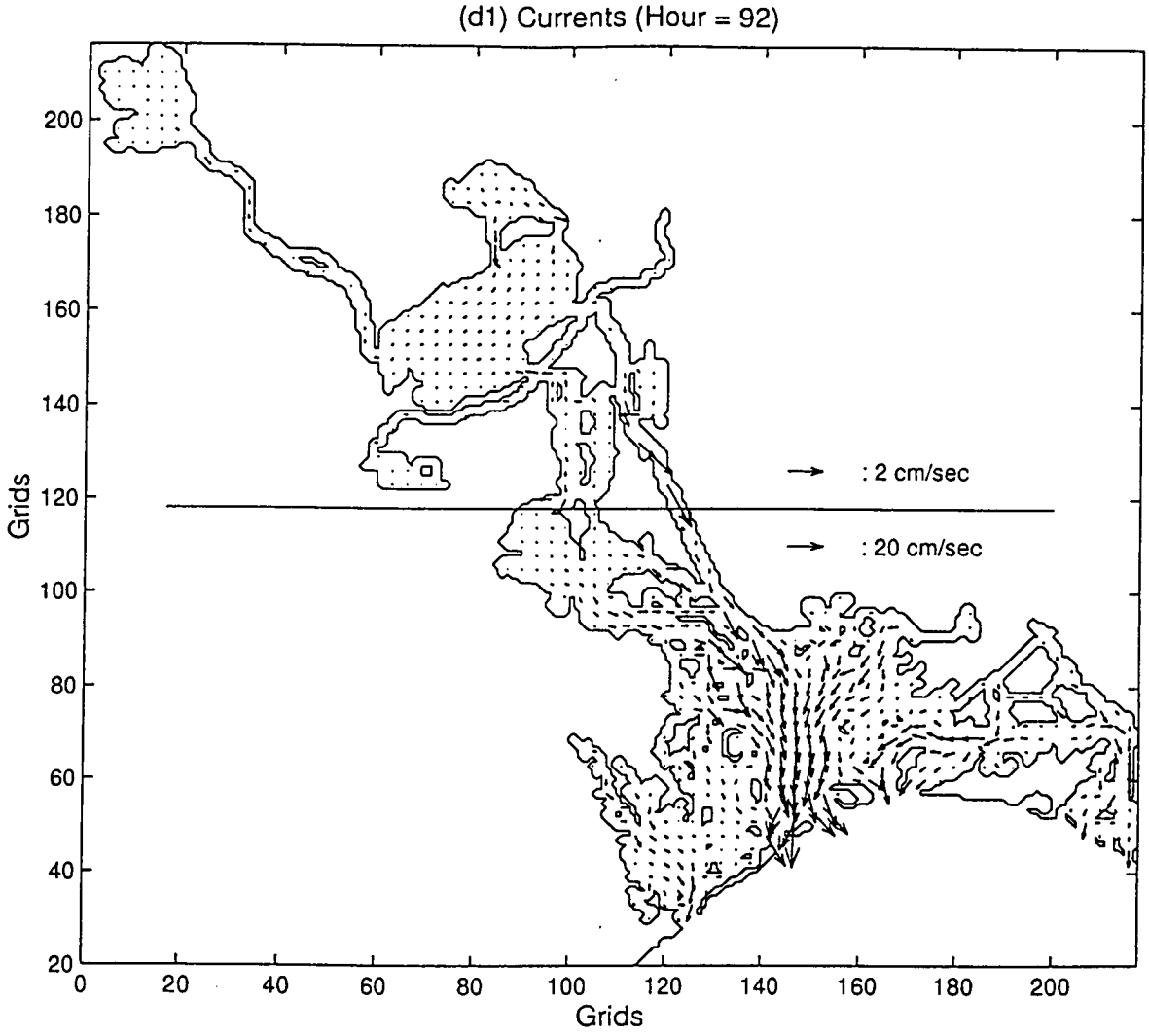

Figure 27d. Simulated currents in Barataria Basin at Hour 92. Different scalings for velocity vector are used for the upper and lower domains. Reference velocity vectors are indicated.

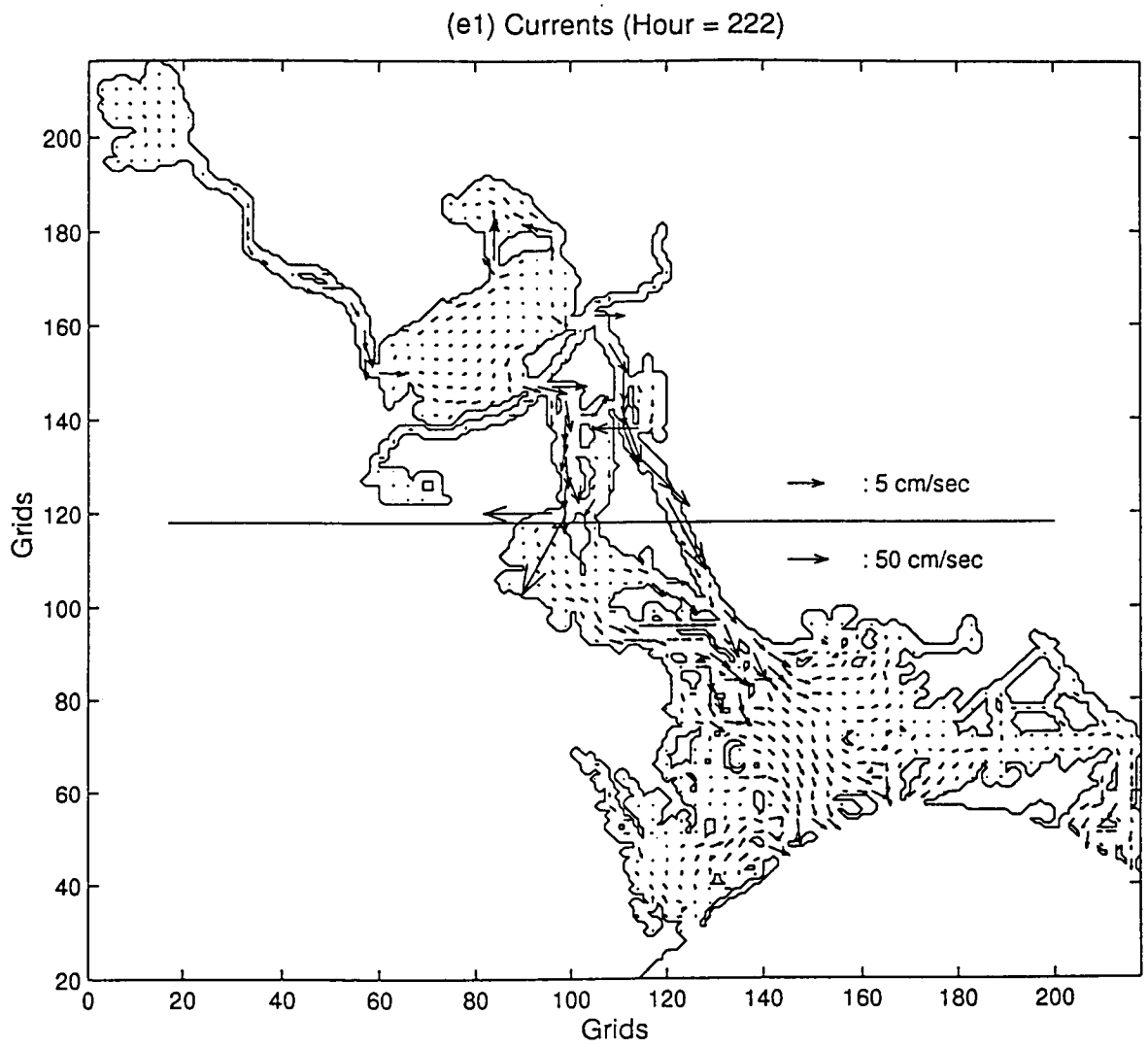

Figure 27e. Simulated currents in Barataria Basin at Hour 222. Different scalings for velocity vector are used for the upper and lower domains. Reference velocity vectors are indicated.

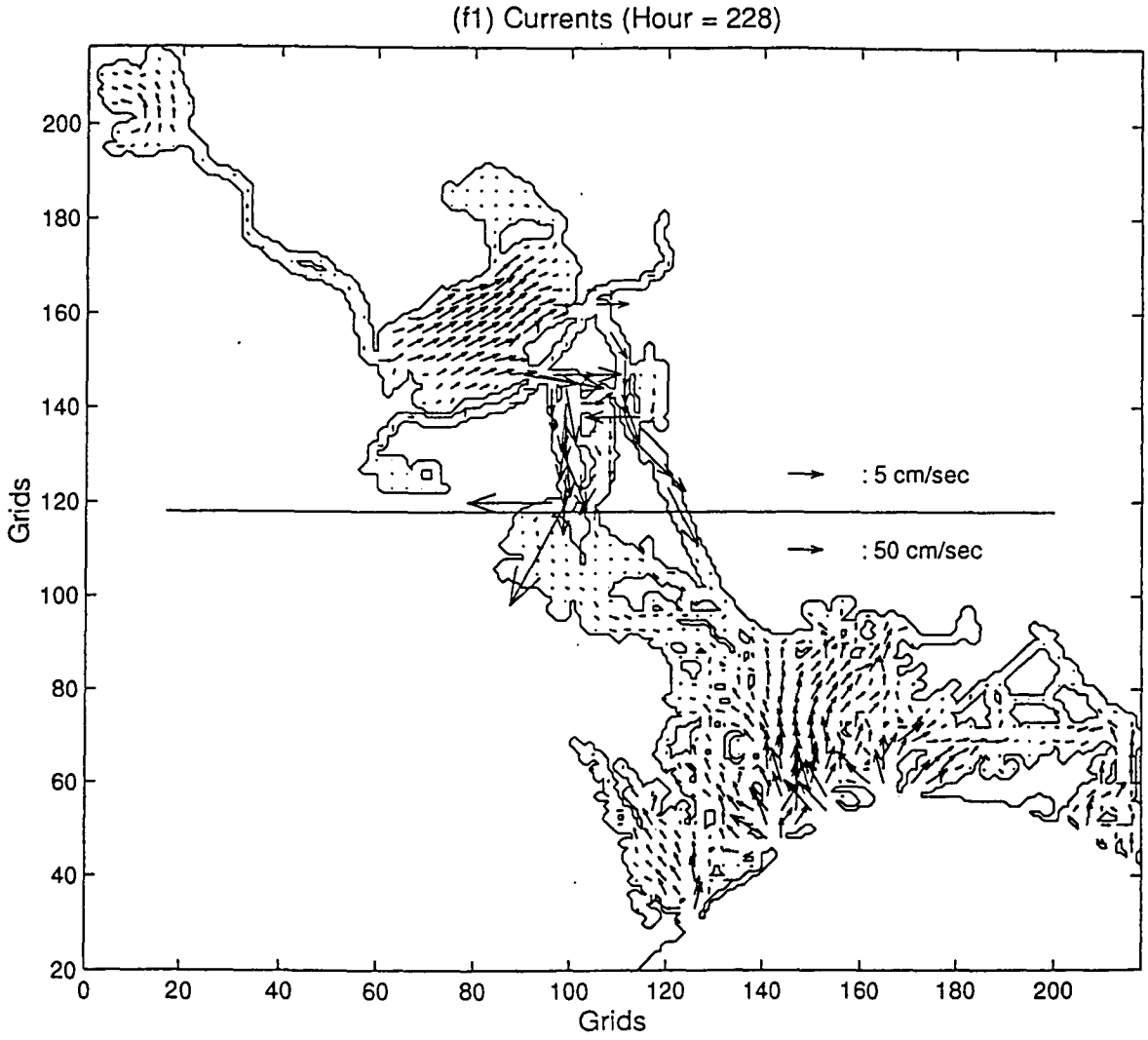

Figure 27f. Simulated currents in Barataria Basin at Hour 228. Different scalings for velocity vector are used for the upper and lower domains. Reference velocity vectors are indicated.

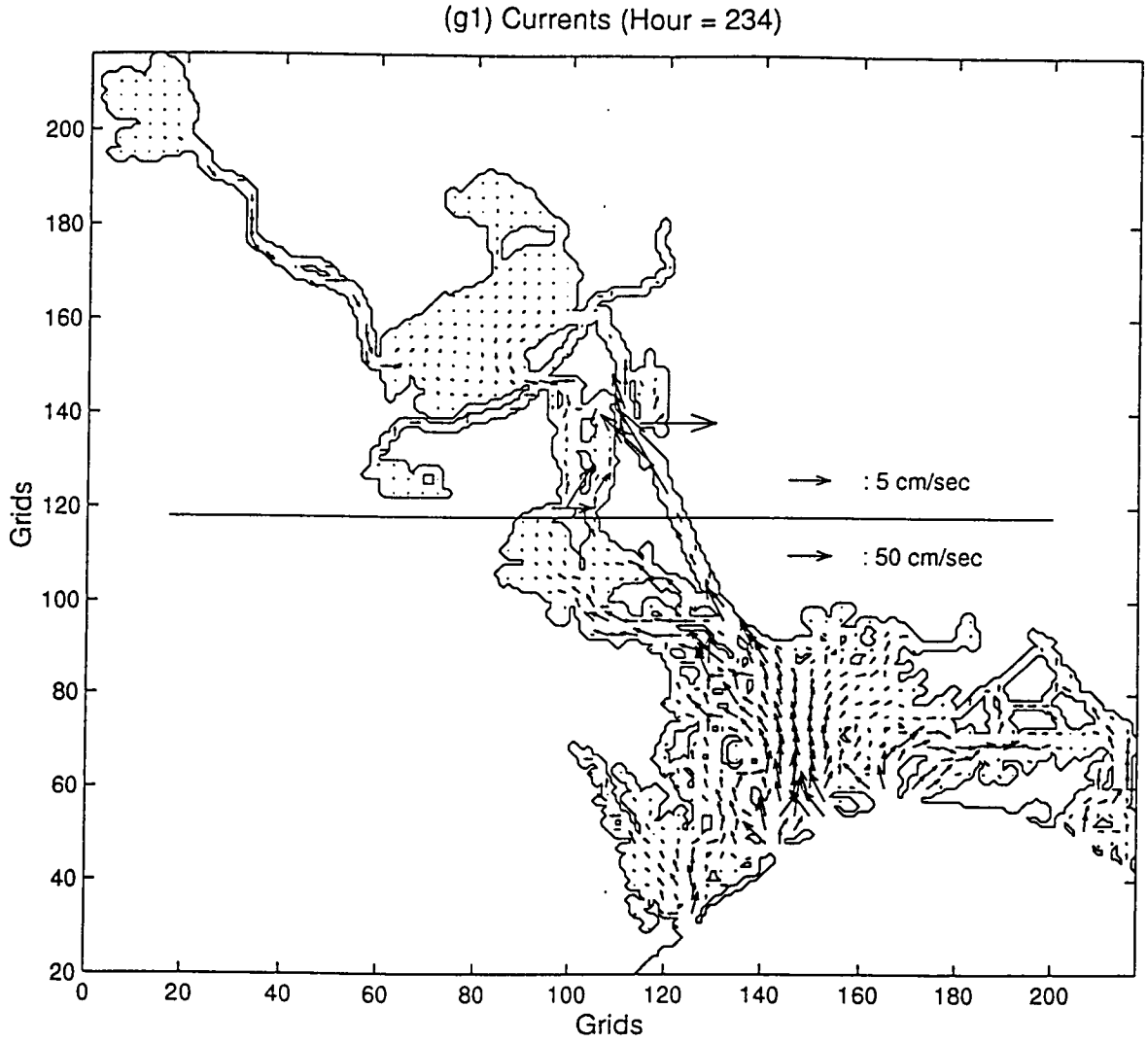

Figure 27g. Simulated currents in Barataria Basin at Hour 234. Different scalings for velocity vector are used for the upper and lower domains. Reference velocity vectors are indicated.

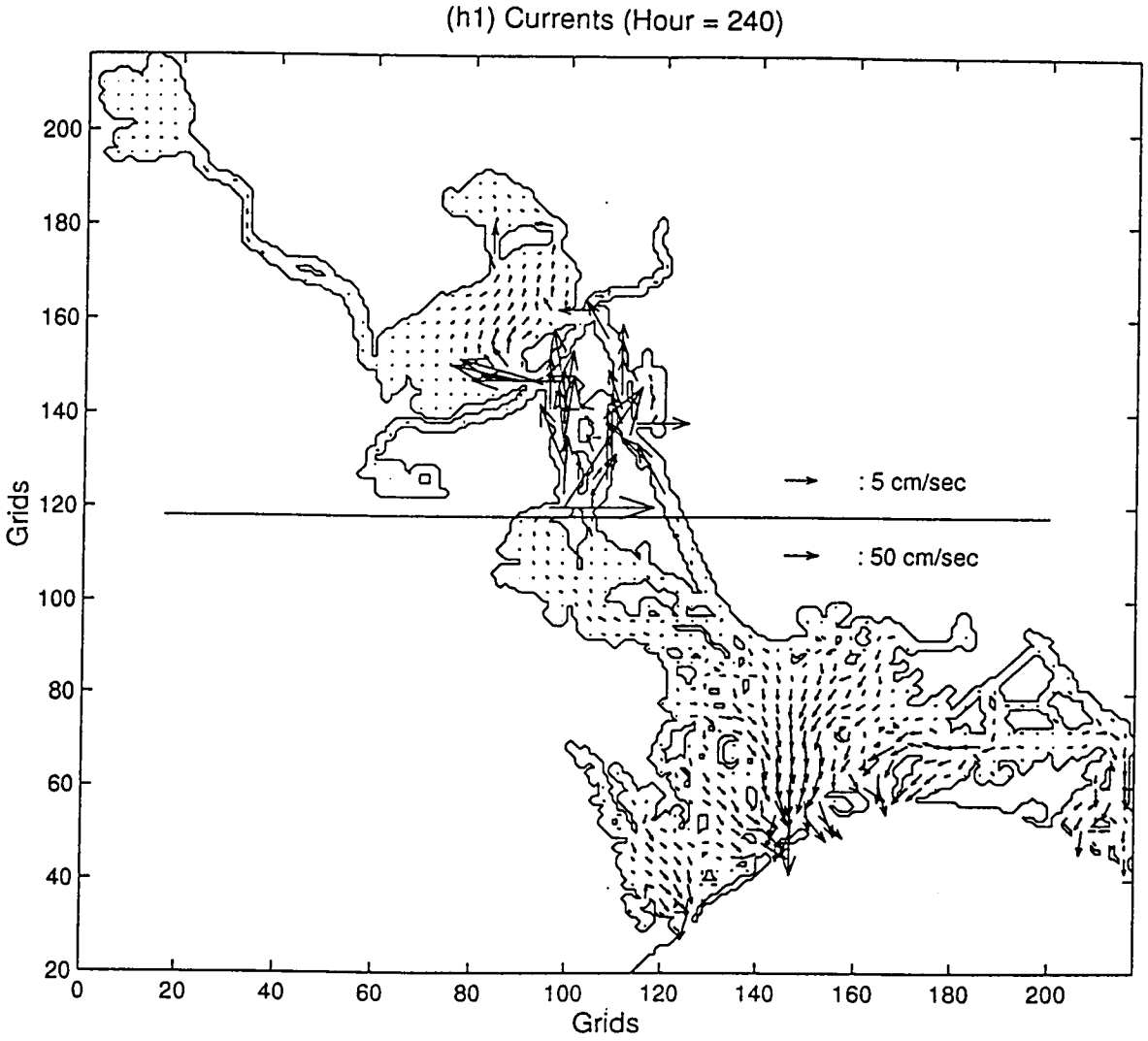

Figure 27h. Simulated currents in Barataria Basin at Hour 240. Different scalings for velocity vector are used for the upper and lower domains. Reference velocity vectors are indicated.

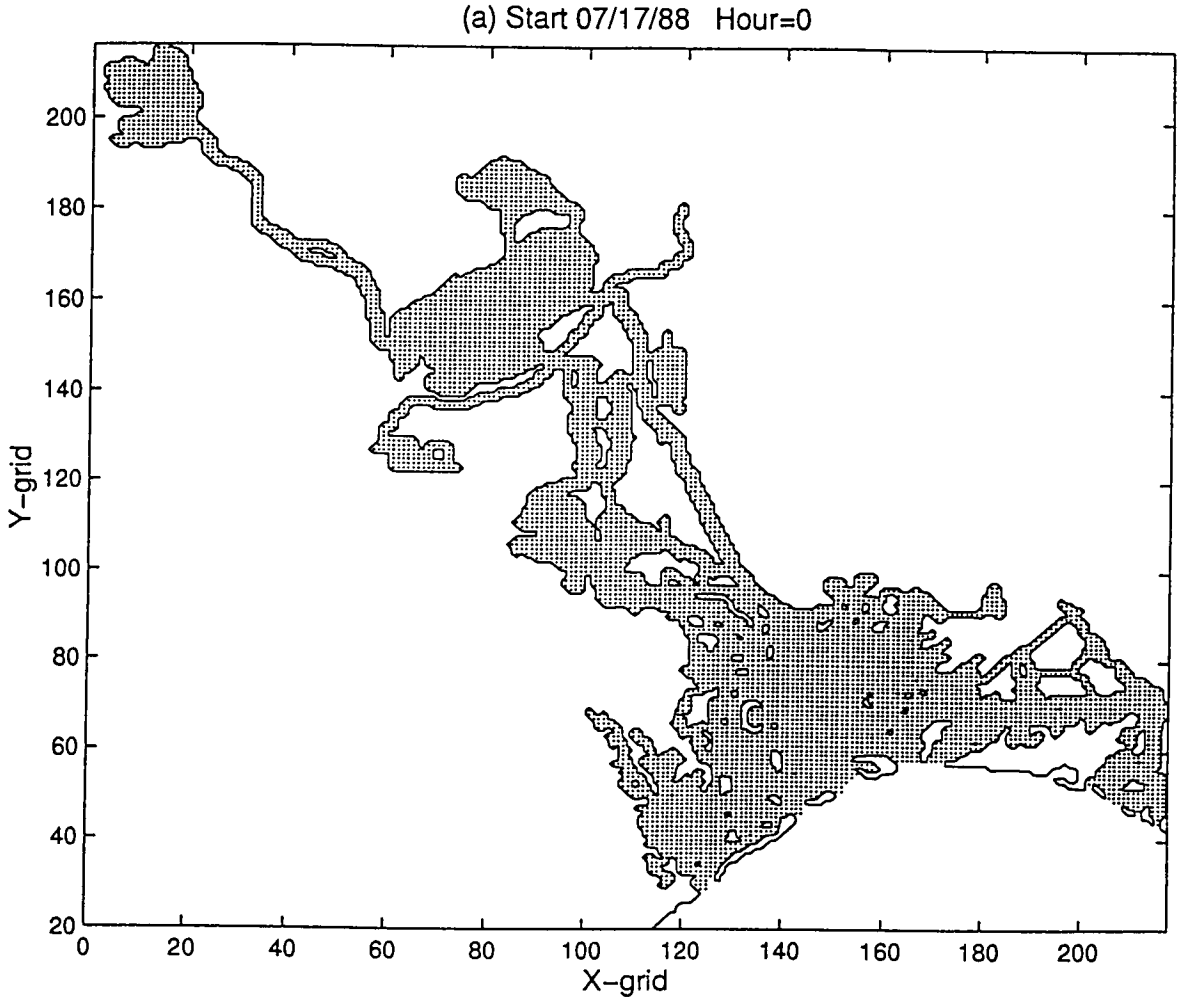

Figure 28a. Distribution of tracer particles simulated for the period 07/17/88-07/27/88 in Barataria Basin. At time of release (0 hr 07/17/88).

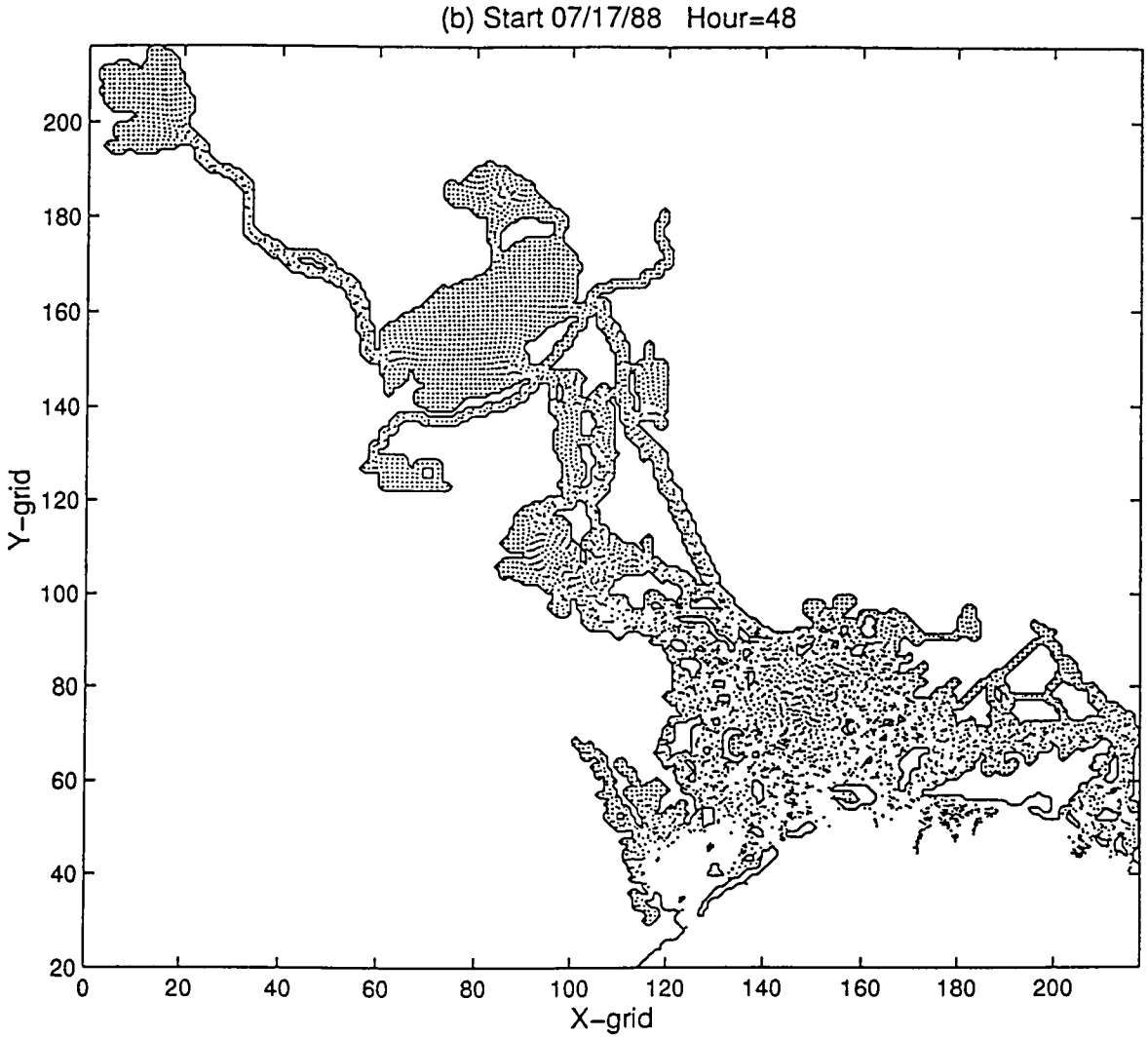

Figure 28b. Distribution of tracer particles simulated for the period 07/17/88-07/27/88 in Barataria Basin. After 48 hours.

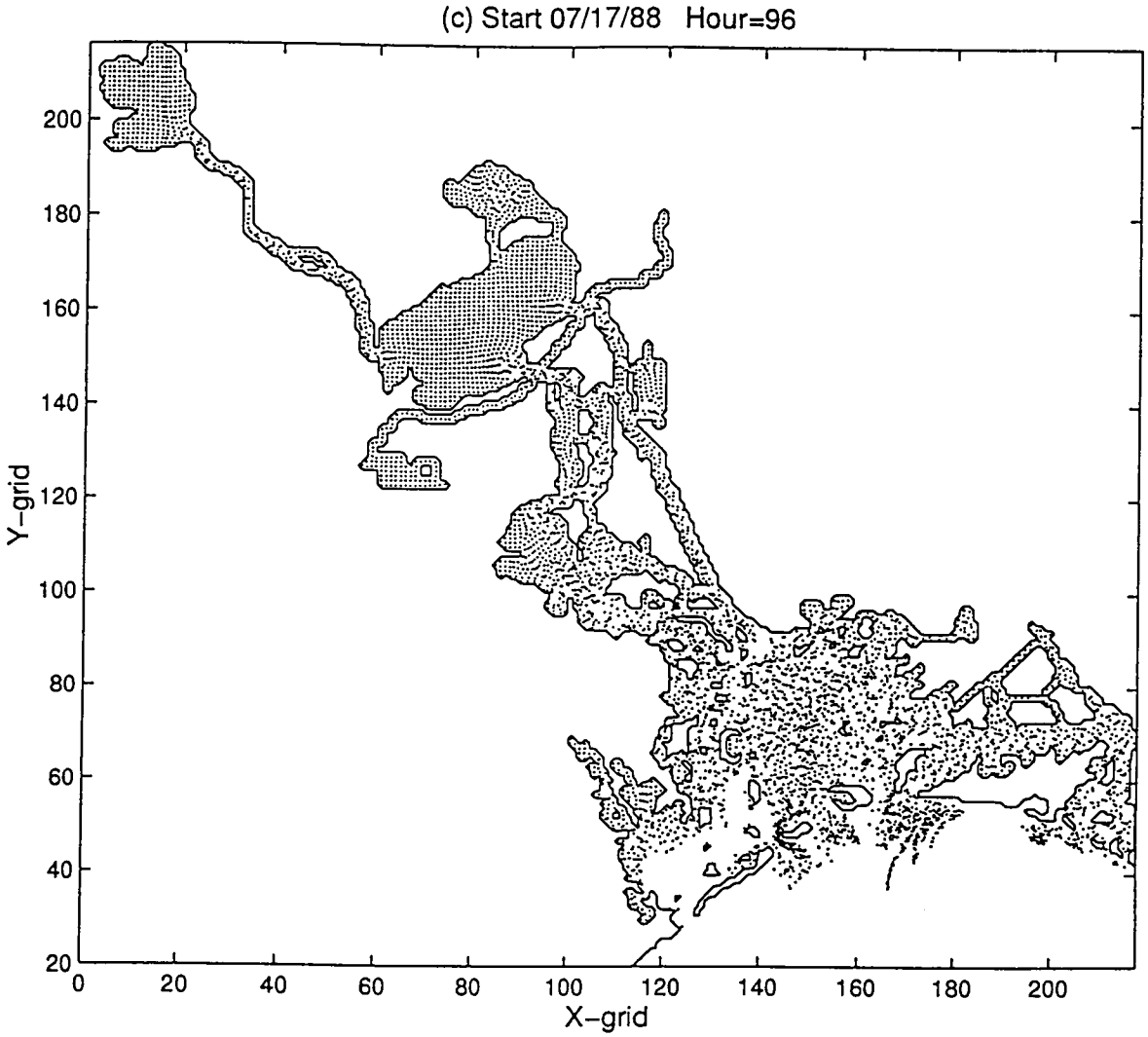

Figure 28c. Distribution of tracer particles simulated for the period 07/17/88-07/27/88 in Barataria Basin. After 96 hours.

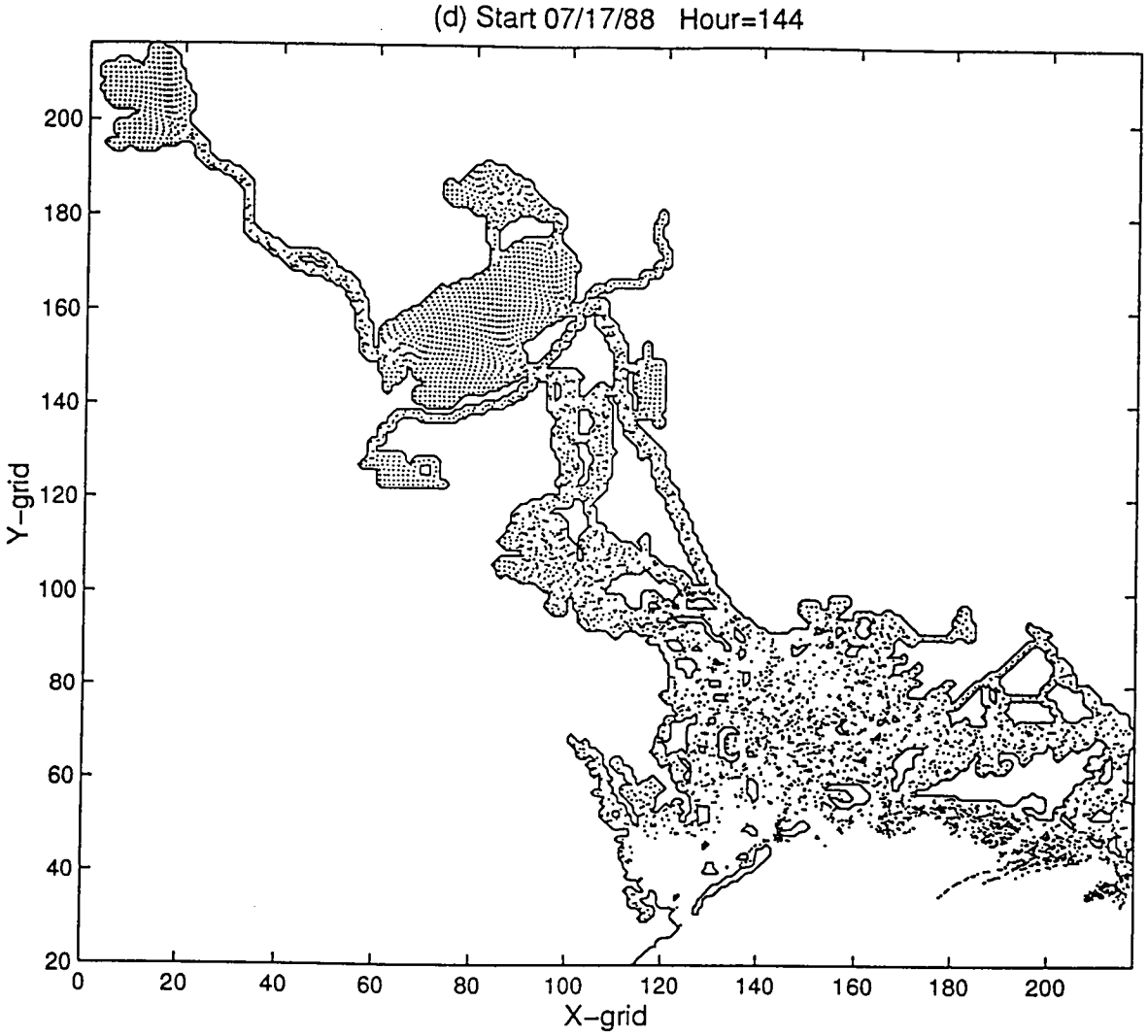

Figure 28d. Distribution of tracer particles simulated for the period 07/17/88-07/27/88 in Barataria Basin. After 144 hours.

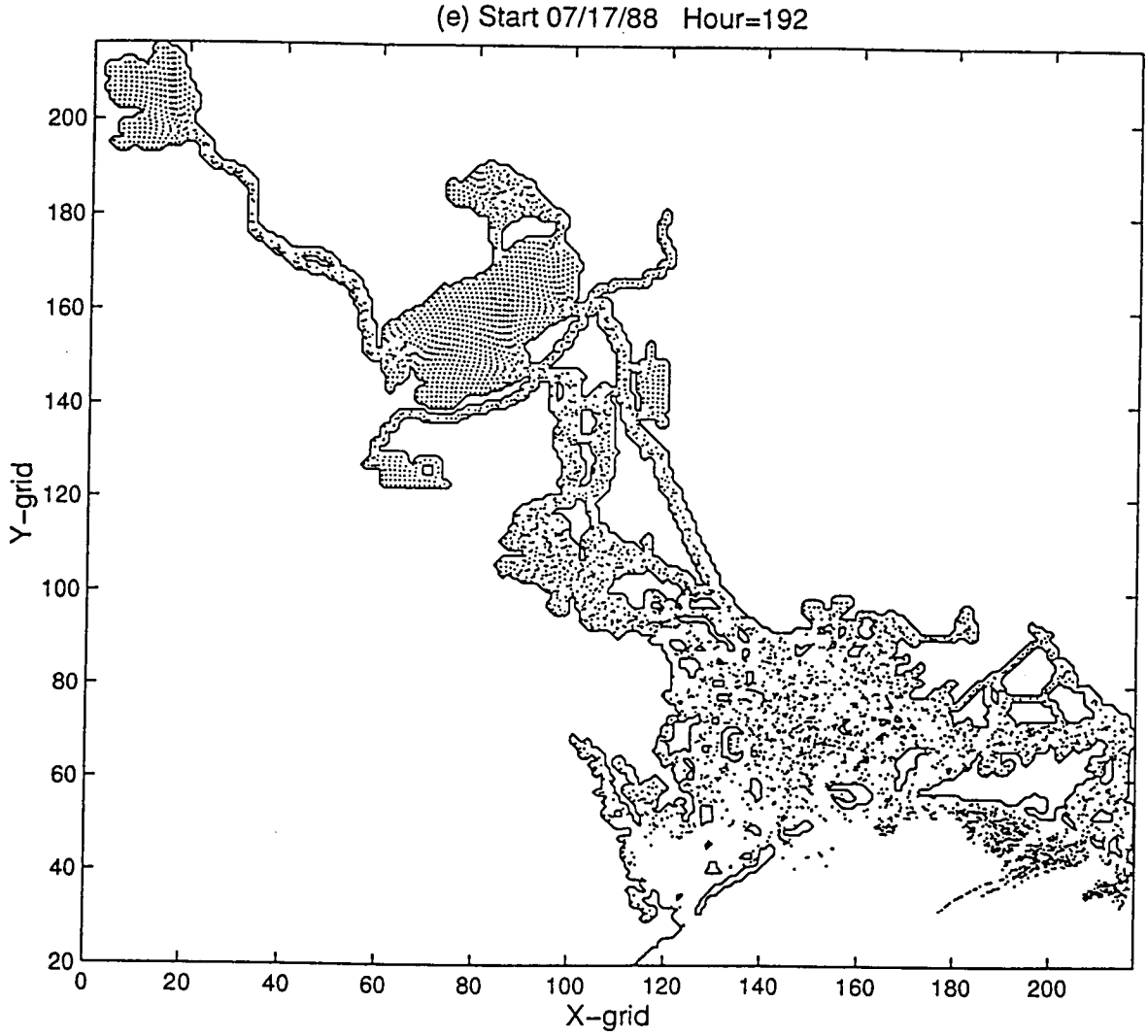

Figure 28e. Distribution of tracer particles simulated for the period 07/17/88-07/27/88 in Barataria Basin. After 192 hours.

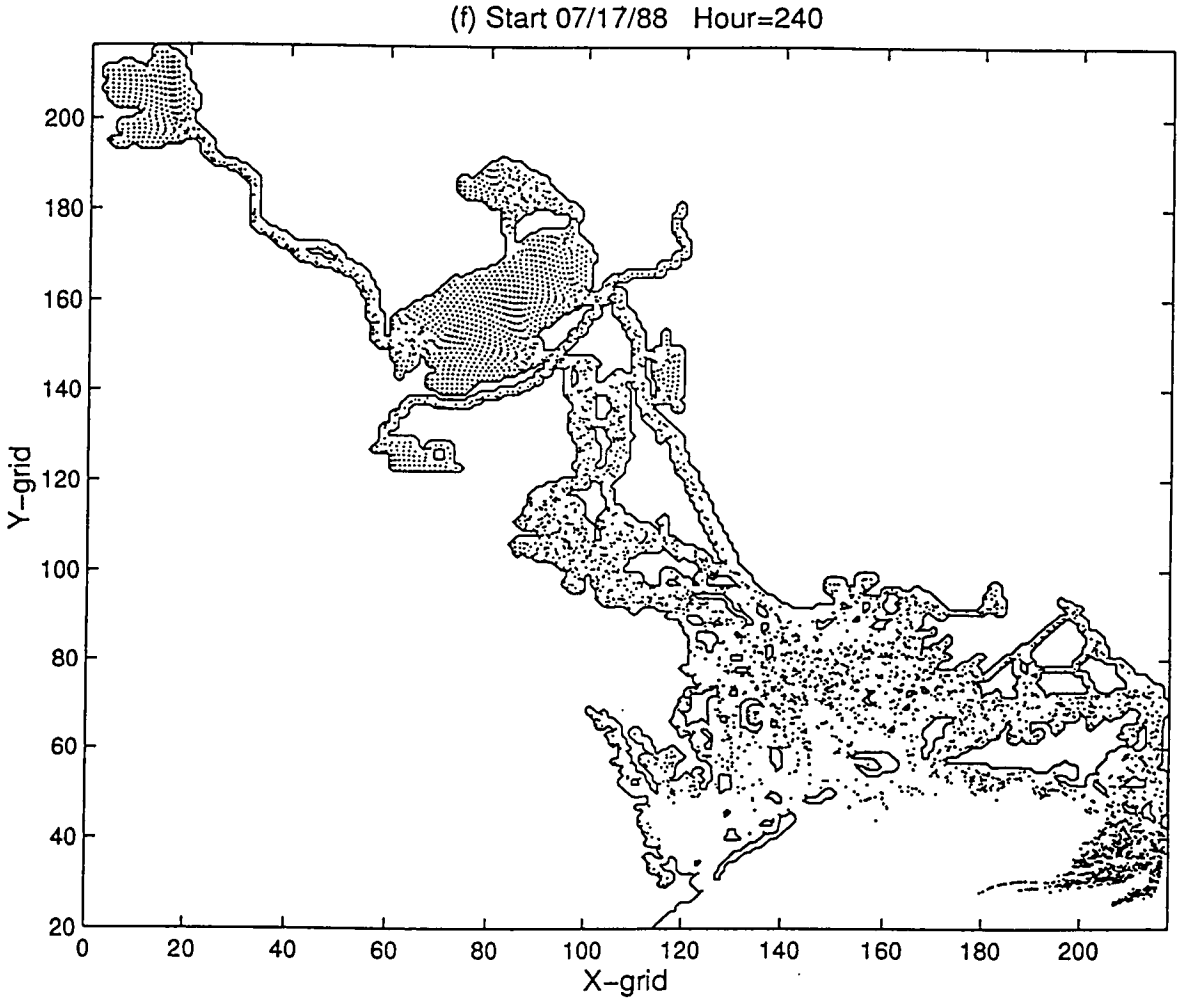

Figure 28f. Distribution of tracer particles simulated for the period 07/17/88-07/27/88 in Barataria Basin. After 240 hours.

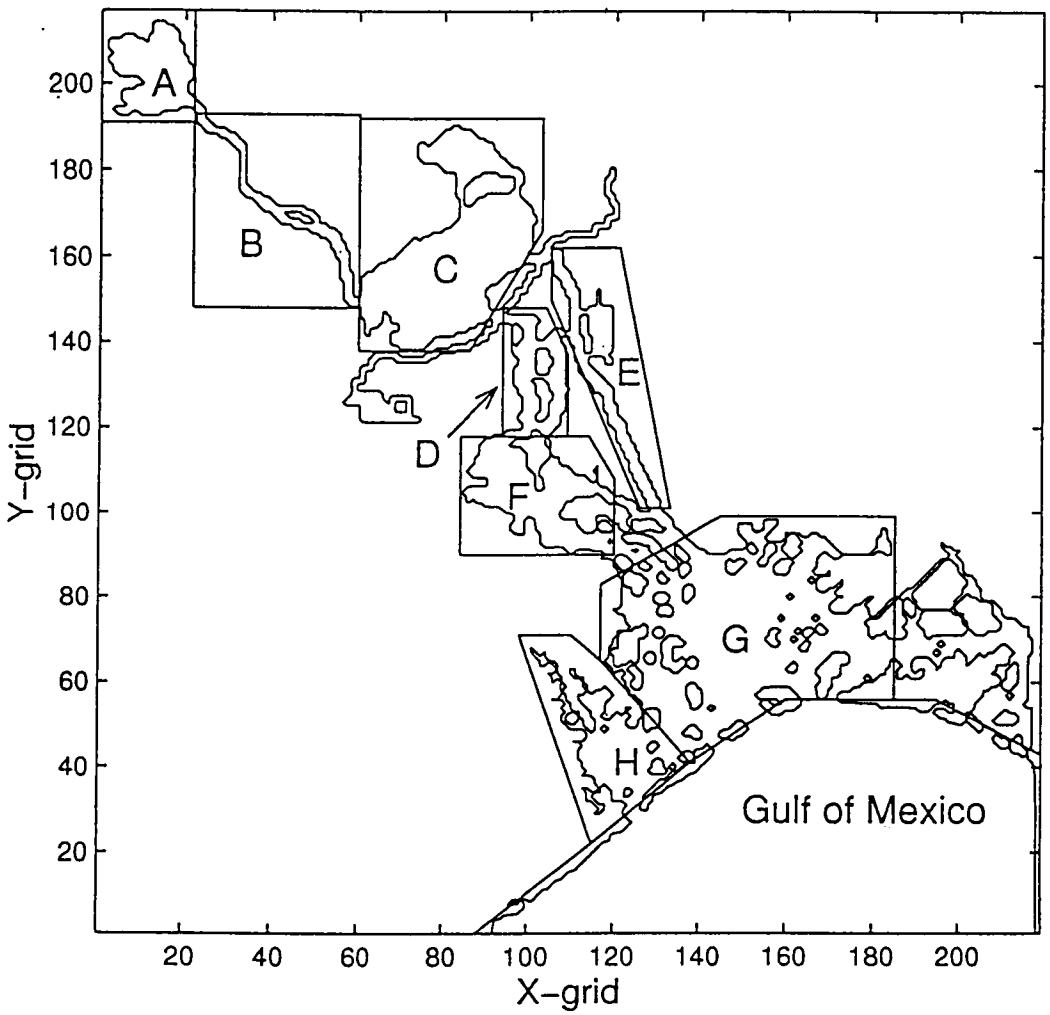

Figure 29. Eight sub-basins in Barataria Basin used for estimating flushing time.

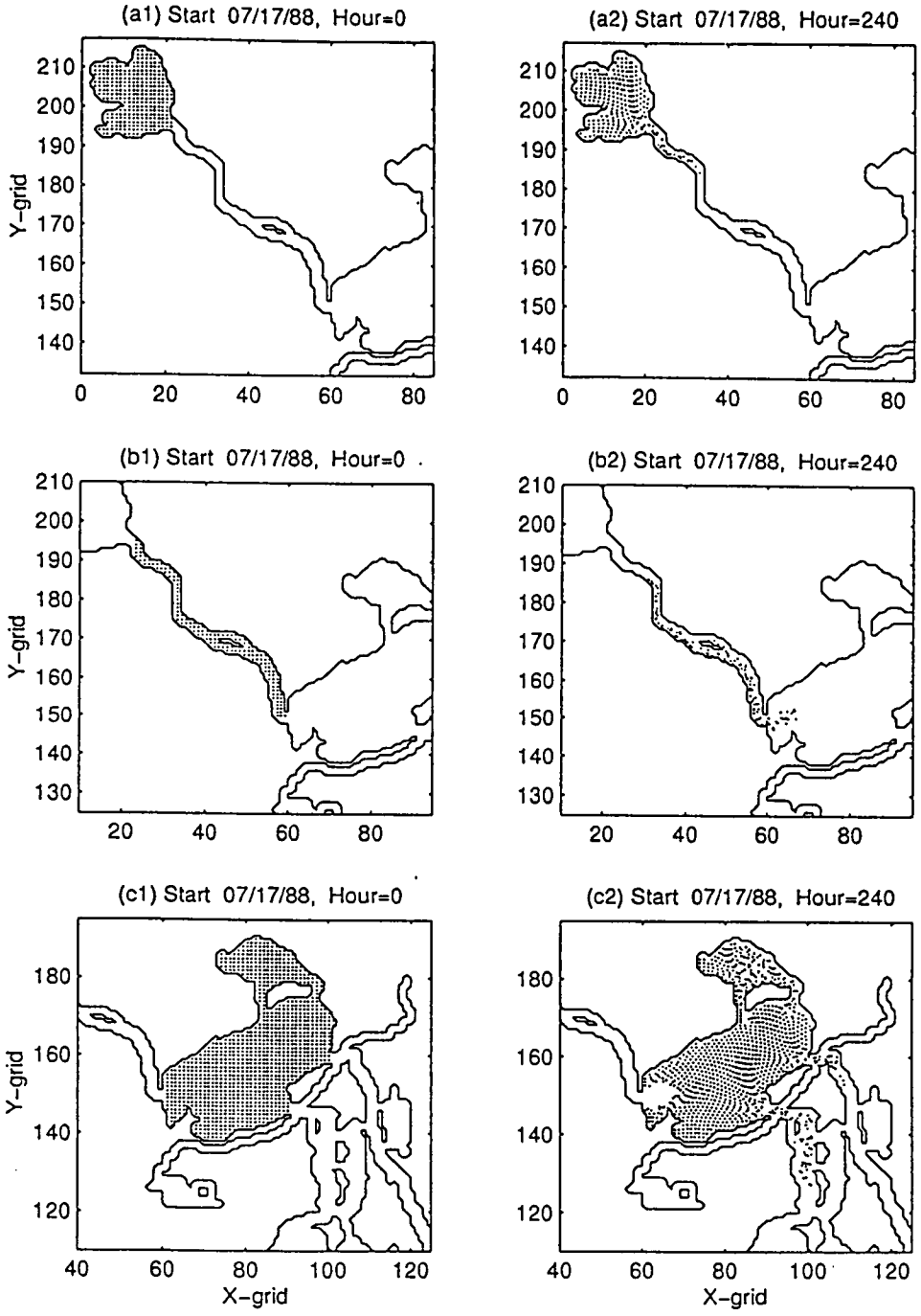

Figure 30a. Distribution of tracer particles in Sub-basins A, B and C in Barataria Basin for the period 07/17/88-07/27/88. At time of release (0 hr 07/17/88) (Left figure). After 240 hours (Right figure).

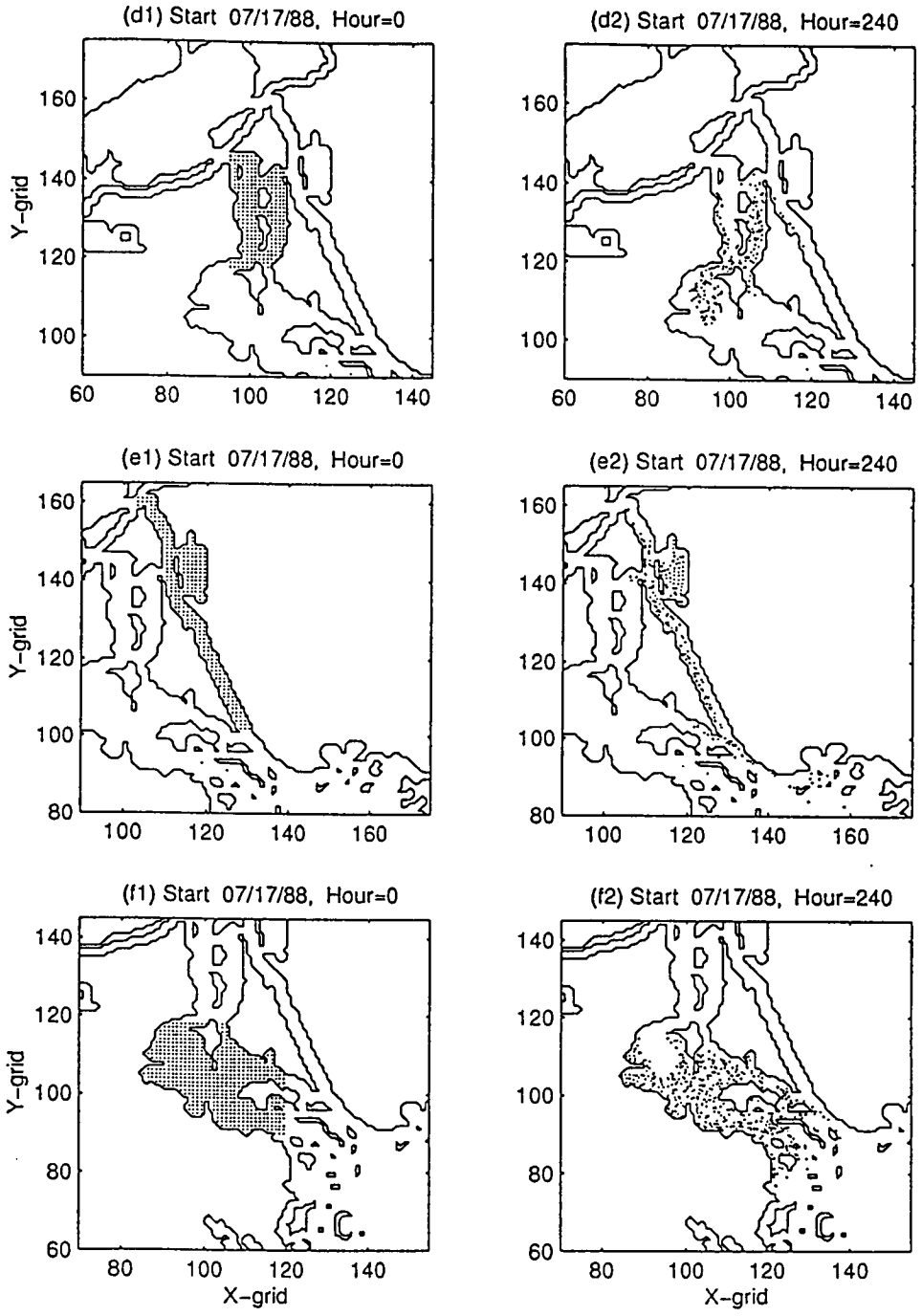

Figure 30b. Distribution of tracer particles in Sub-basins D, E and F in Barataria Basin for the period 07/17/88-07/27/88. At time of release (0 hr 07/17/88) (Left figure). After 240 hours (Right figure).

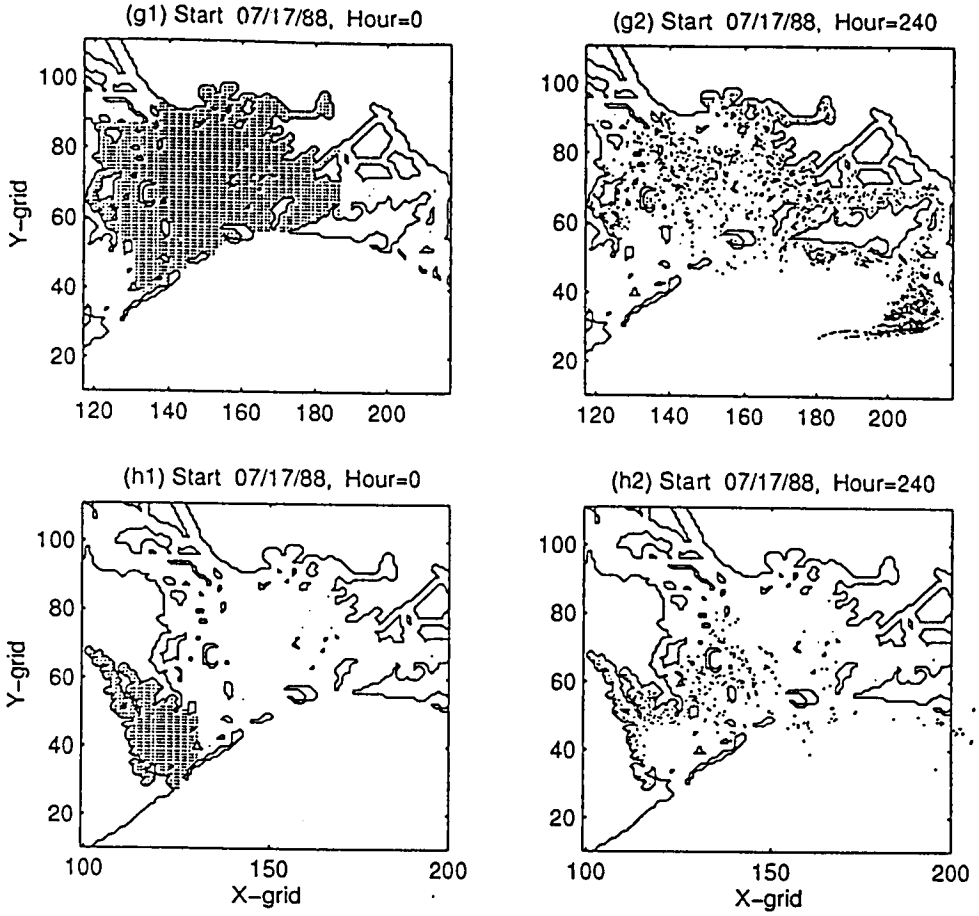

Figure 30c. Distribution of tracer particles in Sub-basins G and H in Barataria Basin for the period 07/17/88-07/27/88. At time of release (0 hr 07/17/88) (Left figure). After 240 hours (Right figure).

flushing time for each of the eight sub-basins is listed in Table 3. Downstream of Lake Salvador, flushing is relatively quick with flushing time ranging from 9 days to 20 days. Further upstream, it increases significantly, and in Lake Salvador flushing time is 38 days. These observations are consistent with previous tidal prism model results (Wiseman and Swenson, 1989).

3.5 Particle Dispersion

Tracking of tracer particles also yields information on particle dispersion due to the deformation of the flow field. For clusters of tracer particles, the variances of the particle positions σ_X^2 and σ_Y^2 along the major and minor axes of the cluster ellipse can be estimated. For this experiment, a cluster of tracer particles comprising of 49 particles initially located near the center of each of four sub-basins, namely Caminada Bay, Barataria Bay, Little Lake, and Lake Salvador, is used to estimate dispersion. Time evolution of each particle cluster is depicted in Figures 31 - 34. The spreading of each cluster, measured by the time evolution of $\sigma_X\sigma_Y$, is plotted in Figure 35. Significant variations are found in spreading rates of clusters. Spreading of clusters starts out slow in Little Lake, Lake Salvador, and Barataria Bay, while in Caminada Bay, it starts out relatively fast, and remains fast. Spreading of clusters in the upstream regions, namely Little Lake and Lake Salvador, remains slow throughout the experiment, while it undergoes a rapid increase in Barataria Bay during the second half of the experiment. It is interesting to note that the clusters released in Little Lake and Lake Salvador do not show, even after ten simulation days, a sign of significant coastal topographic trapping. The cluster released in Caminada Bay started to display a sign of significant coastal topographic trapping 48 hours after the release. A similar transition does not take place for the cluster released in Barataria Bay until the beginning of the second half of the experiment. It appears that as long as the cluster stays close together and unaffected by coastal topographic trapping, spreading rate of the cluster is controlled by the spatial and temporal variability of the flow fields. However, once coastal topographic trapping becomes dominant in deforming the particle cluster, spreading rate increases dramatically.

Figure 36 shows the estimated diffusion coefficients for each of the four sub-basins in comparison to the diffusion diagram prepared by Okubo (1974). All the values estimated are well within the scatter of Okubo's data. It is interesting that values estimated for Lake Salvador and Little Lake are closer to the lower bound of Okubo's data, while those for Caminada Bay and Barataria Bay are closer to the upper bound of Okubo's data. Obviously, coastal topographic trapping enhances spreading significantly. In the absence of coastal topographic trapping, the rate of spreading measured by diffusion coefficients tends to be closer to the lower bound of Okubo's data.

3.6 Summary and Conclusions

Circulation and transport processes in Barataria Basin were examined by applying a depth-integrated two-dimensional hydrodynamic model. Model calibration using the sea level height measured at several stations within the basin yielded a Manning's coefficient of 0.04, a value

Table 3

Estimated flushing time in eight sub-basins.

Area	Flushing Time (days)
A	38.10
B	22.40
C	38.50
D	12.80
E	20.40
F	15.00
G	12.30
H	9.00

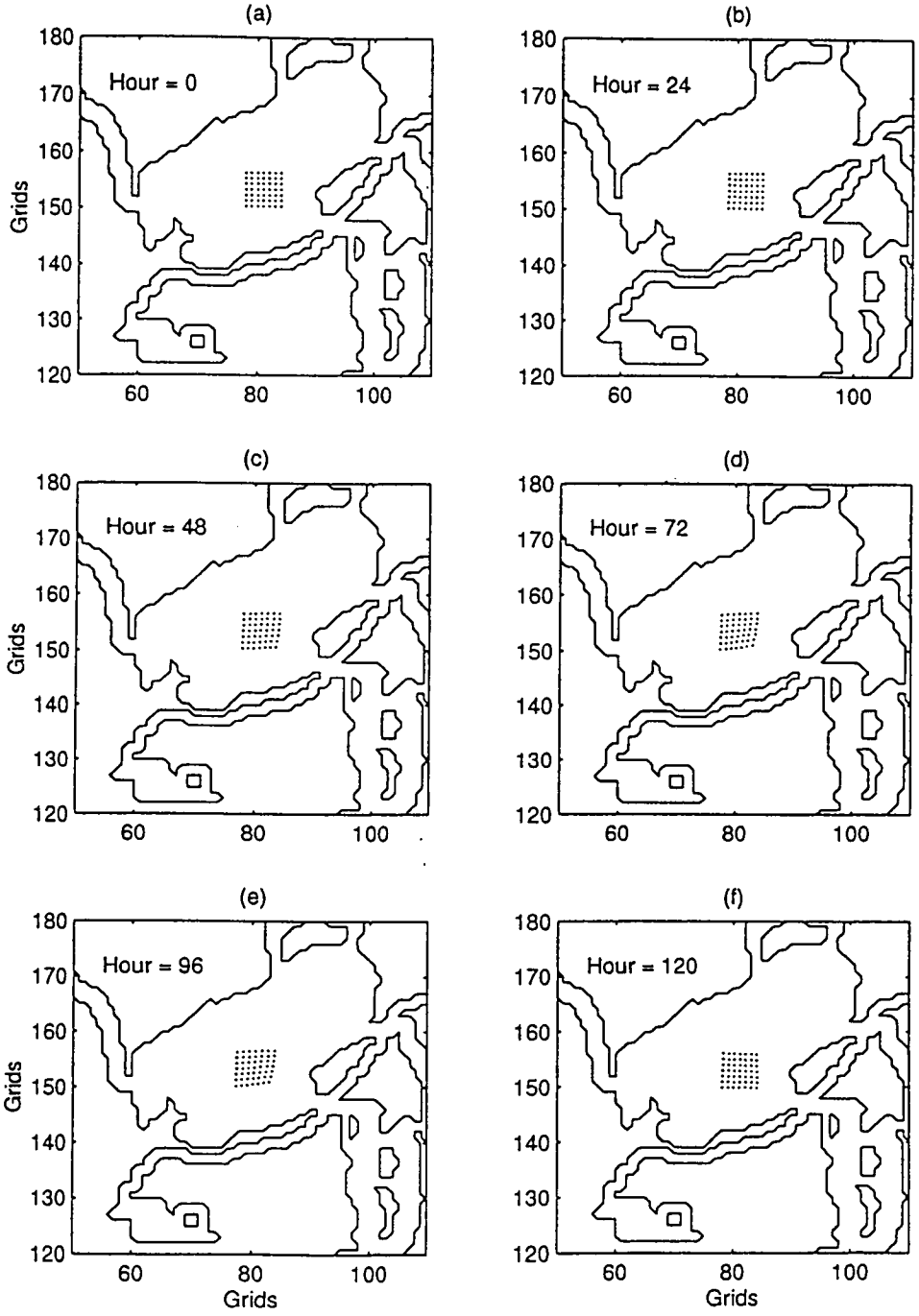

Figure 31. A cluster of 49 tracer particles released at Lake Salvador. (a) At time of release (0 hr 07/17/88). (b) After 24 hours. (c) After 48 hours. (d) After 72 hours. (e) After 96 hours. (f) After 120 hours.

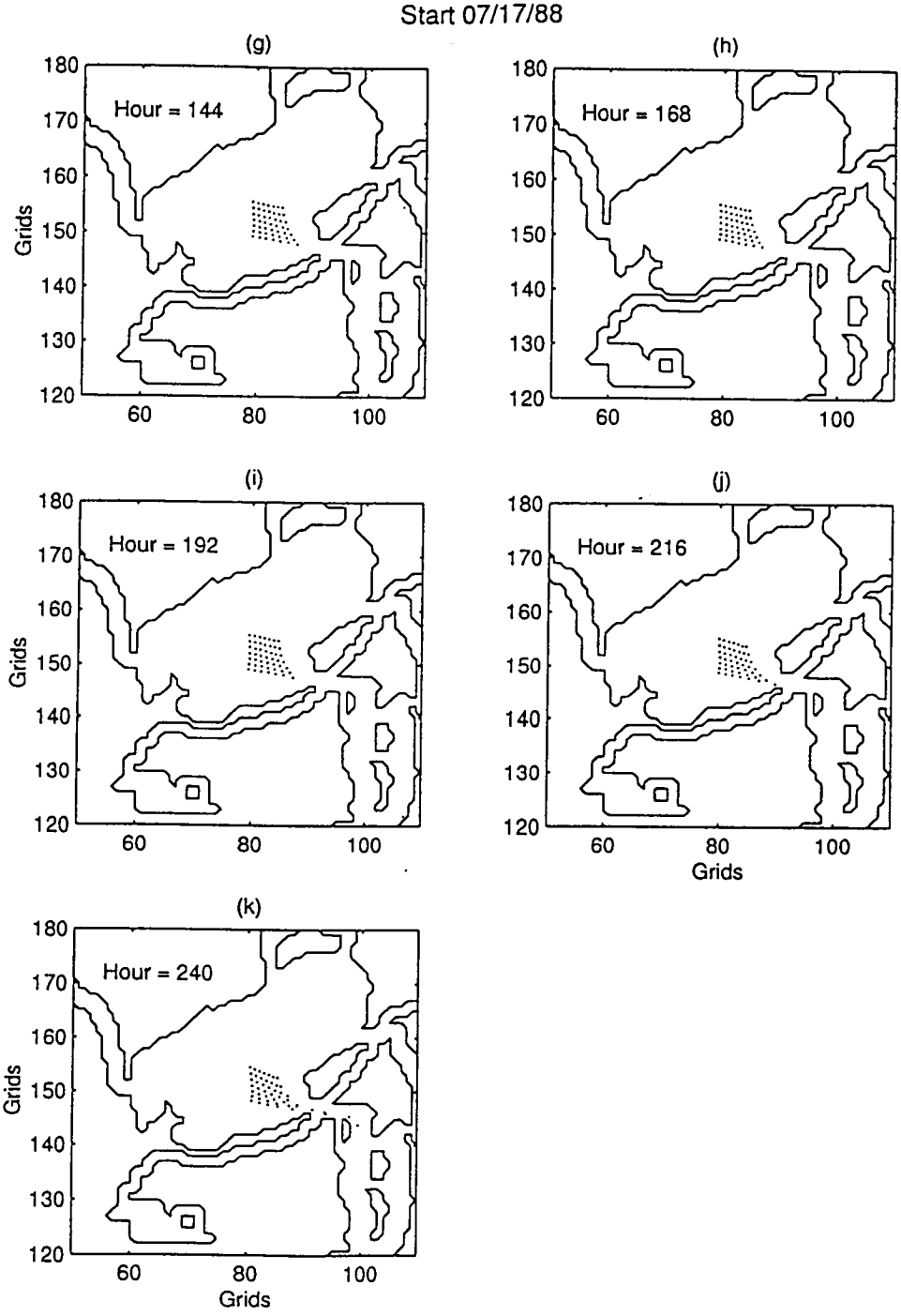

Figure 31. A cluster of 49 tracer particles released at Lake Salvador. (g) After 144 hours. (h) After 168 hours. (i) After 192 hours. (j) After 216 hours. (k) After 240 hours.

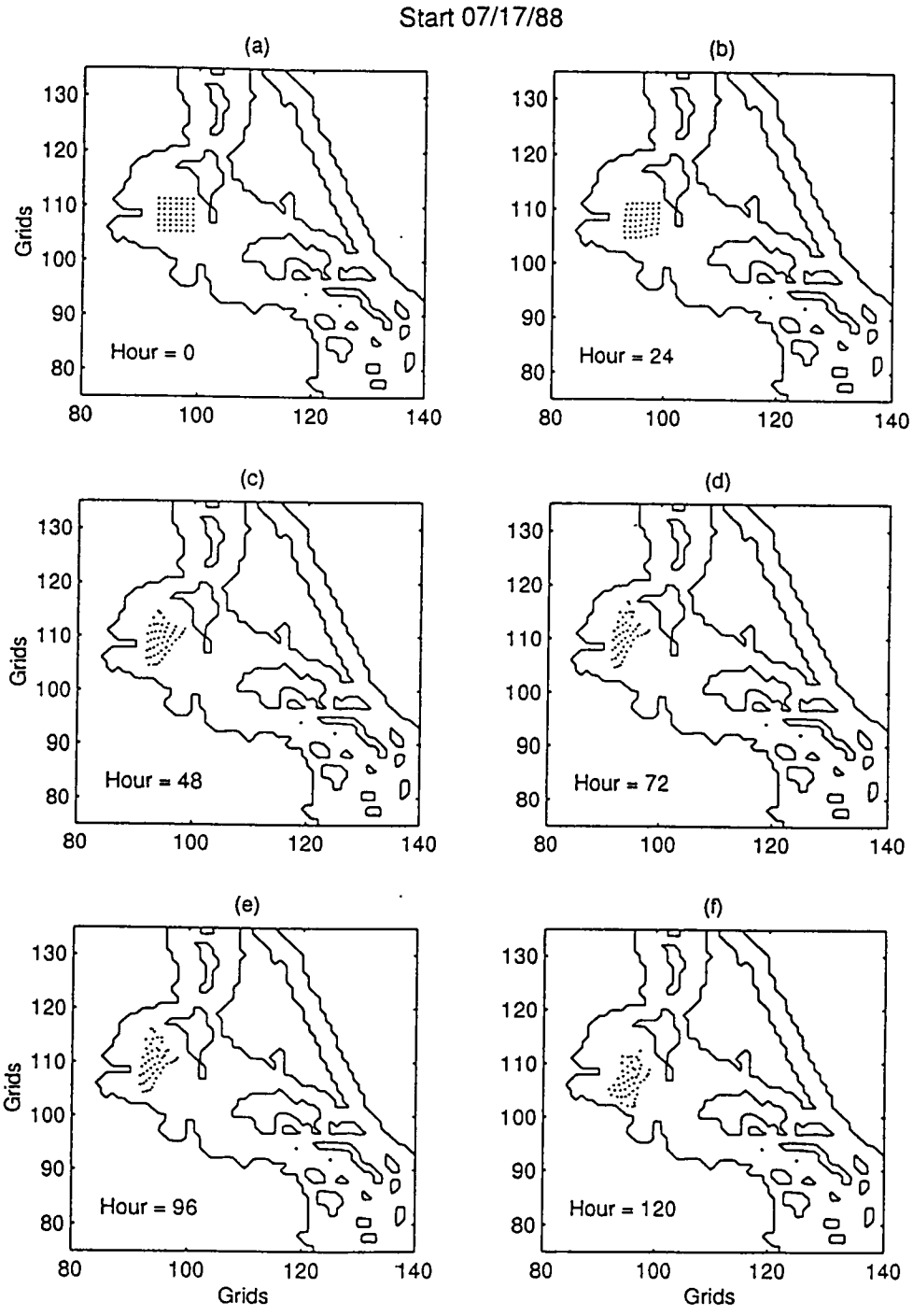

Figure 32. A cluster of 49 tracer particles released at Little Lake. (a) At time of release (0 hr 07/17/88). (b) After 24 hours. (c) After 48 hours. (d) After 72 hours. (e) After 96 hours. (f) After 120 hours.

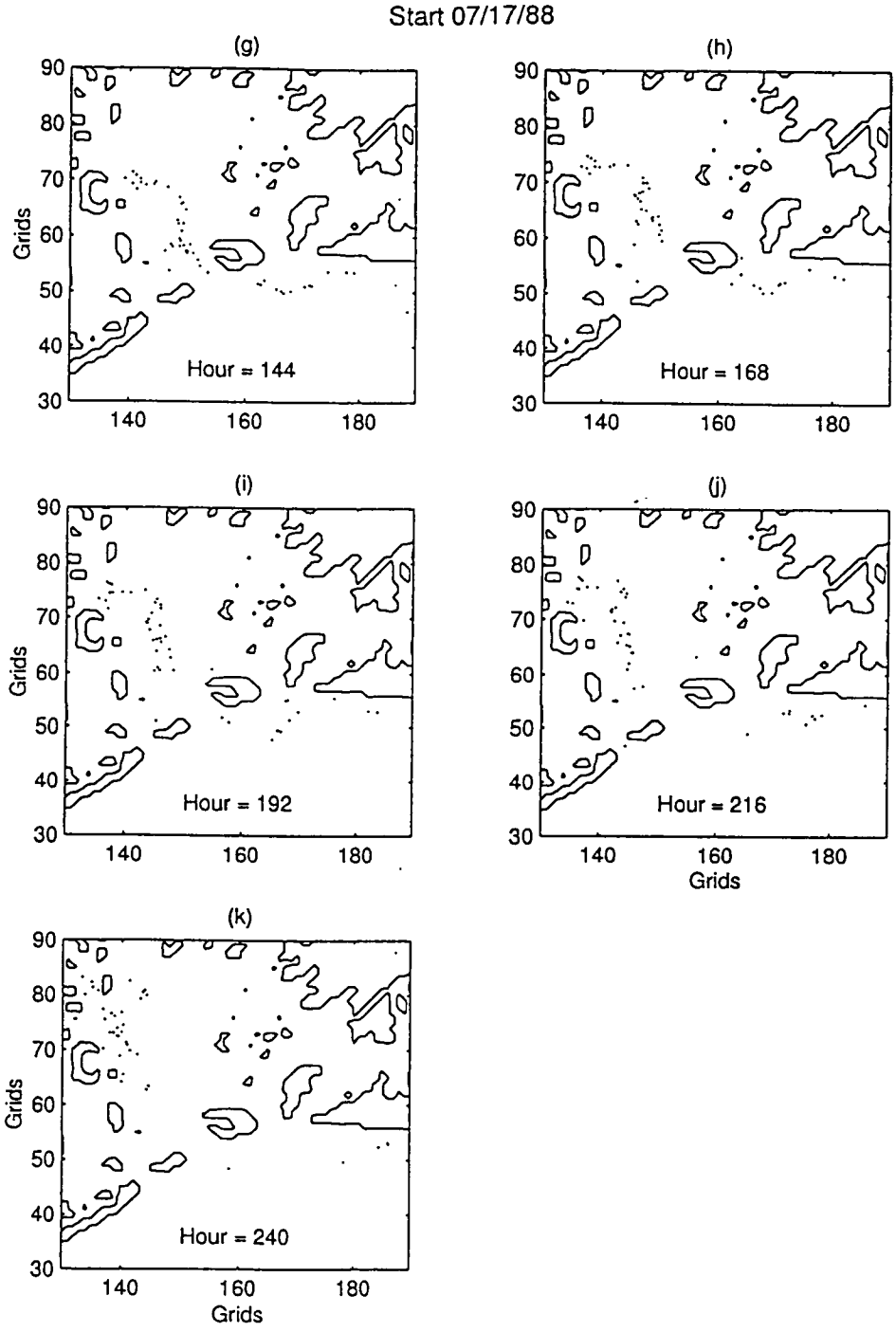

Figure 33. A cluster of 49 tracer particles released at Barataria Bay. (g) After 144 hours. (h) After 168 hours. (i) After 192 hours. (j) After 216 hours. (k) After 240 hours.

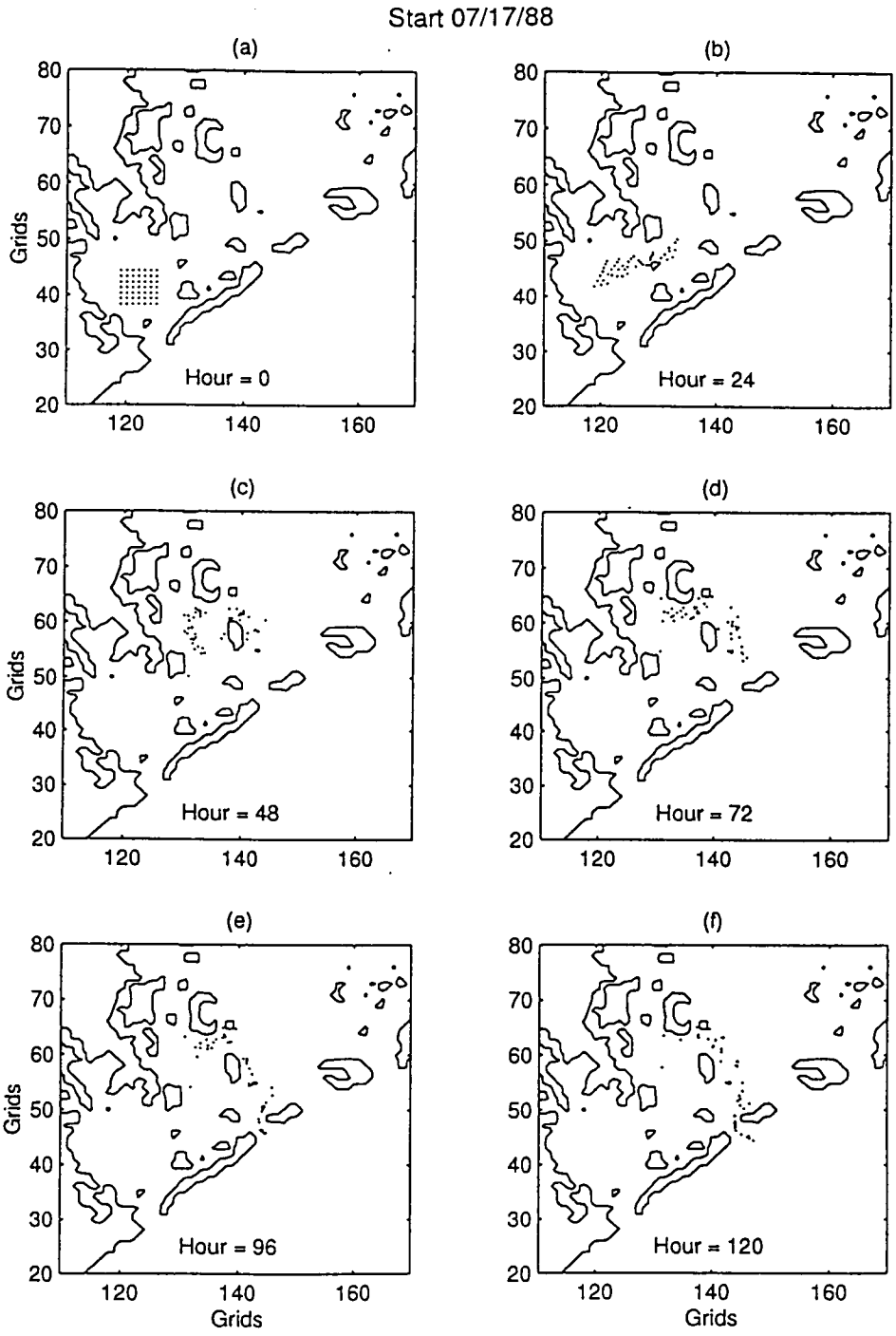

Figure 34. A cluster of 49 tracer particles released at Caminada Bay. (a) At time of release (0 hr 07/17/88). (b) After 24 hours. (c) After 48 hours. (d) After 72 hours. (e) After 96 hours. (f) After 120 hours.

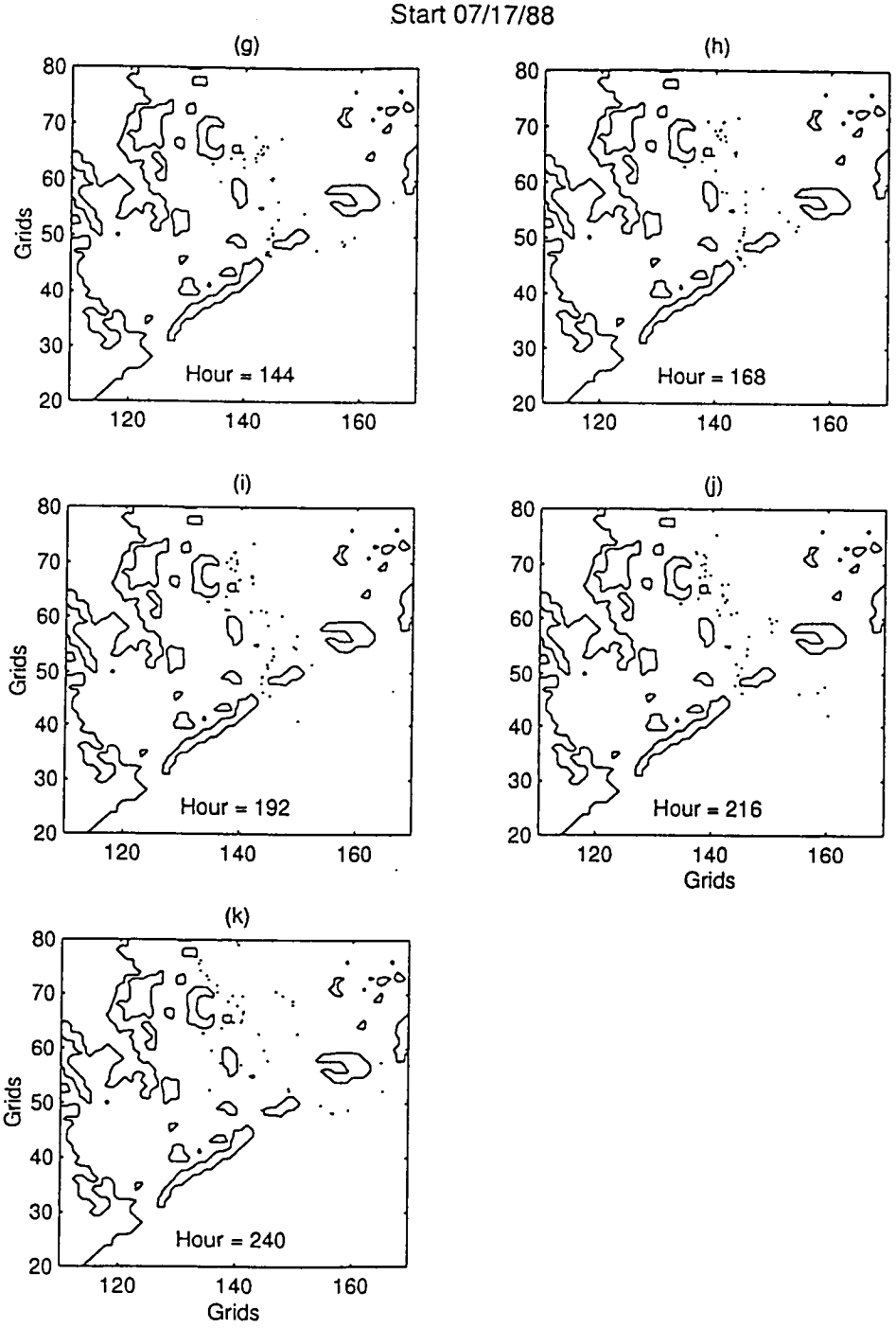

Figure 34. A cluster of 49 tracer particles released at Caminada Bay. (g) After 144 hours. (h) After 168 hours. (i) After 192 hours. (j) After 216 hours. (k) After 240 hours.

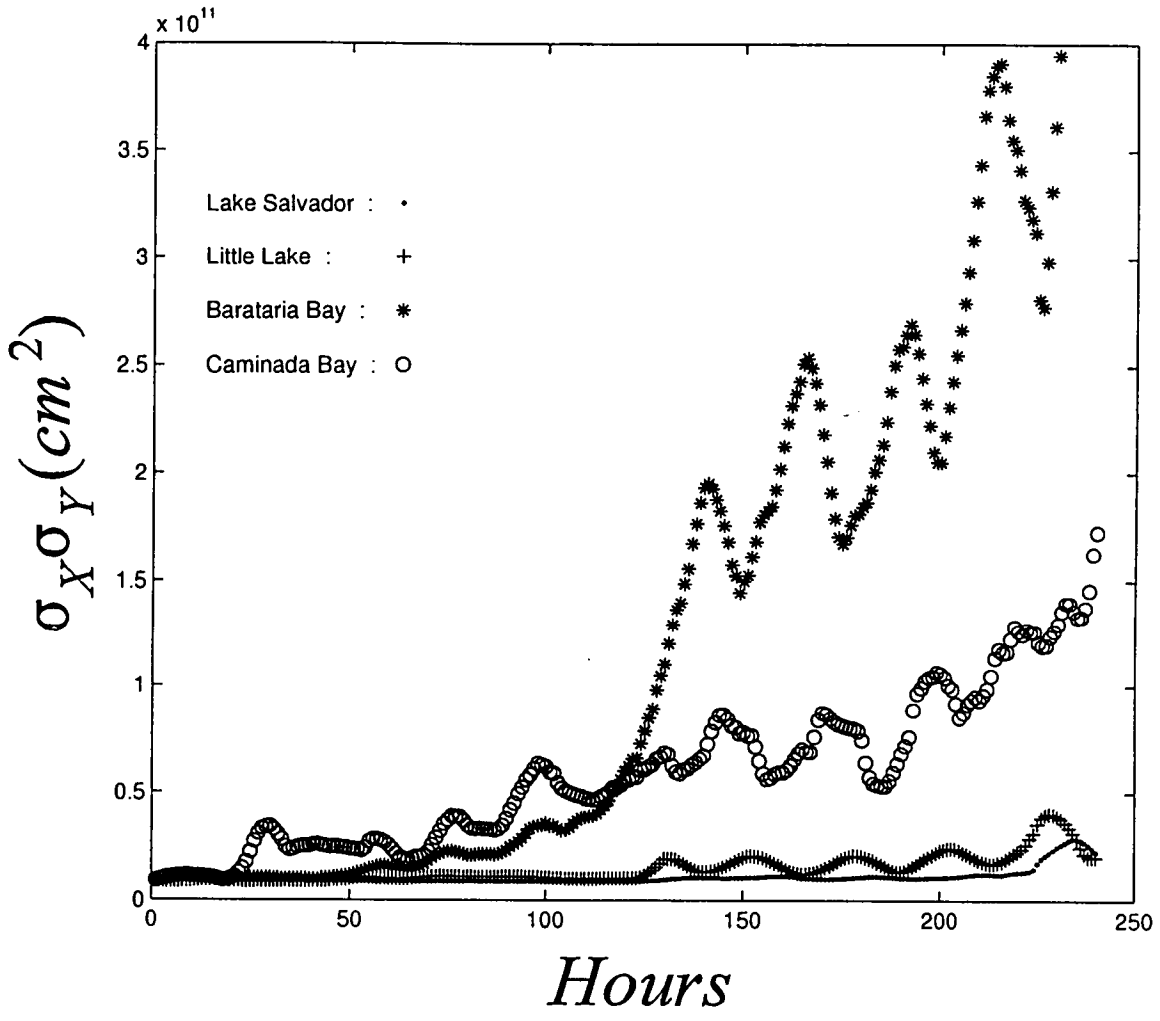

Figure 35. Variance, $\sigma_X\sigma_Y$, versus time for the particle clusters released in four areas shown in Figures 31 through 34.

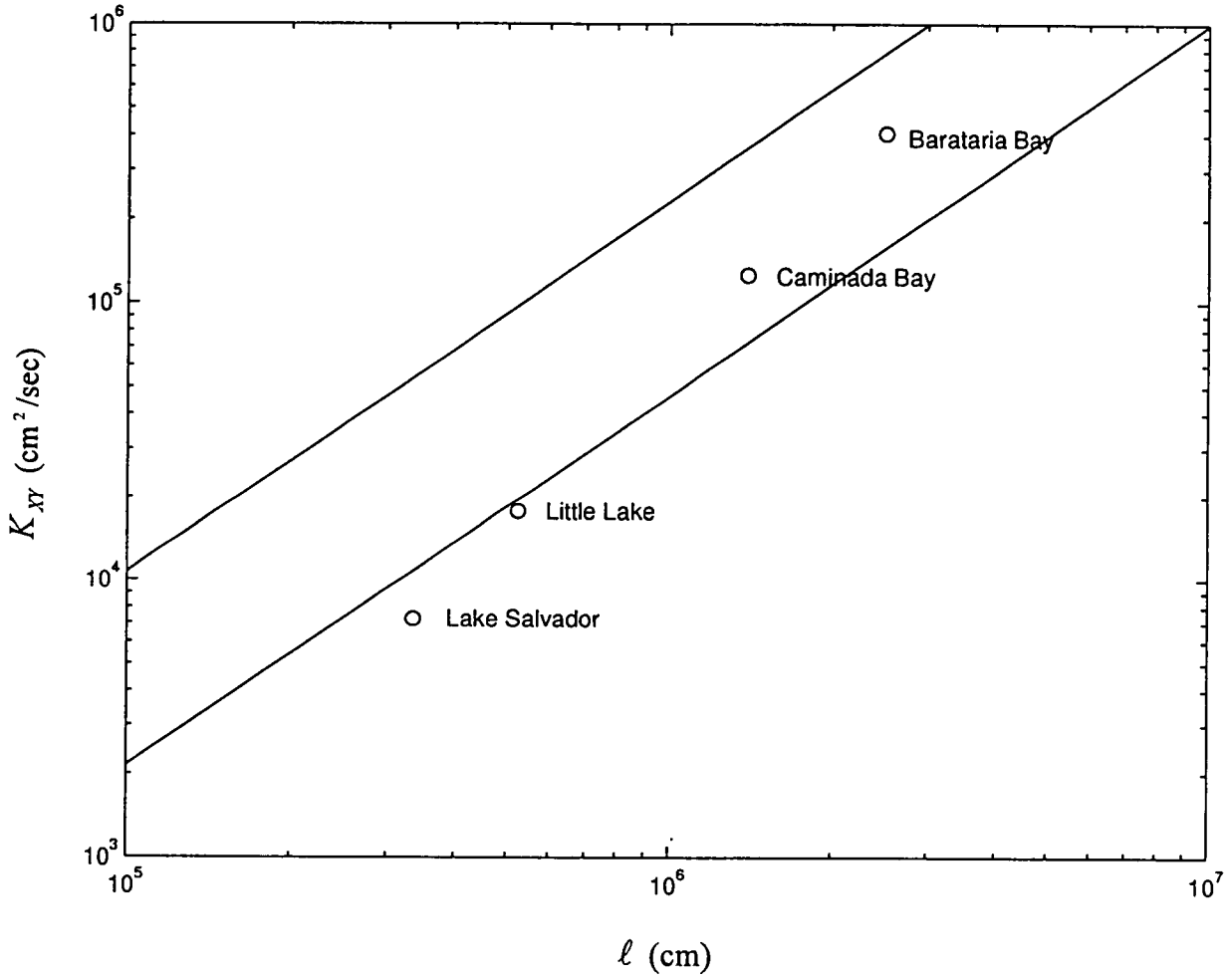

Figure 36. Horizontal diffusitivities (cm^2/sec) of clusters of 49 particles released at various locations (Lake Salvador, Little Lake, Barataria Bay and Caminada Bay) versus scale of diffusion, $l = 3\sqrt{2\sigma_X\sigma_Y}$ (Okubo, 1971). Range of Okubo's data (1974) is bounded by the two solid lines, $K_{XY} = 0.01\left(\frac{l^2}{9}\right)^{2/3}$ and $K_{XY} = 0.002\left(\frac{l^2}{9}\right)^{2/3}$ (Fischer et al., 1979).

smaller than what was obtained for Terrebonne/Timbalier Basin. The relatively large bottom friction estimated for both Terrebonne/Timbalier and Barataria Basin appears to be due to a combined effect of currents and the surface wave field which was not explicitly accounted for in the model. Effects of tidal forcing dominate flood and ebb currents inside the basin, while the local wind significantly influences the lateral component of bay circulation. The magnitudes of tidal currents which could develop inside the bay and in tidal passes are similar to those estimated for Terrebonne/Timbalier Basin.

Flushing time, estimated using a particle tracer technique, ranges from 12 days in Barataria Bay proper to 15 days in Little Lake. It increases significantly as you go further upstream reaching 38 days in Lake Salvador. Compared to Terrebonne/ Timbalier Basin, flushing time is comparable in Barataria Bay proper, while upstream regions have longer flushing time scales. This is reasonable in light of the observation that the main Barataria Basin has connectivity to the open Gulf which is similar to that of Terrebonne/Timbalier Basin, while the region further upstream has a limited connectivity via narrow waterways and channels.

Diffusion characteristics, estimated based on the spreading of tracer particle clusters, reveal diffusion coefficients comparable to Okubo's data. When the length scales of the cluster remain relatively small and the spreading is dominated by a spatially and temporally varying current velocity field, the resulting diffusion coefficient remains closer to the lower bound of Okubo's data. Once the size of the cluster gets large and the diffusion becomes dominated by coastal topographic trapping, the resulting diffusion coefficients move closer to the upper bound of Okubo's data.

Future improvements to the model should include 1) explicit representation of the combined effect of currents and the wave field, 2) more accurate representation of the many narrow waterways and channels, and 3) incorporation of drying/flooding of the surrounding wetlands.

CHAPTER 4

COUPLED HYDRODYNAMIC-ECOLOGICAL MODEL

4.1 Background

Fourleague Bay (Figures 1, 37 and 38) has been the focus of intense scientific study in the past because of its ecological importance to coastal Louisiana. It is a highly productive estuary which serves as a breeding ground and nursery for juvenile faunal species, both commercial and recreational; as a source of food within the estuary, as well as for the nearshore coastal zone; and as an invaluable scientific research site. Furthermore, the Atchafalaya region is the only area along the Louisiana coast experiencing new delta formation and marsh accretion.

Fourleague Bay is located just southeast of the Atchafalaya River mouth and is surrounded by extensive wetlands. With mean depth of 1.5 m, Fourleague Bay is shallow, highly turbid, and vertically well mixed. Freshwater discharge from the Atchafalaya River, which presently carries approximately one third of the total Mississippi River discharge, together with its large suspended sediment and nutrient loads, significantly impacts Fourleague Bay. Salinity ranges from 0~8 ppt in the Upper Bay and 0~26 ppt in the Lower Bay (Caffrey and Day, 1986). Estimated residence time of water within Fourleague Bay varies from 7 days during the spring peak discharge of the Atchafalaya River to about 65 days during low river discharge periods (Day et al., 1995). During the spring peak discharge period, approximately 2% of the Atchafalaya River discharge enters Fourleague bay through the upper entrance (Denes, 1983). Suspended sediment load of this water ranges from 150 mg l^{-1} in the summer to 450 mg l^{-1} during the spring peak discharge period (USGS Water Resources Data 1985-1992). High concentrations of nitrate (NO_3), nitrite (NO_2), and ammonium (NH_4) are also present. The total inorganic nitrogen (TIN) load in the river varies from around 50 μM in fall and winter to over 100 μM in spring (USGS Water Resources Data 1985-1992). Consequently, the inputs of nitrogen and suspended sediments to the bay have profound ecological impacts.

During the spring flood, the bottom sediments and adjacent marshes respond to the increased input of nutrients by acting as a buffer and storing excessive amounts of nutrients while they are plentiful (Teague, 1983; Childers and Day, 1990). During the low river flow periods, less nutrients are available and the marshes and bottom sediments release into the water column, the nutrients, which are utilized by phytoplankton (Teague, 1983). This is one mechanism which leads to a highly productive system with primary production rates on the order of 0.88 g C m^{-2} day^{-1} in the winter/spring (December-May) and 2.31 g C m^{-2} day^{-1} in the summer/fall (June-November) (Madden, 1992). On an annual basis, the production is greater in the lower bay (317 g C m^{-2} day^{-1}) than in the upper bay (120 g C m^{-2} day^{-1}) (Randall and Day, 1987).

The lower production in the winter months is likely due to light limitation of phytoplankton (Madden and Day, 1992). This is caused by the high sediment concentrations in the bay associated with high rates of wind-driven bottom resuspension (Caffrey, 1983) and Atchafalaya River water. As an indication of the degree of turbidity in Fourleague Bay,

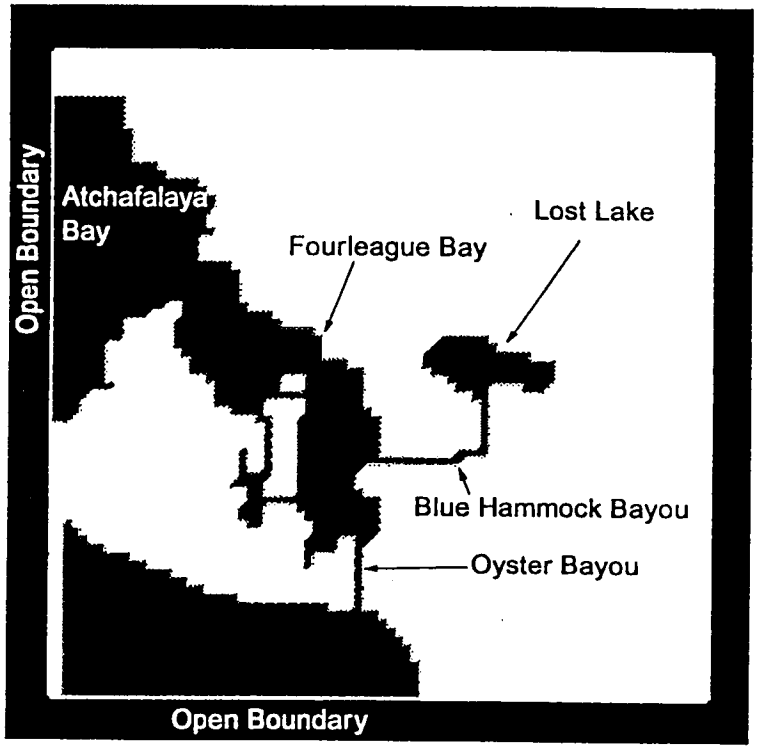

Figure 37. Model geometry of the Fourleague Bay Model. The southern and the western boundaries are open.

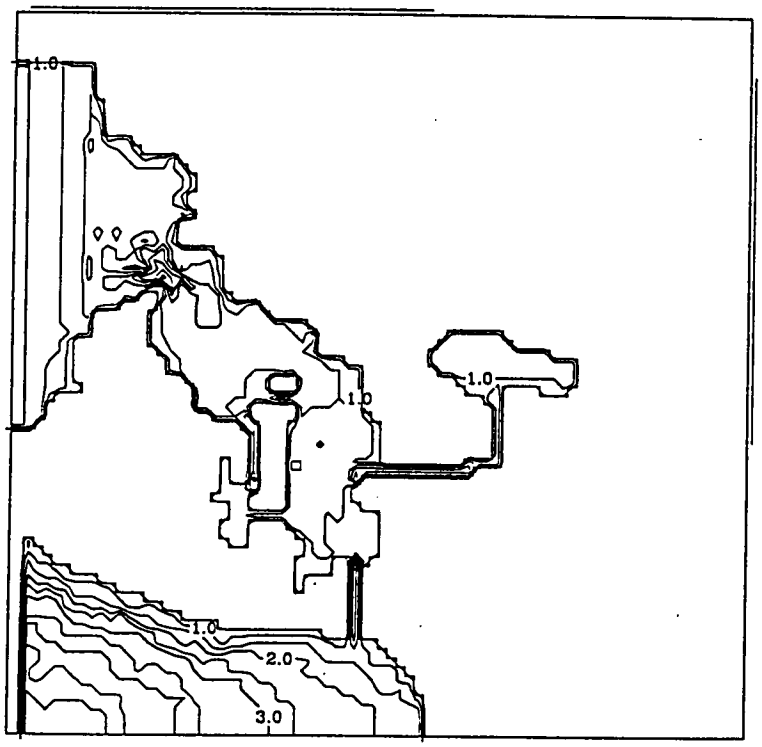

Figure 38. Model bathymetry of the Fourleague Bay Model. Bottom bathymetric contours are shown at every 0.5 m.

Madden (1992) reported that the average euphotic zone, the average depth of 1% light, is only 0.7 m with an average light attenuation coefficient (k) of 4.4 m^{-1} and maximum k often exceeding 20 m^{-1}. Additionally, total suspended sediment concentrations of 152 mg l^{-1} have been recorded in Oyster Bayou during March 1994 (Day unpublished data). In the summer and fall the riverine inputs are reduced and the winds have dissipated and shifted to the south. This results in greater production due to an increase in light levels coupled with an abundance of available nutrients as well as increased sea surface temperatures.

Recently, an initial attempt was made to incorporate an ecological model into the two-dimensional depth-integrated hydrodynamic model developed at the Coastal Studies Institute (Inoue et al., 1996). In this chapter, detailed model formulation of this coupled hydrodynamic-ecological model is presented for the first time. An example of a simulation run using the coupled model is presented in order to illustrate the model's response to a typical spring condition.

4.2 Model Formulation

The set of equations used in the ecological module of the model code were initially tested in a single box ecological model developed by Dr. Dubravko Justic using the Runge-Kutta method for time integration (Inoue et al., 1996). This technique obtains fourth order accuracy by integrating the derivative four times every time step of 1 hour. The ecological module incorporates three state variables which are crucial to the ecological system of the bay. Those state variables are: total suspended sediments (TSS), total inorganic nitrogen (TIN), and phytoplankton as chlorophyll a. The direct forcing functions in the ecological component include Atchafalaya River discharge, light, and temperature. All nutrient interactions follow the Redfield ratio model. Most of the important empirical relationships used in the ecological model were derived from the field data collected recently (Inoue et al., 1996) and during various field programs carried out under the direction of Dr. John Day over the past 15 years.

Sediment Balance

There are two variables involved in the sediment balance in the model. The first is the amount of total suspended sediments that enter Fourleague Bay from the Atchafalaya River. This is expressed as TSSIN in mg l^{-1} hr^{-1}. The TSS concentration in the river is set at 359 mg l^{-1}, which corresponds to a typical January condition (USGS Water Resources data 1985-1989). The second variable is the sedimentation rate of TSS in the system, which is set to 35% day^{-1}.

Nutrient Balance

Nutrient concentrations in Fourleague Bay, expressed as TIN, are balanced by four variables. The first is the amount of nitrogen that enters Fourleague Bay from the Atchafalaya River. The TIN concentration in the river water is set at 114 μM (Justic, unpublished data). Throughout the bay, nutrients are constantly being taken up by phytoplankton. This nutrient uptake (NUPT), a loss term, is a function of GROWTH and the phytoplankton stock. Since phytoplankton is expressed in terms of chlorophyll a, a conversion factor must be used to convert

to nitrogen. Chlorophyll is first converted to carbon using a C:Chl a ratio of 30:1 found in Redalje et al. (1994) and Kremer and Nixon (1978). Carbon is then converted to nitrogen using the Redfield ratio model. The C:N ratio, by weight, is 4C:7N, or 5.7. This concentration is then divided by the atomic weight of nitrogen to obtain units of μM. Finally, nitrogen remineralization in the water column, an additive term, is included. NREG is the TIN remineralization rate moderated by zooplankton grazing. NREG is set to 50% of the phytoplankton stock grazed by zooplankton. NREG is also converted to nitrogen.

Nutrient limitation in Fourleague Bay is not common because of the high influx of nutrients from the Atchafalaya River. Our model incorporates nutrient limitation, NUTLIM, as a potential limitation of total inorganic nitrogen (nitrate+nitrite+ammonium). The NUTLIM parameter is based on the Michaelis-Menton relationship, normalized to maximum phytoplankton growth which takes the form:

$$NUTLIM = N/(K_s + N)$$

where N is the concentration of nitrogen present, and K_S is the half-saturation constant. K_S is the concentration of nitrogen at which uptake is one half of the maximum uptake rate. The K_S value is assumed to be 1 μM of nitrogen. This value is within those reported for uptake by marine phytoplankton (Eppley et al., 1969) and is the value reported for Narragansett Bay (Kremer and Nixon, 1978).

Light

Light attenuation in the water column is caused by reflection, refraction, scattering, and absorption by sea water itself and dissolved and particulate matter in the water. The light attenuation in the water column is expressed by the light attenuation coefficient, KD (m^{-1}). KD is generated based on the relationship between measured values of KD and TSS in the field by Madden (1992). This KD value is used in the Beer-Lambert expression to determine the distribution of light with depth in the water column. The light intensity, I_Z , at depth Z, is expressed as:

$$I_z = RADN \times \exp^{-KD \times Z}$$

where $RADN$ is the solar radiation reaching the sea surface. A characteristic depth of 0.25 m is chosen for Z, based on the assumption that sufficient mixing is present to allow the phytoplankton to reach the upper 0.25 m of the water column.

Due to the shallow depths of Fourleague Bay (1.5 m mean depth) and the high levels of turbidity, the system is often light limited for phytoplankton (Madden and Day, 1992).

Phytoplankton Production

GMAX is the maximum phytoplankton growth rate parameter and is an exponential function of temperature. GMAX is expressed in divisions per day. Our calculations assume a growth rate of phytoplankton at 30°C of 3 day^{-1}. This is close to the growth rate of 2.6 day^{-1} reported by Eppley (1972). The actual growth rate, GROWTH, is a function of GMAX, LTLIM, and NUTLIM, where LTLIM is the relative light limitation of phytoplankton, and NUTLIM is the nutrient limitation of phytoplankton.

4.3 Model Equations

Equations describing the ecological module are

$$\frac{\partial HS}{\partial t} + \frac{\partial US}{\partial x} + \frac{\partial VS}{\partial y} = D_S\left(\frac{\partial H\frac{\partial S}{\partial x}}{\partial x} + \frac{\partial H\frac{\partial S}{\partial y}}{\partial y}\right) + SLOSS$$

$$\frac{\partial HN}{\partial t} + \frac{\partial UN}{\partial x} + \frac{\partial VN}{\partial y} = D_N\left(\frac{\partial H\frac{\partial N}{\partial x}}{\partial x} + \frac{\partial H\frac{\partial N}{\partial y}}{\partial y}\right) - NUPT + NREG \qquad (4)$$

$$\frac{\partial HP}{\partial t} + \frac{\partial UP}{\partial x} + \frac{\partial VP}{\partial y} = D_P\left(\frac{\partial H\frac{\partial P}{\partial x}}{\partial x} + \frac{\partial H\frac{\partial P}{\partial y}}{\partial y}\right) + GROWTH - ZOOGRZ$$

where s, n and p are concentrations of suspended sediments, nutrients, and phytoplankton, respectively. $S = \frac{1}{H}\int_{-h}^{\zeta} s\,dz$, $N = \frac{1}{H}\int_{-h}^{\zeta} n\,dz$ and $P = \frac{1}{H}\int_{-h}^{\zeta} p\,dz$, D_S, D_N and D_P are the horizontal eddy diffusivities for S, N and P, respectively.

RADN = actual solar radiation reaching the sea surface = 450 (langleys), a typical value for May.

Iopt = optimum light level for phytoplankton productivity = 600 (langleys)

Kd = light attenuation coefficient (m^{-1}) = 1.42 + 0.00645 • S

S = total suspended sediment concentration (mg l^{-1})

Iz = light intensity at the depth of 0.25 m. = RADN • exp(-Kd • 0.25)

LTLIM = relative light limitation of phytoplankton = (Iz/Iopt) • exp(1-(Iz/Iopt))

NUTLIM = nutrient limitation of phytoplankton = N/(1.0 + N)

N = nitrogen concentration (μM)

SEATEMP = sea surface temperature (°C) = 20 for typical May conditions

GMAX = maximum phytoplankton growth rate (s^{-1}) = 0.5 • exp(0.06•SEATEMP)/86400

GROWTH = actual growth rate of phytoplankton = GMAX •LTLIM •NUTLIM

ZOOGRZ = instantaneous phytoplankton mortality due to zooplankton grazing (s^{-1})
= ZGRATE •P / (50.0 + P)

P = phytoplankton standing crop expressed as Chl a ($\mu g\ l^{-1}$)

ZGRATE = 1.2/86400

NUPT = TIN uptake by the phytoplankton = (GROWTH •P) •(CAC/(CF •14.0))

CAC = 30.0

CF = 5.7

NREG = TIN remineralization rate, which is moderated by the zooplankton grazing
= 0.5•(ZOOGRZ •P) •(CAC/(CF •14.0))

4.4 Model Simulation

The ecological module expressed in (4) is coupled to the two-dimensional depth-integrated hydrodynamic model expressed in (1). The hydrodynamic model for Fourleague Bay was previously developed and calibrated (Wiseman and Inoue, 1994). The model domain is based on the 1:80,000 scale nautical charts, and includes a portion of the open Gulf to the south with a model grid spacing of 463 m (Figures 37 and 38). The time step used is 10 s, the horizontal eddy viscosity and all the horizontal eddy diffusivities are taken as 10 $m^2\ s^{-1}$. The previous model calibration (Wiseman and Inoue, 1994) yielded a Manning's value of 0.1 for the Fourleague Bay Model. The model is forced by specifying time-dependent sea-level height along the southern and the western open boundaries based on the sea-level measurements taken at the Amerada-Hess platform located just outside the northwest open boundary of the model, and the time-dependent spatially uniform wind stress based on the wind speed measured at a platform located inside the Fourleague Bay (Hsu, 1992, personal communication). Conversion from wind speed to wind stress is done using the same empirical relationship used for the Terrebonne/Timbalier Basin Model which was originally derived for Fourleague Bay (Hsu, 1992, personal communication). Actual specification of sea-level height along the two open boundaries is done by simply using the observed sea-level heights at the Amerada-Hess platform without any

changes in amplitude and phase (Wiseman and Inoue, 1994).

It is well known that the large freshwater discharge from the Atchafalaya River, particularly during the spring flood, could result in a net sea-level slope difference between the Atchafalaya Bay and the Fourleague Bay, pushing water southward through the Fourleague Bay. This effect is incorporated in the model by specifying a net height difference in sea level between the western and the southern open boundaries. A series of calibration runs was made by varying the net sea-level height difference between the two open boundaries and estimating the resulting net throughflow in Oyster Bayou. A linear regression relationship between the net sea-level height difference and the throughflow in Oyster Bayou is derived and subsequently used to specify a net sea-level height difference for the model in order to obtain any desired throughflow in Oyster Bayou.

Under the model domain setup used here, the ecological module requires the specification of open boundary conditions for the three state variables. The assumptions adopted here include; 1) Fluxes of the three state variables across the open boundaries are limited to advective flux only, 2) Outflow across an open boundary carries the value of a state variable just inside the open boundary, 3) Inflow across an open boundary carries the value specified at the open boundary.

The objective of the "spring bloom" experiment carried out here is to simulate a spring bloom of phytoplankton in Fourleague Bay. For this experiment, the following open boundary conditions are used,

1) Net freshwater inflow from Atchafalaya River is close to 2% of the estimated river discharge from Atchafalaya River (5.6×10^8 m^3 day^{-1}) (This corresponds to a 0.13 m difference in sea-level height between the two open boundaries).

2) TSS concentration in the Atchafalaya River discharge (i. e., inflow along the western open boundary) is 359 mg l^{-1} .

3) TIN concentration in the Atchafalaya River discharge (i. e., inflow along the western boundary) is 114 μg at l^{-1} .

4) Phytoplankton concentration in the Atchafalaya River discharge (i. e., inflow along the western boundary) is 0 μg l^{-1} .

5) TSS, TIN, and phytoplankton concentrations in open Gulf of Mexico water (i. e., inflow along the southern open boundary) are all 0.

6) Initial conditions for TSS, TIN and phytoplankton concentration inside the model domain were set to be 50 mg l^{-1}, 70 μg at l^{-1}, and 20 μg l^{-1}, respectively. These are close to the typical values observed in Fourleague Bay during spring.

The model was forced by typical sea-level and wind conditions for Fourleague Bay and integrated for one month of simulation time. The three state variables at three locations, namely upper, mid, and lower bay, inside the Fourleague Bay for the first 30 days are plotted in Figures 39a through 39c. Figures 40a through 40c show snapshots of the variable field for the three state variables on Day 18. The suspended sediment concentration initially decreases inside the bay due to a 35% day^{-1} sedimentation rate. After the initial decrease, it begins to increase due to the advective influx of the highly turbid Atchafalaya River discharge into Fourleague Bay. The turbid river discharge first appears in the upper bay at Day 2, subsequently at Day 4 in the mid bay, and at Day 7 in the lower bay. It continues to increase until Day 19 when it reaches a peak. Thereafter, it appears to settle down toward values in the range 45~50 mg l^{-1} . The nitrogen concentration initially decreases with the most notable decrease in the lower bay due to the rapid growth of phytoplankton. More rapid growth of phytoplankton in the mid and lower bay is caused by the availability of more light at greater depths. Peaking of the phytoplankton standing stock is reached after several days with the most prominent peak appearing at Day 10 in the lower bay. This peaking appears to be due to the depletion of the available nitrogen by the "phytoplankton bloom." Subsequently, phytoplankton concentration decreases with a corresponding increase in nitrogen concentration. In the upper bay, due to the high concentrations of suspended sediments, "blooming" of phytoplankton never takes place, and nitrogen concentration shows only a slight decrease. On Day 4, the beginning of the gradual increase in nitrogen concentration signals the arrival of the nutrient-rich river discharge at the upper bay. Gradual decrease in phytoplankton concentration is accompanied by the gradual increase in nitrogen concentration. On Day 20, the whole system appears to settle down toward a quasi-steady state with nitrogen concentration in the range of 100~110 μg at l^{-1} in the upper bay, 80~100 μg at l^{-1} in the mid bay, and 60~80 μg at l^{-1} in the lower bay, and phytoplankton concentration in the range of 10~15 μg l^{-1} in the upper bay, 10~30 μg l^{-1} in the mid bay, and 35~50 μg l^{-1} in the lower bay. The model apparently suggests higher productivity in the lower bay compared to the upper and mid bay, in agreement with observations (Randall and Day, 1987). The time scale of a spring bloom suggested by the model is on the order of 10~12 days. It is evident that significant gradients in space as well as in time in the three state variables exist within the bay, suggesting that the resolution of those spatial and temporal scales in the coupled model is crucial in producing a realistic hydrodynamic-ecological system.

Significant exchange of water takes place between Fourleague Bay and the open Gulf through Oyster Bayou (Figure 41). It should be noted also that significant temporal variations with energetic tidal signals are present in concentrations of the three state variables in Oyster Bayou (Figure 42a through 42c). Consequently, energetic temporal variations with pronounced peaks at tidal frequencies are suggested in the fluxes of those variables through Oyster Bayou (Figures 43a through 43c). Significant fluxes of suspended sediments as well as nitrogen are flushed out of Fourleague Bay into the open Gulf on each ebb tide (Figures 43a and 43b). Moreover, Fourleague Bay appears to act as a source of phytoplankton for the open Gulf, as a plume of high concentrations of phytoplankton spills out into the open Gulf on each tidal cycle as shown in Figure 43c. Those observations suggest that during periods of "spring bloom," Fourleague Bay could act as a source of phytoplankton to the neighboring open Gulf.

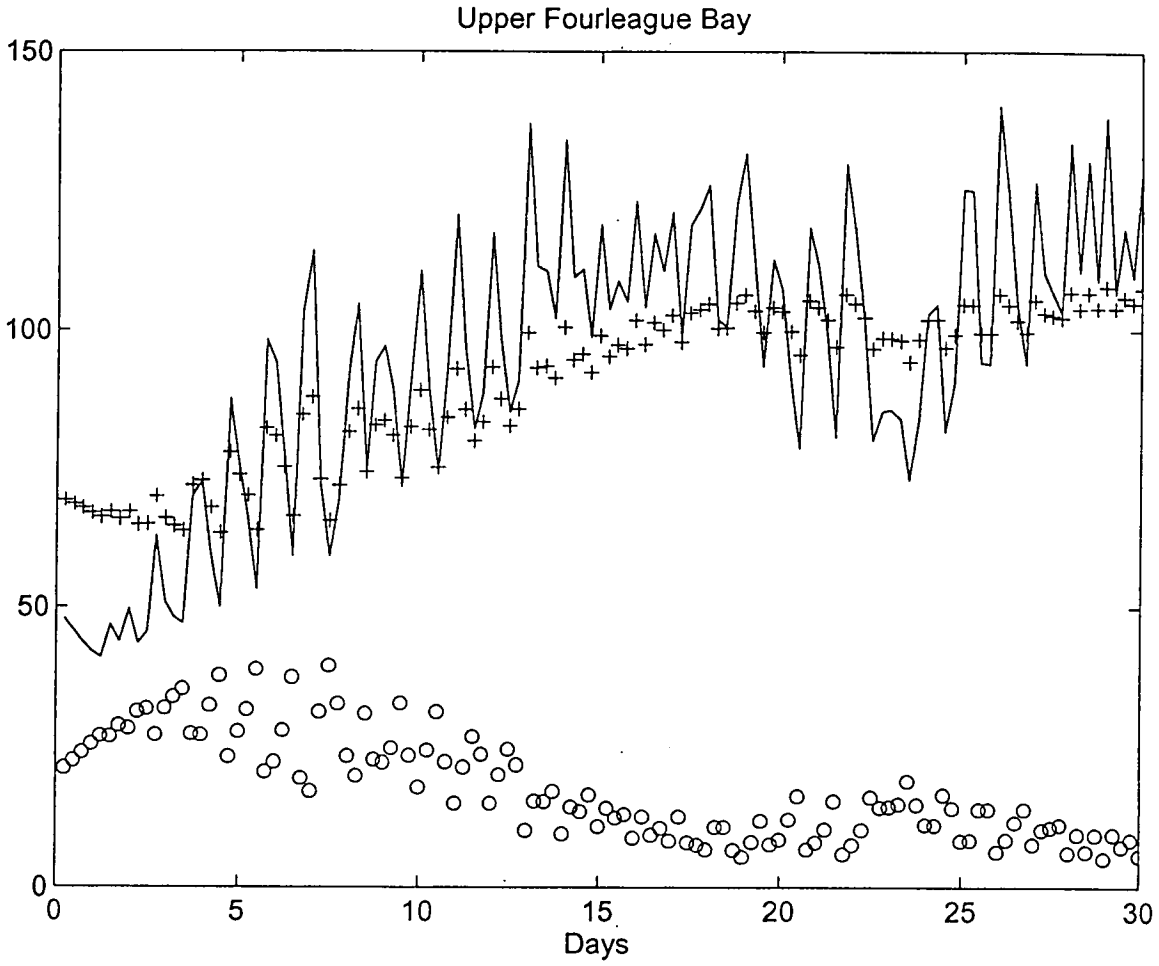

Figure 39a. Simulated concentrations of suspended sediment (mg l^{-1})(solid line), nitrogen (μg at l^{-1}) (+) and phytoplankton (μg l^{-1}) (circles) for the first 30 days. At Upper Fourleague Bay.

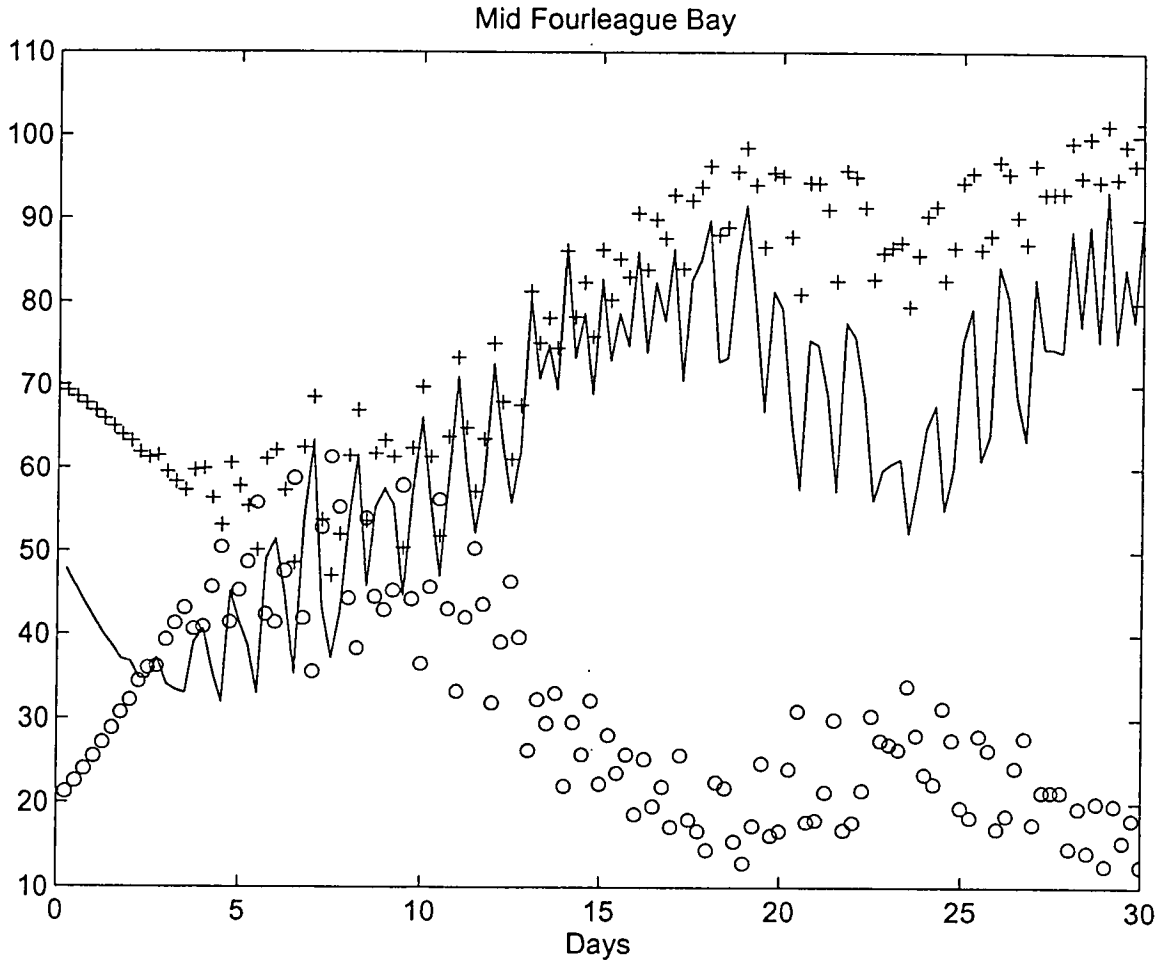

Figure 39b. Simulated concentrations of suspended sediment (mg l^{-1})(solid line), nitrogen (μg at l^{-1}) (+) and phytoplankton (μg l^{-1}) (circles) for the first 30 days. At Mid Fourleague Bay.

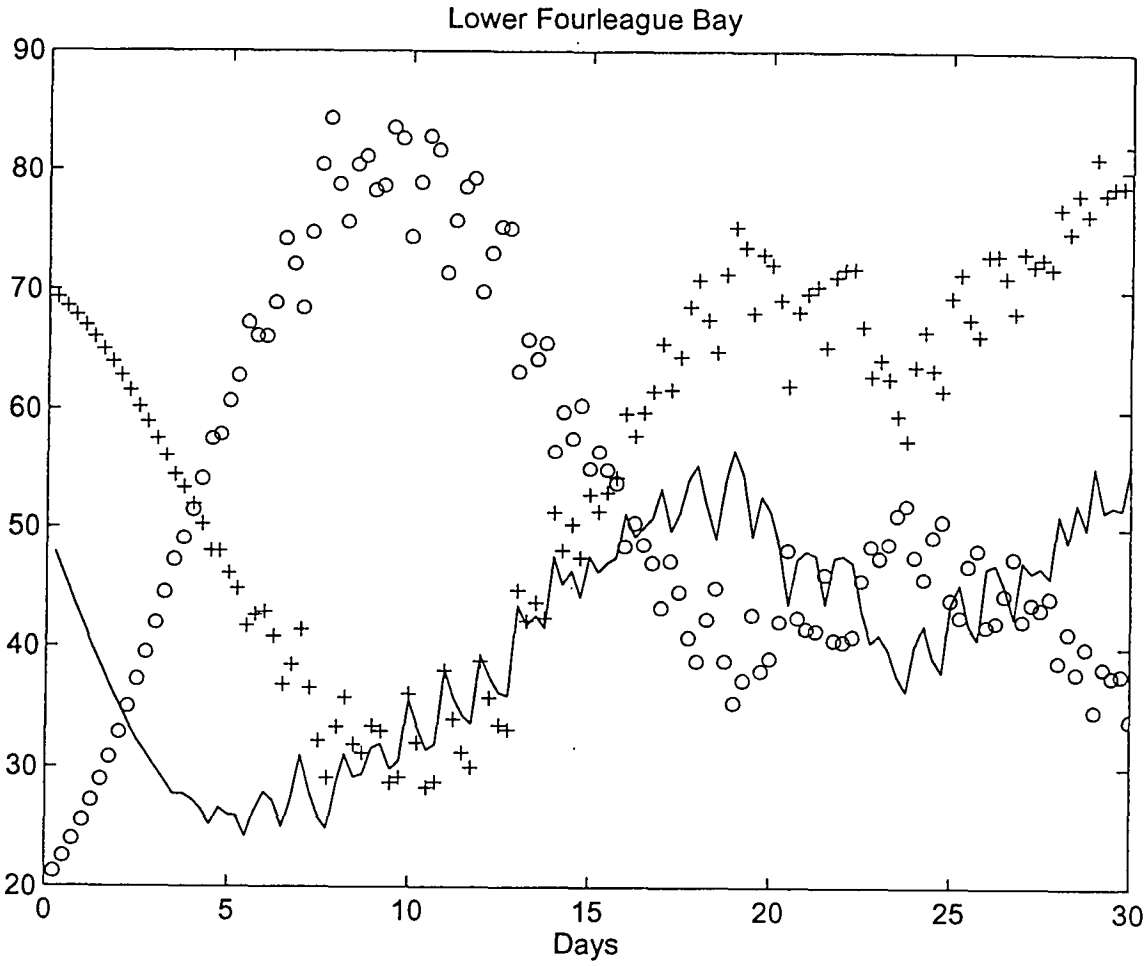

Figure 39c. Simulated concentrations of suspended sediment (mg l^{-1})(solid line), nitrogen (μg at l^{-1}) (+) and phytoplankton (μg l^{-1}) (circles) for the first 30 days. At Lower Fourleague Bay.

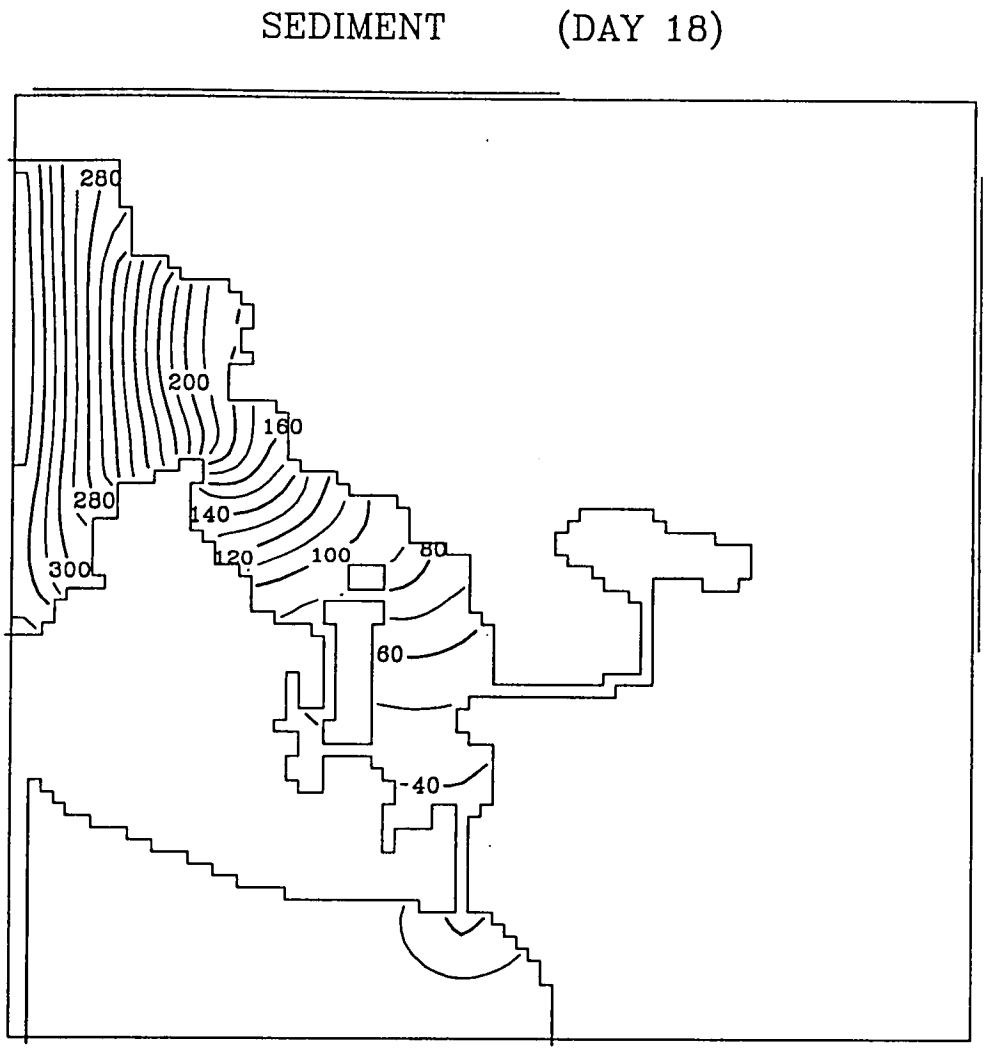

Figure 40a. Simulated concentrations of suspended sediments (mg l^{-1}) in Fourleague Bay on Day 18.

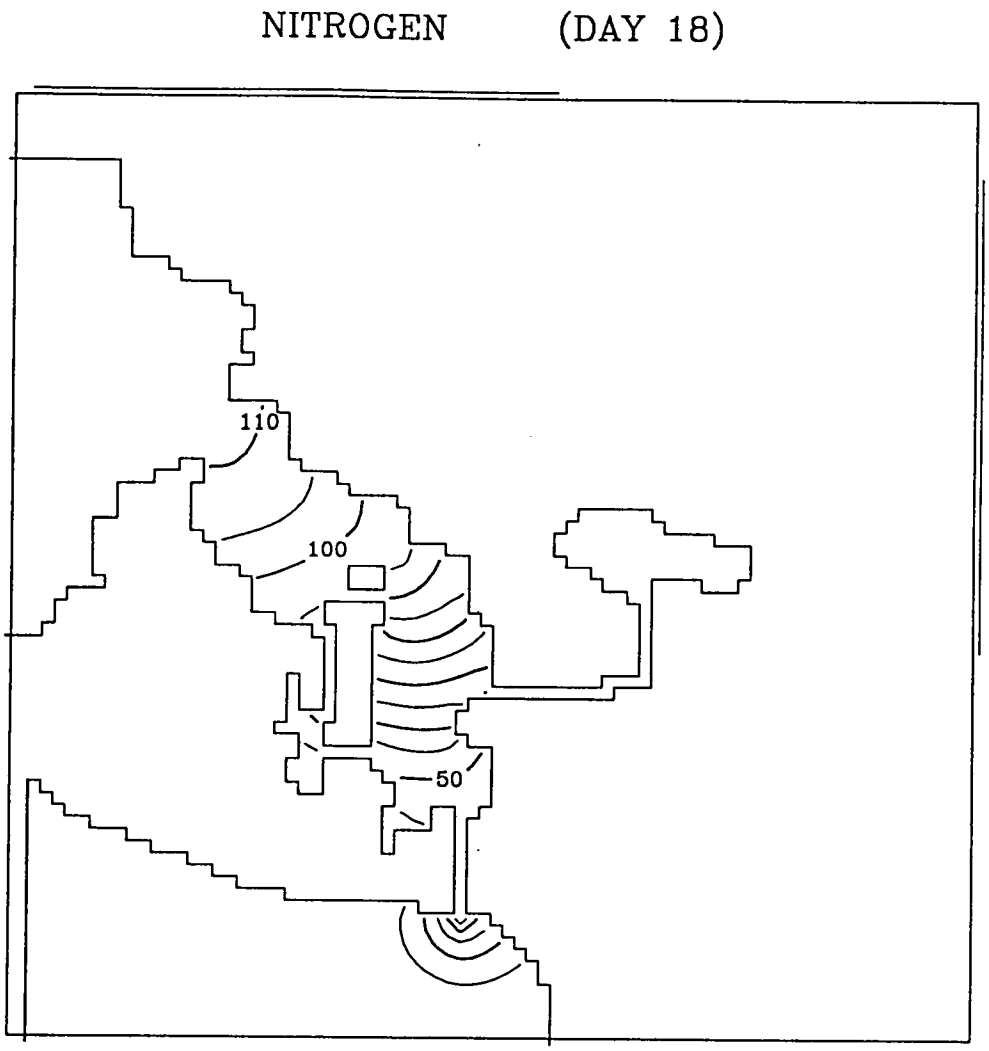

Figure 40b. Simulated concentrations of nitrogen (μg at l^{-1}) in Fourleague Bay on Day 18.

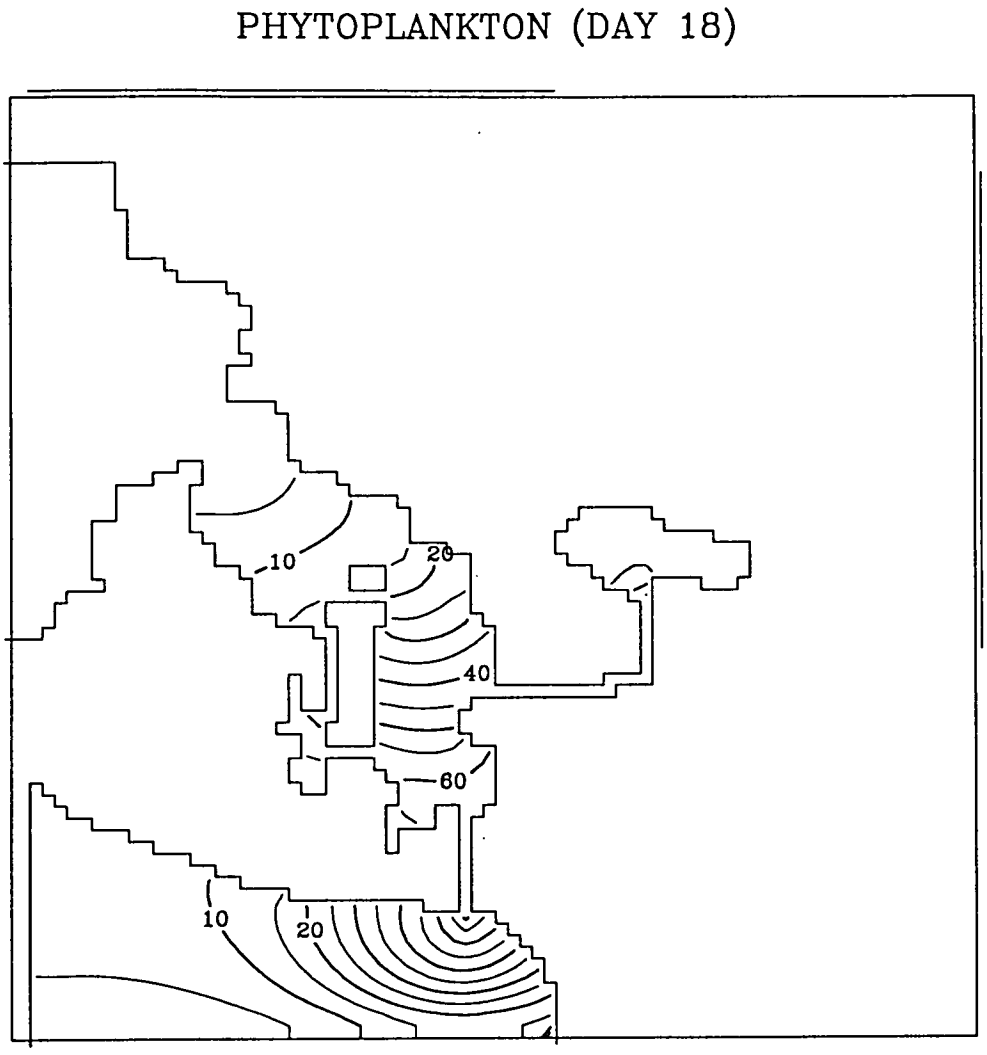

Figure 40c. Simulated concentrations of phytoplankton ($\mu g\ l^{-1}$) in Fourleague Bay on Day 18.

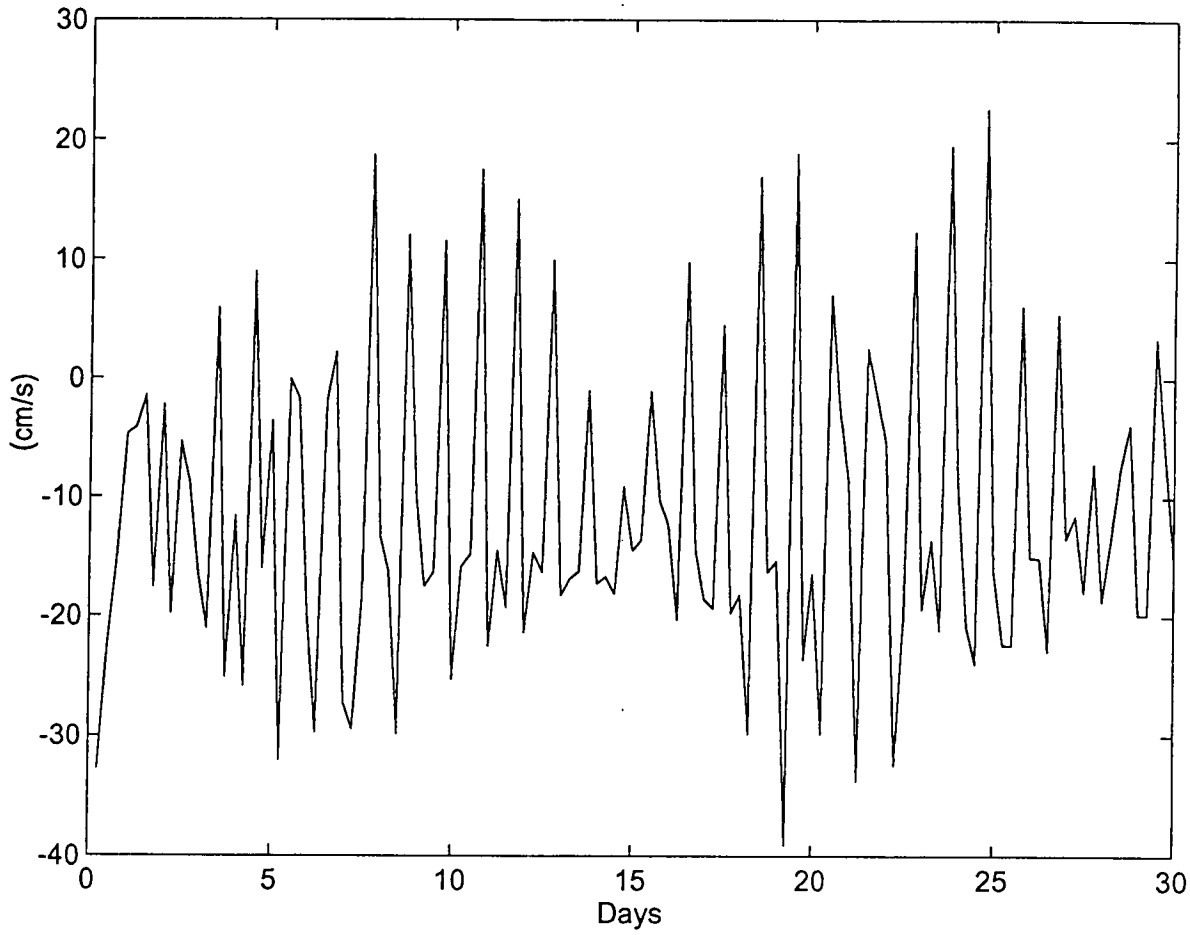

Figure 41. Simulated currents in Oyster Bayou. Positive northward, negative southward currents. Notice the mean currents are southward, indicating a net flow through Fourleague Bay due to influx of discharge from Atchafalaya River.

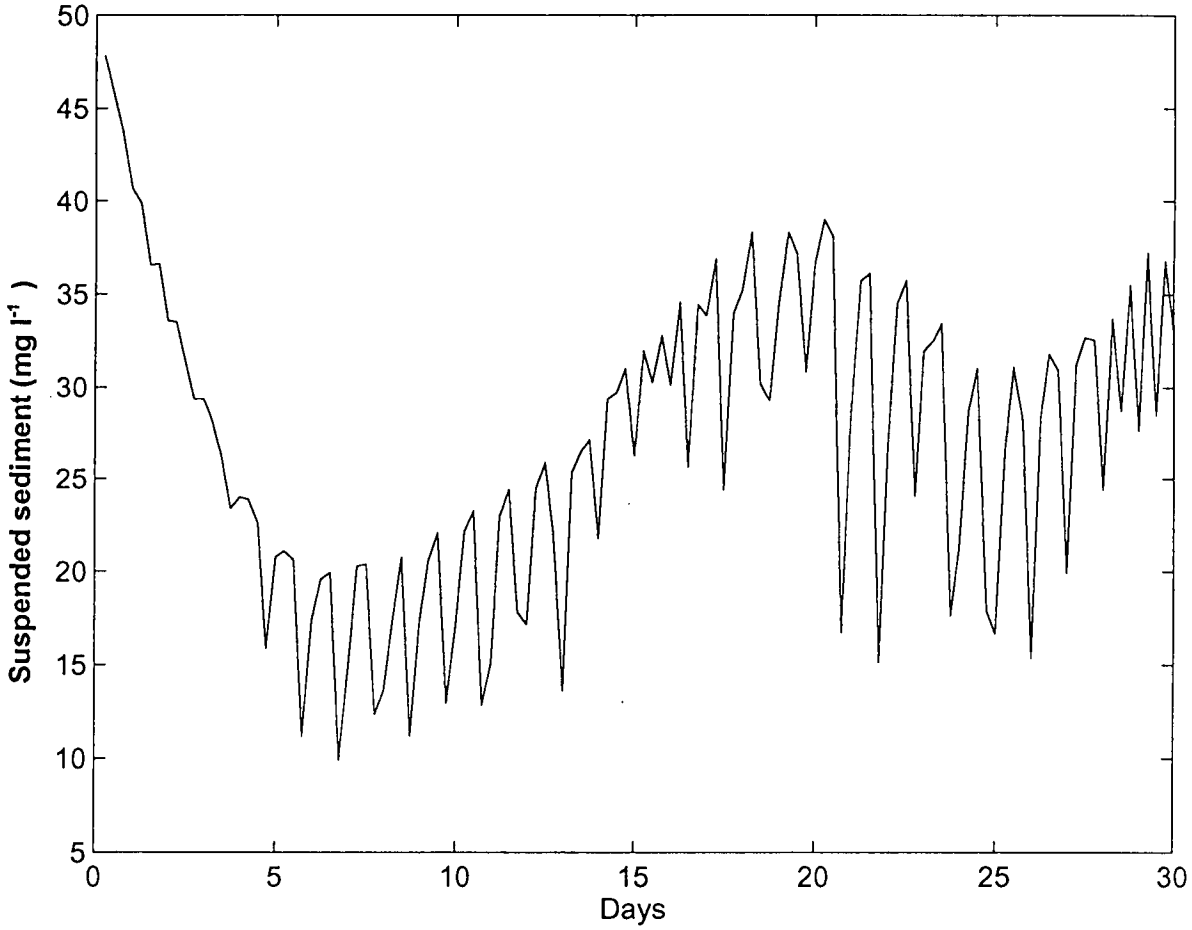

Figure 42a. Simulated suspended sediment (mg l^{-1}) in Oyster Bayou.

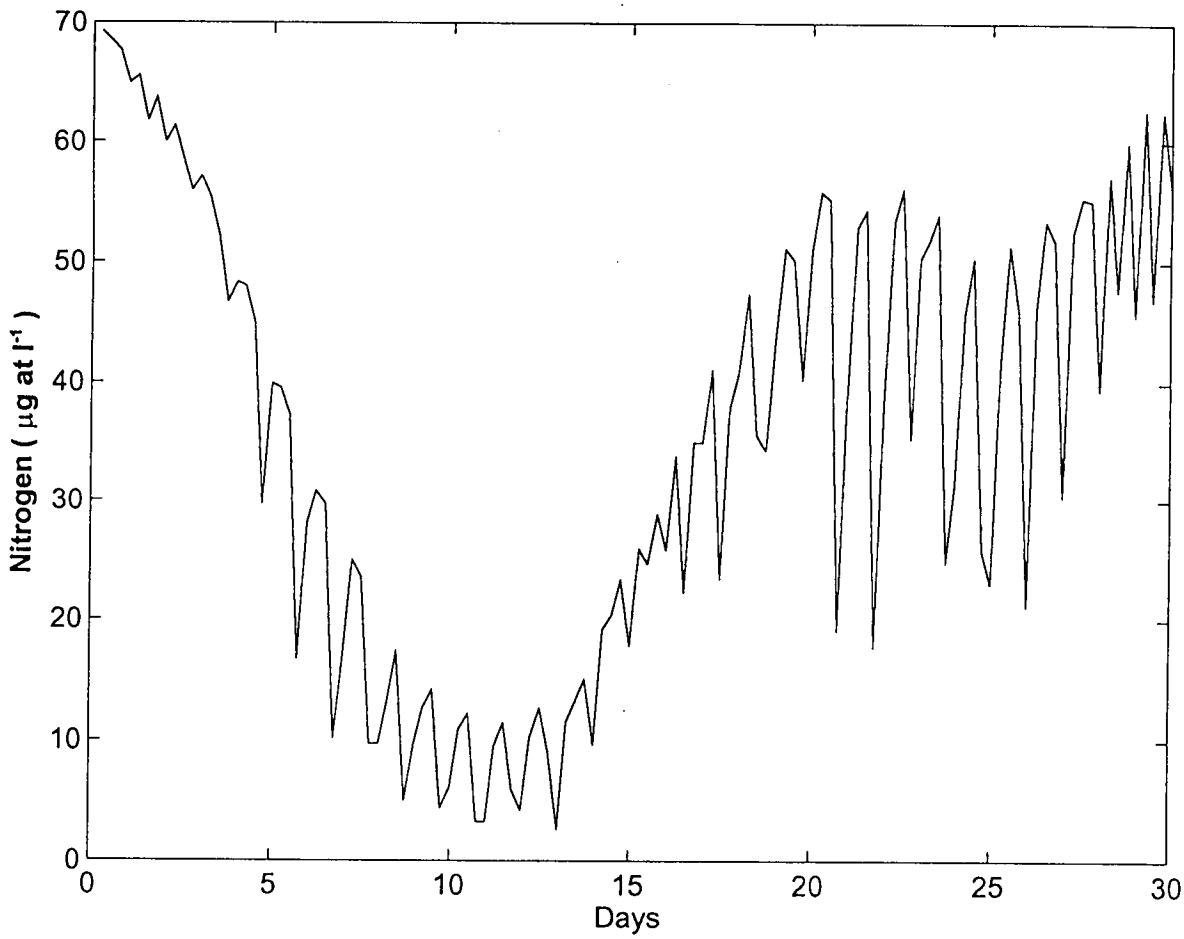

Figure 42b. Simulated nitrogen (μg at l^{-1}) in Oyster Bayou.

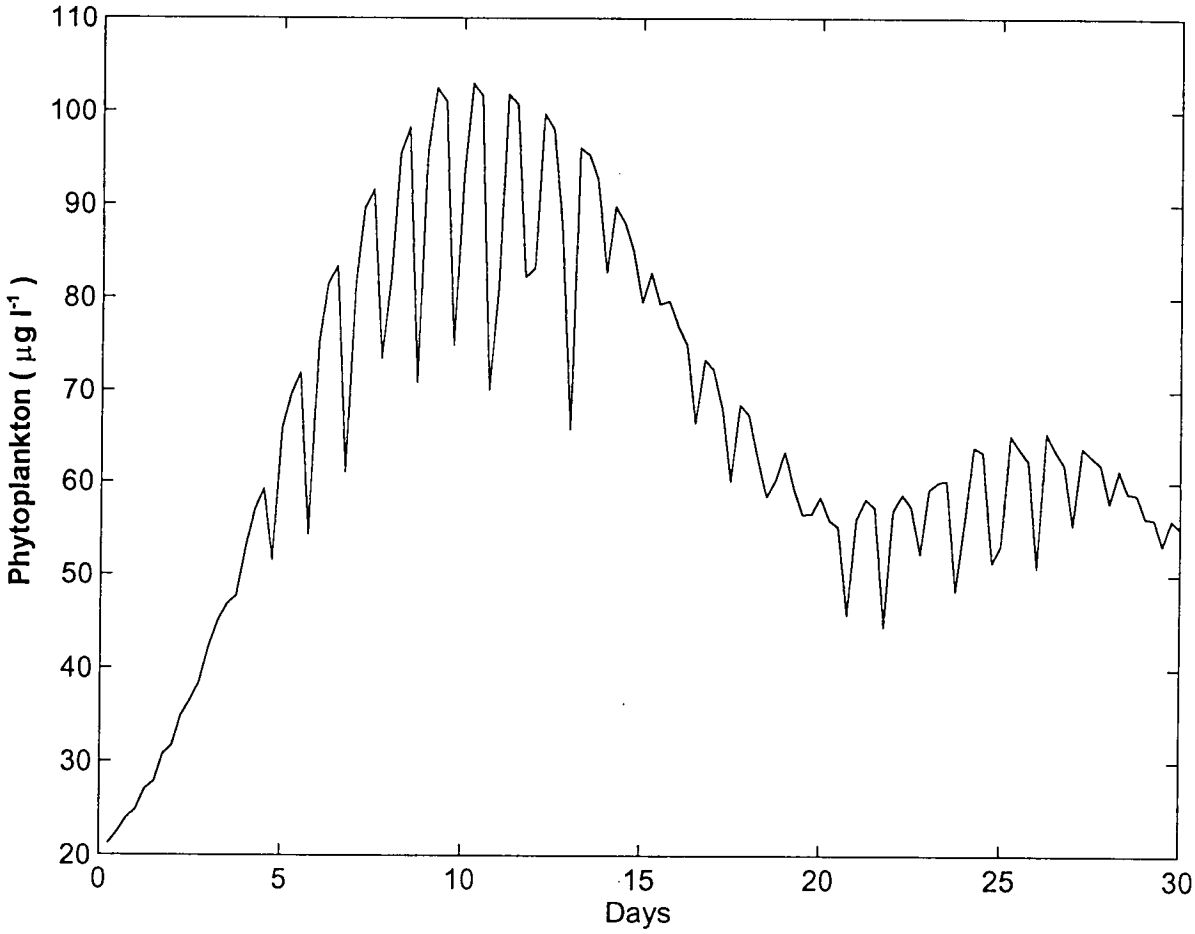

Figure 42c. Simulated phytoplankton ($\mu g\ l^{-1}$) in Oyster Bayou.

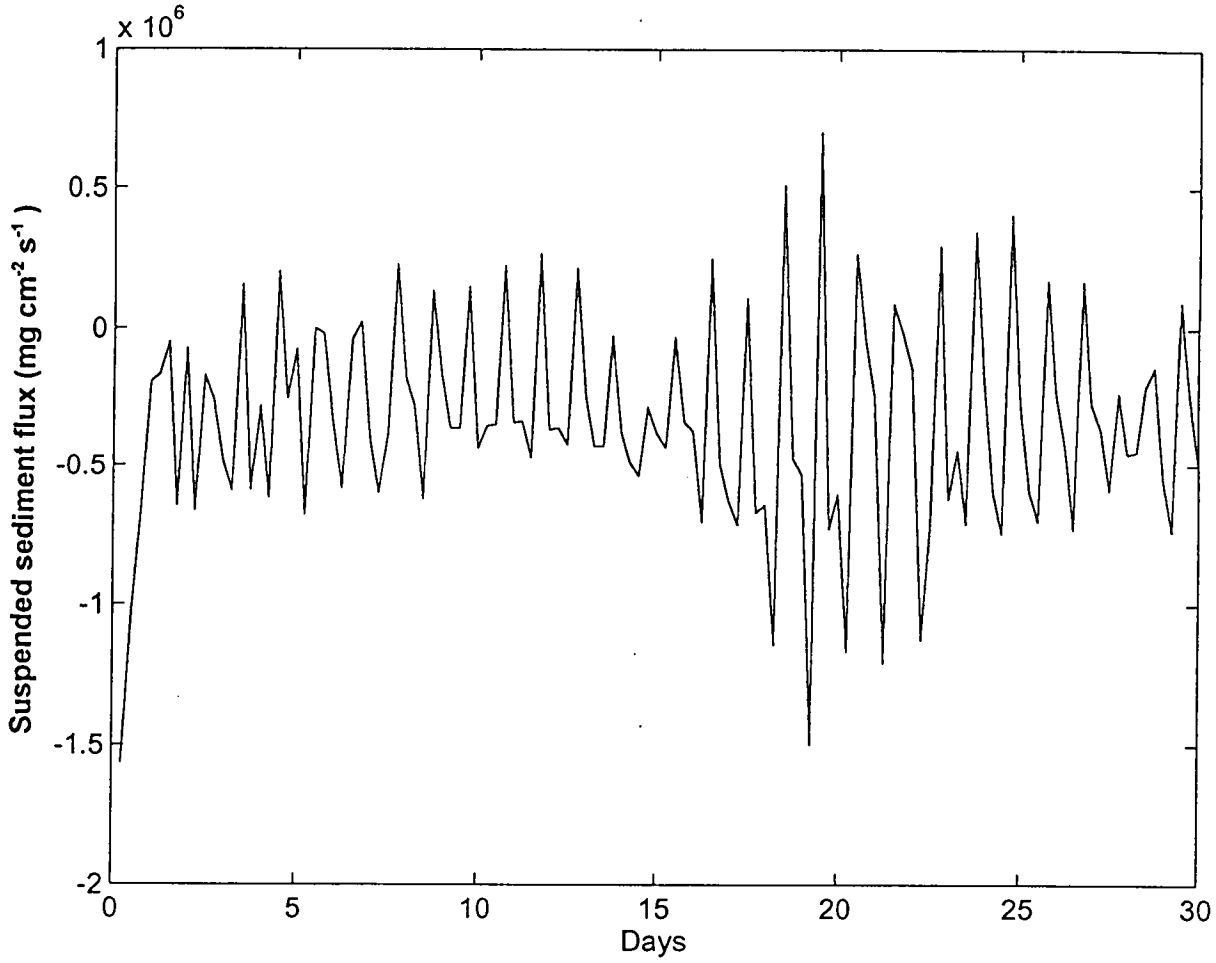

Figure 43a. Simulated suspended sediment flux (mg $cm^{-2}s^{-1}$) through Oyster Bayou. Negative values indicate southward flux toward the open Gulf.

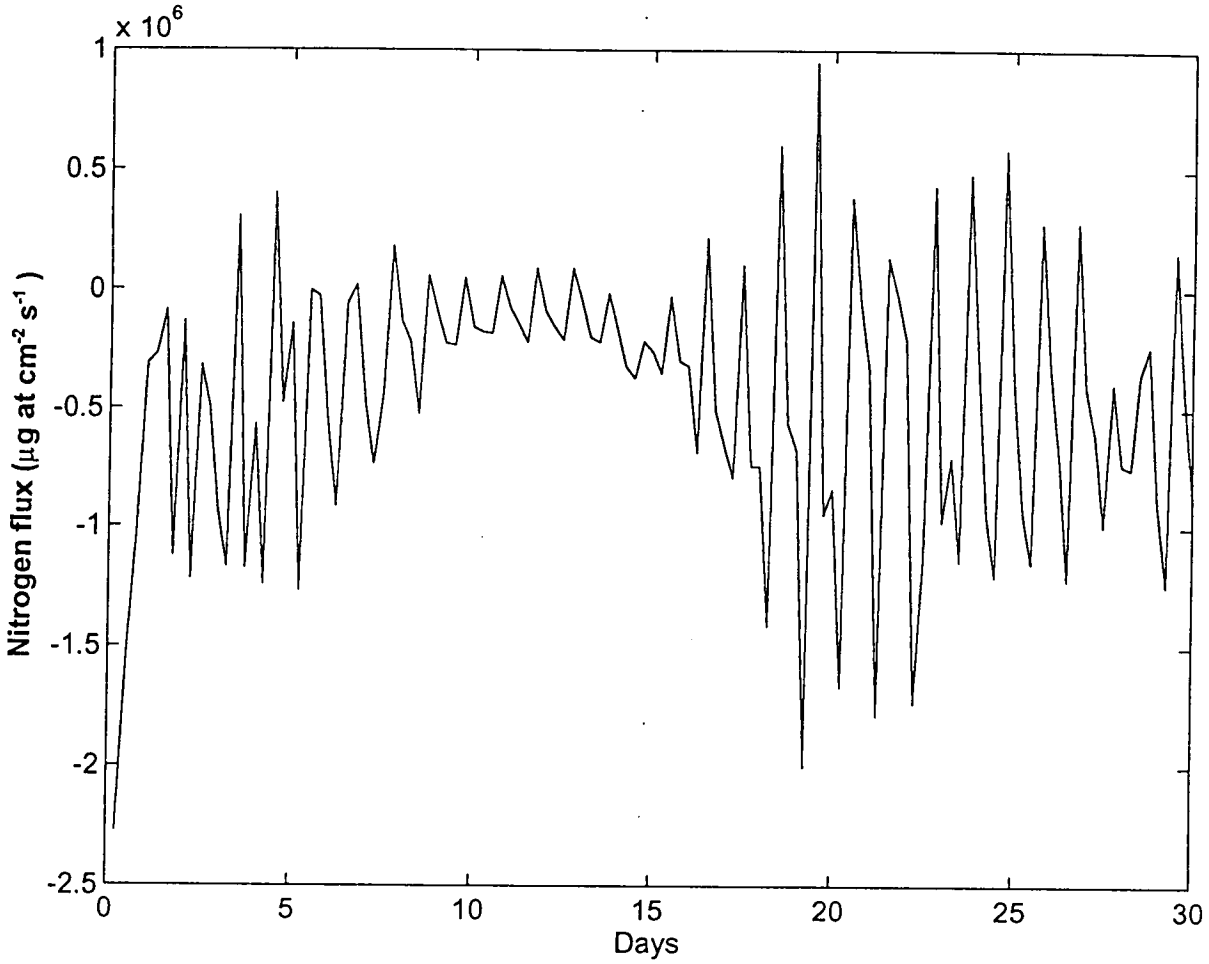

Figure 43b. Simulated nitrogen flux (µg at $cm^{-2}s^{-1}$) through Oyster Bayou. Negative values indicate southward flux toward the open Gulf.

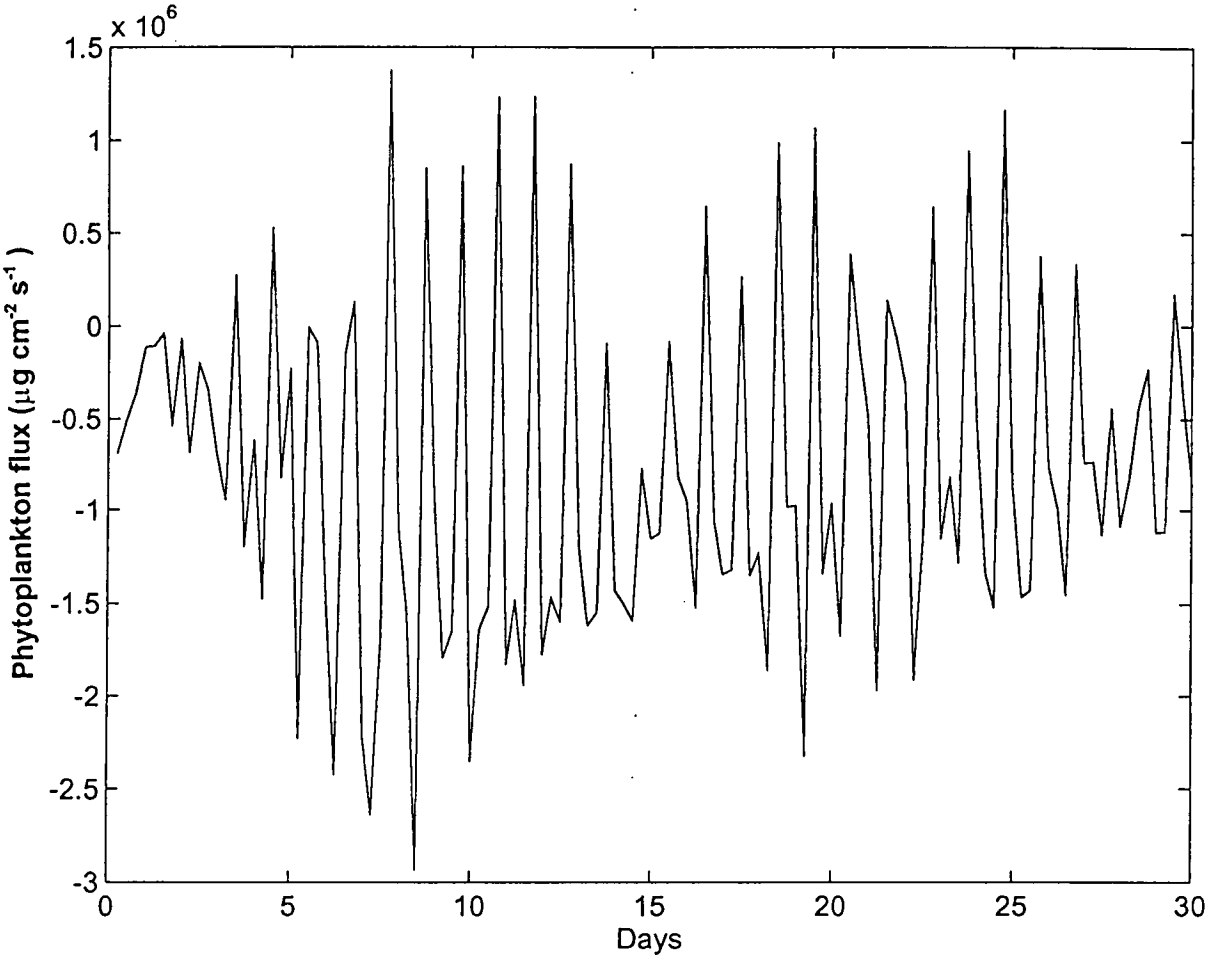

Figure 43c. Simulated phytoplankton flux ($\mu g\ cm^{-2}s^{-1}$) through Oyster Bayou. Negative values indicate southward flux toward the open Gulf.

4.5 Summary and Conclusions

A coupled hydrodynamic-ecological model was developed by coupling a two-dimensional depth-integrated hydrodynamic model to an ecological model simplified to represent three state variables, namely, suspended sediments, nutrients (total nitrogen), and phytoplankton. The model was applied to Fourleague Bay in order to simulate a spring bloom. The uniqueness of the coupled model is its ability to account for detailed hydrodynamics with spatial and temporal resolutions of less than 500 m and 10 s, respectively. The model simulation in response to a typical spring-time condition observed for Fourleague Bay, appears to be in general agreement with the previous observations. Further efforts are needed, however, to add more complexities into the model, both hydrodynamic and ecological modules, before a useful coupled model could be established for management purposes. It is very important to note that in order to simulate realistic hydrodynamic-ecological interactions in the Fourleague Bay system, it is necessary to resolve the spatial and temporal scales required to model hydrodynamics, i. e., model grid resolution as well as time step in a coupled model should be consistent with those used in hydrodynamic modeling. Of course, simulation of patchness, often observed for plankters, in a coupled model is an important issue for future research. Additional features that need to be incorporated in the coupled model include vertical resolution, bottom stress enhancement due to the combined effect of surface waves and currents, realistic resuspension of bottom sediments, additional nutrients, better representation of grazing by zooplankton, and interaction with the surrounding wetland.

CHAPTER 5

CONCLUSIONS

A two-dimensional, depth-integrated, barotropic, numerical hydrodynamic model suitable for application to the shallow, bar-built estuaries of coastal Louisiana has been developed. The model has been successfully applied to describe the circulation and dispersion in three systems - Terrebonne/Timbalier Basin, Barataria Basin, and Fourleague Bay - thus demonstrating the portability of the model. These applications involved forcing with observed winds and tides and calibration to observed currents and water levels. The model has been successfully coupled to a simple ecological model to demonstrate the ability of the model to capture time and space scale variability in circulation which is important to the accurate prediction of ecological processes.

A number of important results have derived from this effort:

- Water levels can be adequately represented within the modeling framework, even in the upper marsh regions, using topographic and bathymetric data available from historical maps and photographs.

- Water currents are well represented in the open water reaches of the lower bay systems and qualitatively represented in the upper bay regions of these systems using topographic and bathymetric data available from historical maps and photographs.

- Horizontal diffusion coefficients estimated from tracking of synthetic particles with the model indicate diffusion coefficients which are comparable with those synthesized by Okubo (1974). The largest values estimated, $O(10\ m^2\ s^{-1})$, result from coastal topographic trapping. (This process appears to be less important in the narrow channels of the upper marsh systems.) This indicates the necessity for highly accurate topography and bathymetry to achieve accurate dispersion predictions in these systems.

- When coupled with an ecological model, the hydrodynamic model is able to reproduce the observed characteristics and scales of an estuarine, spring phytoplankton bloom.

These studies, though, also raised many questions and pointed to areas of future research where model refinements are necessary before the models can be used in a quantitatively predictive sense:

- Better coupling of the estuarine environment with the coastal ocean is needed. This will require better models of the coastal ocean or better nearshore monitoring of conditions or both.

- Better topographic resolution and/or improved bathymetry, particularly in the highly interconnected marsh regions, is needed for accurate prediction of currents.

- Accurate estimates of fresh water input to the systems modeled are necessary for prediction of net flow and marsh flooding.

- Accurate prediction of phytoplankton dynamics will require realtime forcing functions and boundary conditions for the ecological models and more complex models.

REFERENCES

Aref, H. 1984. Stirring by chaotic advection. J. Fluid Mech. 143:1-21.

Awaji, T., N. Imasato and H. Kunishi. 1980. Tidal exchange through a strait: A numerical experiment using a simple model basin. J. Phys. Oceanogr. 10:1,499-1,508.

Awaji, T. 1982. Water mixing in a tidal current and the effect of turbulence on tidal exchange through a strait. J. Phys. Oceanogr. 12:501-514.

Böning, C. and M. D. Cox. 1988. Particle dispersion and mixing of conservative properties in an eddy-resolving model. J. Phys. Oceanogr. 18:320-338.

Bowden, K. F. 1965. Horizontal mixing in the sea due to a shearing current. J. Fluid. Mech. 21:83-95.

Brown, M. G. and K. B. Smith. 1990. Are SOFAR float trajectories chaotic? J. Phys. Oceanogr. 20:139-149.

Brown, M. G. and K. B. Smith. 1991. Ocean stirring and chaotic low-order dynamics. Phys. Fluids. A 3(5):1,186-1,192.

Byrne, P., M. Borengasser, G. Drew, R. A. Muller, B. L. Smith, Jr. and C. Wax. 1976. Barataria Basin: Hydrologic and climatologic processes. Sea Grant Publ. No. LSU-T-76-010. Center for Wetland Resources, Louisiana State University. Baton Rouge, LA. 176 pp.

Caffrey, J. M. 1983. The influence of physical factors on water column nutrients and suspended sediments in Fourleague Bay, Louisiana. M. S. Thesis. Louisiana State University. Baton Rouge, LA. 85 pp.

Caffrey, J. M. and J. W. Day, Jr. 1986. Control of the variability of nutrients and suspended sediments in a Gulf coast estuary by climatic forcing and spring discharge of the Atchafalaya River. Estuaries. 9(4A):296-300.

Childers, D. L. and J. W. Day, Jr. 1990. Marsh-water column interaction in two Louisiana estuaries: I. Sediment dynamics. Estuaries. 13(4):404-417.

Chuang, W. S. and Wm. J. Wiseman, Jr. 1983. Coastal sea level response to frontal passages on the Louisiana-Texas Shelf. J. Geophys. Res. 88(C4):2615-2620.

Csanady, G. T. 1973. Turbulent diffusion in the environment. D. Reidel Publishing Co. Boston, MA. 248 pp.

Davies, A. M. and J. Lawrence. 1995. Modeling the effect of wave-current interaction on the three-dimensional wind-driven circulation of the eastern Irish Sea. J. Phys. Oceanogr. 25:29-45.

Day, J. W., Jr., C. J. Madden, R. R. Twilley, R. F. Shaw, R. A. McKee, M. J. Dagg, D. L. Childers, R. C. Raynie and L. J. Rouse. 1995. The influence of Atchafalaya River discharge on Fourleague Bay, Louisiana, U. S. A. ECSA22/ERF Symposium. 151-160.

Denes, T. A. 1983. Seasonal transports and circulation of Four League Bay, Louisiana. M. S. Thesis. Louisiana State University. Baton Rouge, LA. 112 pp.

DiMego, G. J., L. F. Bosart and G. W. Endersen. 1976. An examination of the frequency and mean conditions surrounding frontal incursions into the Gulf of Mexico and Caribbean Sea. Mon. Wea. Rev. 104:709-718.

Eckart, C. 1948. An analysis of the stirring and mixing processes in incompressible fluids. J. Mar. Res. 7:265-275.

Elliott, B. A. and R. O. Reid. 1976. Salinity induced horizontal estuarine circulation. J. Waterways, Harbors and Coastal Engineering Division. WW4:425-442.

Eppley, R. W. 1972. Temperature and phytoplankton growth in the sea. Fisheries Bulletin. 70:1063-1085.

Eppley, R. W., J. Roger and J. McCarthy. 1969. Half-saturation constants for uptake of nitrate and ammonia by marine phytoplankton. Limnology and Oceanography. 14:912-920.

Fischer, H. B., E. J. List, R. C. Y. Koh, J. Imberger and N. H. Brooks. 1979. Mixing in Inland and Coastal Waters. Academic Press. New York. 483 pp.

Geyer, W. R. and R. P. Signell. 1992. A reassessment of the role of tidal dispersion in estuaries and bays. Estuaries, 15:97-108.

Grammeltvedt, A. 1969. A survey of finite-difference schemes for the primitive equations for a barotropic fluid. Mon. Wea. Rev. 97:384-404.

Gutierrez de Velasco, G. and C. D. Winant. 1996. Seasonal patterns of wind stress and wind stress curl over the Gulf of Mexico. J. Geophys. Res. 101:18,127-18,140.

Hacker, S. 1973. Transport phenomena in Estuaries. Ph.D. dissertation. Louisiana State University. Baton Rouge, La. 355 pp.

Haidvogel, D. B. 1982. On the feasibility of particle tracking in Eulerian ocean models, Ocean Modelling. 45:4-9.

Hart, W. E. 1978. A numerical study of currents, water surface elevations, and energy dissipation in Chandeleur-Breton Sound, Louisiana. Tech. Rep. No. 250. Coastal Studies Institute, Louisiana State University. Baton Rouga, LA. 97 pp.

Hart, W. E. and S. P. Murray. 1978. Energy balance and wind effects in a shallow sound. J. Geophys. Res. 83:4097-4106.

Hebblewaithe, M. 1990. The determination of marsh and offshore sediment end-member components in Terrebonne Bay, Louisiana. Master's thesis. Univ. New Orleans, New Orleans, LA. 61 pp.

Hsu, S. A. and B. W. Blanchard. 1991. Shear velocity and eolian sand transport on a barrier island. Proceedings Coastal Sediments '91, Specialty Conference/WR Div./ASCE. Seattle, WA. 220-234.

Hsu, S. A. and B. W. Blanchard. 1993. Meteorological forcing on Louisiana wetlands. Proceedings, 8th Symposium on Coastal and Ocean Management. New Orleans, LA. 230-242. published by the American Society of Civil Engineers. New York.

Ichiye, T., M. Inoue and M. Carnes. 1981. Horizontal diffusion in ocean dumping experiments. pp. 131-159. In B. H. Ketchum, D. R. Kester, and P. K. Park. Ocean Dumping of Industrial Wastes. Plenum Press, New York, NY.

Inoue, M., J. W. Day, Jr. and D. Justic. 1996. Ecological linkages among wetland, bay, and shelf systems: II. Development of linked hydrodynamic and ecological spatial models. Project R/MPE-66. Louisiana Sea Grant Program, Louisiana State University. Baton Rouge, LA. 68 pp.

Kapolnai, A., F. E. Werner and J. O. Blanton. 1996. Circulation, mixing, and exchange processes in the vicinity of tidal inlets: A numerical study. J. Geophy. Res. 101:14,253-14,268.

Kjerfve, B. 1972. Circulation and salinity distribution in a marsh lake system in coastal Louisiana. Sea Grant Publ. No. LSU-SG-72-06. Center for Wetland Resources, Louisiana State University. Baton Rouge, LA. 54 pp.

Krauss, W. and C. W. Boning. 1987. Lagrangian properties of eddy fields in the northern North Atlantic as deduced from satellite-tracked buoys. J. Mar. Res. 45:259-291.

Kremer, J. N. and S. W. Nixon. 1978. A coastal marine ecosystem: Simulation and analysis. Springer-Verlag. New York, NY. 217 pp.

Lee, J. M., Wm. J. Wiseman, Jr. and F. J. Kelly. 1990. Barotropic sub-tidal exchange between Calcasieu Lake and the Gulf of Mexico. Estuaries. 13(3):258-264.

Leendertse, J. J. 1967. Aspects of a computational model for long period water wave propagation. RM-5294-PR. Rand Corporation. Santa Monica, CA. 165 pp.

Li, X., P. Chang and R. C. Pacanowski. 1996. A wave-induced stirring mechanism in the mid-depth equatorial ocean. J. Mar. Res. 54:487-520.

Liu, Z. and H. Yang. 1994. The intergyre chaotic transport. J. Phys. Oceanogr. 24:1,768-1,782.

Madden, C. J. 1992. Control of phytoplankton production in a shallow, turbid estuary. Ph. D. dissertation. Louisiana State University. Baton Rouge, LA. 248 pp.

Madden, C. J. and J. W. Day, Jr. 1992. Induced turbulence in rotating bottles affects phytoplankton productivity measurements in turbid waters. J. Plankton Res. 14(8):1171-1191.

Marmer, H. A. 1948. The currents in Barataria Bay. Texas A&M Research Foundation. Project 9. College Station, TX. 30 pp.

Marmer, H. A. 1954. Tides and sea level in the Gulf of Mexico. pp. 101-118. In P. S. Galtsoff. Gulf of Mexico, its origins, waters, and marine life. Fishery Bulletin. 89. U. S. Fish and Wildlife Service.

McKee, B. A., Wm. J. Wiseman, Jr. and M. Inoue. 1992. Salt-water intrusion and sediment dynamics in a bar-built estuary. pp. 13-16. In K. R. Dyers & R. J. Orth. Changes in Fluxes in Estuaries. Olsen & Olsen. Fredensborg, Denmark.

Mesinger, F. and A. Arakawa. 1976. Numerical Methods Used in Atmospheric Models. GARP Pub. Ser. 17. World Meteorological Organization. Geneva, Switzerland. 64 pp.

Okubo, A. 1967. The effect of shear in an oscillatory current on horizontal diffusion from an instantaneous source. Int. J. Oceanol. Limnol. 1:194-204.

Okubo, A. 1971. Oceanic diffusion diagrams. Deep Sea Res. 18:789-802.

Okubo, A. 1973. Effect of shoreline irregularities on streamwise dispersion in estuaries and other embayments. Neth. J. Sea Res. 6:213-224.

Okubo, A. 1974. Some speculations on oceanic diffusion diagrams. Rapp. P.-v. Reun. Cons. Int. Explor. Mer. 167:77-85.

Okubo, A., C. C. Ebbesmeyer, J. M. Helseth and A. S. Robbins. 1976. Reanalysis of the Great Lakes drogue studies data. Spec. Rep.. No. 2, Ref. 76-2. State University of New York Marine Research Center, Stony Brook, NY. 85 pp.

Ottino, J. M. 1989. The kinematics of mixing: stretching, chaos, and transport. Cambridge University Press. New York, NY. 364 pp.

Panofsky, H. A. and J. A. Dutton. 1984. Atmospheric Turbulence. Wiley. New York, NY. 397 pp.

Penland, P. S. 1990. Barrier island evolution, delta plain development, and Chenier Plain formation in Louisiana. Ph. D. dissertation. Louisiana State University. Baton Rouge, LA. 210 pp.

Prager, E. J. 1992. Modeling of circulation and transport in Terrebonne Bay, Louisiana, and its implications for oyster harvesting management. Ph. D. dissertation. Louisiana State University. Baton Rouge, LA. 145 pp.

Prandle, D. 1984. A modelling study of the mixing of Cs^{137} in the seas of the European continental shelf. Phil. Trans. R. Soc. (A)310:407-436.

Randall, J. M. and J. W. Day, Jr. 1987. Effects of river discharge and vertical circulation on aquatic primary production in a turbid Louisiana (USA) estuary. Neth. J. Sea. Res. 21:231-242.

Redalje, D. G., S. E. Lohrenz and G. L. Fahnenstiel. 1994. The relationship between primary production and the vertical export of particulate matter in a river impacted coastal system. Estuaries. 17(4):829-838.

Richardson, L. F. 1926. Atmospheric diffusion shown on a distance-neighbour graph. Proc. Roy. Soc. A(110):709-727.

Ridderinkhof, H. 1990. Residual currents and mixing in the Wadden Sea. Ph. D. dissertation. Utrecht Univ. Utrecht, Netherlands. 91 pp.

Ridderinkhof, H. and J. T. F. Zimmerman. 1992. Chaotic stirring in a tidal system. Science. 258:1,107-1,111.

Ridderinkhof, H. and J. W. Loder. 1994. Lagrangian characterization of circulation over submarine banks with application to the outer Gulf of Maine. J. Phys. Oceanogr. 24:1,184-1,200.

Roberts, H. H. (ed.) 1994. Critical physical processes of wetland loss, 1988-1994. Final Report submitted to the U. S. Geological Survey. Reston, Va. Coastal Studies Institute, Louisiana State University. Baton Rouge, LA. 364 pp.

Sanderson, B. G., A. Okubo, I. T. Webster, S. Kioroglou and R. Appeldoorn. 1995. Observations and idealized models of dispersion on the southwestern Puerto Rican insular shelf. Mathl. Comput. Modelling. 21(6):39-63.

Schroeder, W. W. and Wm. J. Wiseman, Jr. 1986. Low-frequency shelf-estuarine exchange processes in Mobile Bay and other estuarine systems on the northern Gulf of Mexico. pp. 355-367 In D. A. Wolfe. Estuarine Variability. Academic Press. Orlando, FL. 509 pp.

Signell, R. P., R. C. Beardsley, H. C. Graber and A. Capotondi. 1990. Effect of wave-current interaction on wind-driven circulation in narrow, shallow embayments. J. Geoph. Res. 95:9,671-9,678.

Signell, R. P. and W. R. Geyer. 1990. Numerical simulation of tidal dispersion around a coastal headland. pp. 210-222. In R. T. Cheng. Residual Currents and Long-Term Transport. Lecture Notes on Coastal and Estuarine Studies, 38, Springer-Verlag. New York, NY. 544 pp.

Signell, R. P. and B. Butman. 1992. Modeling tidal exchange and dispersion in Boston Harbor. J. Geophys. Res. 97:15,591-15,606.

Sobey, I. J. 1985. Dispersion caused by separation during oscillatory flow through a furrowed channel. Chem. Eng. Sci. 40:2,129-2,134.

Teague, K. G. 1983. Benthic oxygen uptake and net sediment-water nutrient fluxes in a river-dominated estuary. M. S. thesis. Louisiana State University. Baton Rouge, LA. 72 pp.

Thackston, E. L. and K. B. Schnelle, Jr. 1970. Predicting effects of dead zones on stream mixing. J. Sanitary Eng. Div. Proc. Amer. Soc. Civil Engineers. 96(SA2)319-331.

Van Sickle, V. R., B. B. Barrett and T. B. Ford. 1976. Barataria Basin: Salinity change and oyster distribution. Sea Grant Publ. No. LSU-T-76-002, Louisiana State University Center for Wetland Resources. Baton Rouge, LA. 22 pp.

von Arx, W. S. 1957. An experimental approach to problems in physical oceanography. pp. 1-29. In L. H. Ahrens, F. Press, K. Rankuma and S. K. Runcorn. Physics and Chemistry of the Earth. Pergamon, New York, NY. 259 pp.

Wang, J. D. and J. J. Connor. 1975. Mathematical modeling of near coastal circulation. Report No. 200. R, M. Parsons Laboratory for Water Resources and Hydrodynamics, MIT. Cambridge, MA. 272 pp.

Wiseman, Wm. J., Jr., S. P. Murray, J. M. Bane and M. W. Tubman. 1975. Offshore physical oceanography. Vol. II: Technical appendices, app. 3, in Environment Assessment of Louisiana Offshore Oil Port and Appertinent Storage and Pipeline Facilities. Louisiana Offshore Oil Port, Inc. New Orleans, La. 162 pp.

Wiseman, Wm. J., Jr. and E. M. Swenson. 1989. Modelling the effects of produced water discharge on estuarine salinity, In Environmental impact of produced water discharges in coastal Louisiana. In D. F. Boesch and N. N. Rabalais. Report to the Louisiana Division of the Mid-Continent Oil and Gas Association. Louisiana Universities Marine Consortium. Chauvin, LA., pp. 287.

Wiseman, Wm. J., Jr. and M. Inoue. 1993. Salinity variations in two Louisiana Estuaries. pp. 1,230-1,242. Vol. 1. In O. T. Magoon, W. S. Wilson, H. Converse and L. T. Tobin. Proceedings Coastal Zone '93, 8th Symposium on Coastal and Ocean Management. American Society of Civil Engineers. Salem, MA.

Wiseman, W. J., Jr. and M. Inoue. 1994. Salinity variability and transport processes. pp. 3.1-3.31. In H. H. Roberts. Critical Physical Processes of Wetland Loss. Final Report submitted to U. S. Geological Survey. Coastal Studies Institute, Louisiana Sate University. Baton Rouge, LA.

Young, W. R., P. B. Rhines and C. J. R. Garret. 1982. Shear flow dispersion, internal waves and horizontal mixing in the ocean. J. Phys. Oceanogr. 12:515-527.

Zimmerman, J. T. F. 1986. The tidal whirlpool: A review of horizontal dispersion by tidal and residual currents. Neth. J. Sea Res. 20:133-154.

The Department of the Interior Mission

As the Nation's principal conservation agency, the Department of the Interior has responsibility for most of our nationally owned public lands and natural resources. This includes fostering sound use of our land and water resources; protecting our fish, wildlife, and biological diversity; preserving the environmental and cultural values of our national parks and historical places; and providing for the enjoyment of life through outdoor recreation. The Department assesses our energy and mineral resources and works to ensure that their development is in the best interests of all our people by encouraging stewardship and citizen participation in their care. The Department also has a major responsibility for American Indian reservation communities and for people who live in island territories under U.S. administration.

The Minerals Management Service Mission

As a bureau of the Department of the Interior, the Minerals Management Service's (MMS) primary responsibilities are to manage the mineral resources located on the Nation's Outer Continental Shelf (OCS), collect revenue from the Federal OCS and onshore Federal and Indian lands, and distribute those revenues.

Moreover, in working to meet its responsibilities, the **Offshore Minerals Management Program** administers the OCS competitive leasing program and oversees the safe and environmentally sound exploration and production of our Nation's offshore natural gas, oil and other mineral resources. The MMS **Royalty Management Program** meets its responsibilities by ensuring the efficient, timely and accurate collection and disbursement of revenue from mineral leasing and production due to Indian tribes and allottees, States and the U.S. Treasury.

The MMS strives to fulfill its responsibilities through the general guiding principles of: (1) being responsive to the public's concerns and interests by maintaining a dialogue with all potentially affected parties and (2) carrying out its programs with an emphasis on working to enhance the quality of life for all Americans by lending MMS assistance and expertise to economic development and environmental protection.